

FEDERAL UNIVERSITY OF ESPÍRITO SANTO  
UNIVERSITY CENTER OF NORTHERN ESPÍRITO SANTO  
DEPARTMENT OF ENGINEERING AND TECHNOLOGY

BRENO EDUARDO TAVARES SOARES

AN ANALYSIS OF THE IMPACTS OF HETEROGENEITY  
LOSSES DUE TO UPSCALING IN WELL TESTING  
SIMULATIONS

SÃO MATEUS  
2018

BRENO EDUARDO TAVARES SOARES

**AN ANALYSIS OF THE IMPACTS OF HETEROGENEITY  
LOSSES DUE TO UPSCALING IN WELL TESTING  
SIMULATIONS**

Graduation Project presented to  
the Department of Engineering and  
Technology of the Federal University  
of Espírito Santo, as partial fulfillment  
for obtaining the degree of Bachelor  
of Sciences in Petroleum Engineering.

Advisor: Oldrich Joel Romero  
Guzmán  
Co-advisor: Wagner Queiroz Barros

SÃO MATEUS  
2018

**BRENO EDUARDO TAVARES SOARES**

**AN ANALYSIS OF THE IMPACTS OF HETEROGENEITY  
LOSSES DUE TO UPSCALING IN WELL TESTING  
SIMULATIONS**

Graduation Project presented to the Department of Engineering and Technology of the Federal University of Espírito Santo, as partial fulfillment for obtaining the degree of Bachelor of Sciences in Petroleum Engineering and approved by the evaluation committee below.

---

**Prof. Dr. Oldrich Joel Romero Guzmán**

Federal University of Espírito Santo

Advisor

---

**Prof. Dr. Ana Paula Meneguelo**

Federal University of Espírito Santo

---

**Prof. Dr. Jesuína Cássia Santiago de Araújo**

Federal University of Espírito Santo

**SÃO MATEUS**  
**2018**

## Abstract

Reservoir models are essential tools for managing oil and gas projects since they can predict the outcomes of different development strategies, thus optimizing the process of decision-making. A key source of data for those models is well testing, which provides valuable information about the well and reservoir in a dynamic state. The standard workflow of well test interpretation includes calibrating analytical and numerical simulations to observed results, then obtaining well and reservoir data by inverse modeling. Creating those numerical models usually requires the upscaling of a high-resolution geological grid into a low-resolution representative model, which is necessary for optimizing the usage of computational power. Under certain circumstances, upscaling can generate an accurate representation of those fine-scale models; however, as Christie (1996) states, the accuracy of this process is hardly guaranteed. Thus, the main objective of this project is to investigate the effects of upscaling when utilizing numerical simulations to support well test interpretation.

The methodology of this project consists of the development and utilization of a reservoir simulator. This simulator has been developed in C language, resembling a single-phase flow of compressible fluid in the surroundings of a vertical, multilayered well. The mathematical model has been discretized by a finite differences approach with a fully implicit temporal discretization. Its linearization has been done with what Ertekin et al. (2001) describes as the simple iteration of the transmissibility terms, and the sparse system of equations has been solved by utilizing the UMFPACK (Unsymmetric Multifrontal sparse LU Factorization Package) library. This simulator has been validated by comparing its results with simulation done with industry-standard software. After this validation, four fine-grid synthetic sandstone models have been created and upscaled into four coarse-grid models. Next, those eight cases have been put under a flow simulation for a drawdown test scenario. Finally, the results of their bottom-hole pressure, pressure drop, and Bourdet derivative have been analyzed.

Keywords: reservoir simulation, well testing, upscaling, single-phase flow.

*Dedicated to my father, Samuel Vieira Soares.*

# Acknowledgments

I cannot express enough thanks to Mr. Wagner Barros, who mentored and guided me since the beginning of this project with unparalleled attention and enthusiasm. His guidance helped me during all the time of research and writing of this project. Without his help, the goal of this work would not have been realized.

I want to express my sincere gratitude for my professors at the Universidade Federal do Espírito Santo and their contributions to my education. In particular, I want to thank Dr. Oldrich Romero, an enthusiastic professor who guided me in this project and keeps supporting me in several endeavors. I also want to acknowledge the guidance that Dr. Ana Paula Meneguelo provided me in several reservoir engineering aspects relevant to this project.

I thanks CAPES immensely for granting me a sandwich-graduation scholarship with the Science Without Borders Program. This life-changing opportunity allowed me to study abroad in the USA for two semesters at the Montana Technological University and to realize a summer internship at the Bureau of Economic Geology of the University of Texas at Austin. My professors at Montana Tech also have a significant share of contribution to my development as a petroleum engineer, and I thank them very much for this. I want to express my sincere appreciation to Dr. Ian Duncan, who supervised me at the Bureau of Economic Geology with much attention and support. Our conversations at the UT were an enriching source of knowledge in reservoir engineering, geosciences, and a threshold in my academic development.

I appreciate the support of my friends, and in particular, of Günter Gaede, who shared many hours of his time helping me to troubleshoot and debug the simulator developed in this project. His assistance was significantly helpful during the first stages of this project.

Finally, I want to express my love and gratitude to my mother, Ruth Soares, for always providing me with unfailing support and care during all my life. Thank you.

*”What we know is a drop, what  
we don’t know is an ocean.”*  
*Isaac Newton.*

# List of Figures

1.1	Absolute permeabilities. a) in 128x128 grid. b) in an 8x8 up-scaled grid. Source: Christie (1996). . . . .	2
2.1	Diagram illustrating the development of the single-phase flow equation. . . . .	5
2.2	The variation of a given macroscopic property in different levels of scale. Source: Kandlikar et al. (2014). . . . .	7
2.3	Example of a control volume in a Cartesian coordinate system. Source: Ertekin et al. (2001). . . . .	8
3.1	Illustration of three finite differences methods: central difference, forward difference, and backward difference. Source: Heinzl (1988). . . . .	17
3.2	Unidimensional example of a block-centered grid. Source: Ertekin et al. (2001). . . . .	19
3.3	Example of a tridimensional grid representing an artificial, parallelepipedal reservoir. . . . .	20
3.4	Illustration of the matrix coefficients utilized for representing the transmissibilities. Source: Ertekin et al. (2001). . . . .	27
3.5	The convergence of the Newton-Raphson method in comparison with the Simple Iteration of the Transmissibility Terms. Source: Ertekin et al. (2001). . . . .	30
3.6	Example of a relationship between pressure and viscosity in a fluid model. . . . .	32
3.7	Example of a relationship between pressure and specific weight in a fluid model. . . . .	33
3.8	Example of a relationship between pressure and FVF in a fluid model. . . . .	33
4.1	Example of a flow-rate specified well. . . . .	36

4.2	Vertical section of the wellbore and the grid blocks considered in its flow model. Source: Ertekin et al. (2001) . . . . .	39
4.3	Wellbore with multiple layers. Source: Ertekin et al. (2001) . .	40
4.4	Example of well completions passing across multiple grid blocks. The color represents the source/sink term of each grid block in a given time step for a production scenario. This image represents an unrealistic scenario since each layer has the same value of individual flow rate. . . . .	41
4.5	Example of well completions passing across multiple grid blocks. The color represents the source/sink term of each grid block in a given time step for a production scenario. This image depicts a realistic scenario in which each layer has a different value of individual flow rate. . . . .	42
5.1	Iteration in the equilibration process. . . . .	47
5.2	Iteration for calculating the pressure distribution after a time step. . . . .	49
5.3	Fluid proprieties for the simulation. . . . .	51
5.4	Well flow rate in the simulation. Negative values indicate production. . . . .	52
5.5	Comparison between the CSPF and IMEX for a drawdown/buildup well test in a homogeneous reservoir. . . . .	52
5.6	Comparison between the CSPF and IMEX for a drawdown/buildup well test in a heterogeneous and anisotropic reservoir. . . . .	53
5.7	Relative differences between CSPF and IMEX for the heterogeneous and homogeneous cases. . . . .	54
6.1	Illustration of porosity upscaling from a fine to a coarse grid. Source: Lie (2015). . . . .	55
6.2	Illustration of a perfectly stratified medium with layers perpendicular to the pressure gradient. According to Lie (2015), in this setting, harmonic is the appropriate averaging for upscaling permeability. Source: Lie (2015). . . . .	60
6.3	Illustration of a perfectly stratified medium with layers parallel to the pressure gradient. According to Lie (2015), in this setting, arithmetic is the appropriate averaging for upscaling permeability. Source: Lie (2015). . . . .	61
7.1	Typical representation of a bottom hole pressure behavior in a drawdown/build-up test. Source: Bourdet (2002). . . . .	63

7.2 Schematical representation of a spherical flow in a reservoir. Source: Bourdet (2002). . . . .	64
7.3 Pressure drop and its derivative in a log-log plot for a well with partial penetration. Bourdet (2002) shows that the slope of the pressure derivative curve is equal to $-\frac{1}{2}$ in this scenario. Source: Bourdet (2002). . . . .	64
8.1 Relationship between the porosity and permeability of the UNISIM-I, a synthetic sandstone model based on the Namorado Field, Campos Basin of Brazil. Source: Avansi and Schiozer (2015). The eight models constructed in this chapter have the same porosity-permeability relationship, as shown in this pic- ture. . . . .	68
8.2 Well flow rate for all the cases in the simulation. Negative values indicate production. . . . .	70
8.3 Bottom hole pressure for the fine models (case 1, case 3, case 5, and case 7). . . . .	71
8.4 Bottom hole pressure for case 1 and its upscaled version, case 2. .	72
8.5 Bottom hole pressure for case 3 and its upscaled version, case 4. .	73
8.6 Bottom hole pressure for case 5 and its upscaled version, case 6. .	74
8.7 Bottom hole pressure for case 7 and its upscaled version, case 8. .	75
8.8 Pressure drop and Bourdet derivative for the fine-grid models (case 1, case 3, case 5, and case 7). . . . .	76
8.9 Pressure drop and Bourdet derivative for case 1 and its up- scaled version, case 2. . . . .	77
8.10 Pressure drop and Bourdet derivative the case 3 and its up- scaled version, case 4. . . . .	77
8.11 Pressure drop and Bourdet derivative the case 5 and its up- scaled version, case 6. . . . .	78
8.12 Pressure drop and Bourdet derivative the case 7 and its up- scaled version, case 8. . . . .	78
A.1 Example of a $4 \times 3 \times 3$ grid modeling a parallelepipedal reser- voir. Source: Ertekin et al. (2001). . . . .	86
A.2 Representation of the system of equations originated in the simulation of the reservoir described by Figure A.1. Source: Ertekin et al. (2001). . . . .	91
A.3 Coefficient matrix of the system of equations originated from the Ertekin et al. (2001) example of a $4 \times 3 \times 3$ reservoir with sealed boundaries. The black squares represent the non-zero entries. Source: Ertekin et al. (2001). . . . .	92

*List of Figures*

---

C.1	Porosity distribution for case 3 and its upscaled version (case 4). . . . .	102
C.2	Horizontal permeability distribution for case 3 and its upscaled version (case 4). . . . .	103
C.3	Vertical permeability distribution for case 3 and its upscaled version (case 4). . . . .	103
C.4	Porosity distribution for case 5 and its upscaled version (case 6). . . . .	104
C.5	Horizontal permeability distribution for case 5 and its upscaled version (case 6). . . . .	104
C.6	Vertical permeability distribution for case 5 and its upscaled version (case 6). . . . .	105
C.7	Porosity distribution for case 7 and its upscaled version (case 8). . . . .	105
C.8	Horizontal permeability distribution for case 7 and its upscaled version (case 8). . . . .	106
C.9	Vertical permeability distribution for case 7 and its upscaled version (case 8). . . . .	106

## List of Tables

4.1	Algorithm for modeling a well with multiple perforated grid blocks.	44
5.1	Parameters of the homogeneous scenario for the validation.	50
8.1	Common characteristics for all the simulation cases.	67
8.2	Difference between each simulation scenario.	69
B.1	Count of the non-zero coefficients of the Eq. 3.5.9 for the grid blocks in the example described by Figure A.1 from Ertekin et al. (2001).	98
B.2	Count of the non-zero coefficients of the Eq. 3.5.9 for the grid blocks in the example described by Figure A.1 from Ertekin et al. (2001).	100

# Contents

<b>1</b>	<b>Introduction</b>	<b>1</b>
1.1	Objectives . . . . .	3
<b>2</b>	<b>Mathematical Formulation</b>	<b>5</b>
2.1	Continuity Equation . . . . .	7
2.2	Darcy's Law . . . . .	11
2.3	Equation of State . . . . .	12
2.4	Compressibility . . . . .	13
2.5	Porosity . . . . .	15
2.6	Single-Phase Flow Equation . . . . .	16
<b>3</b>	<b>Numerical Formulation</b>	<b>17</b>
3.1	Grid Definition . . . . .	19
3.2	Discretization in Space . . . . .	21
3.3	Discretization in Time . . . . .	25
3.4	Matrix Notation . . . . .	27
3.5	Linearization . . . . .	30
<b>4</b>	<b>Well Representation</b>	<b>35</b>
4.1	Inflow Performance Relationship . . . . .	37
4.2	Peaceman Model . . . . .	39
4.3	Well Model for Multiple Perforated Layers . . . . .	40
<b>5</b>	<b>Solution</b>	<b>45</b>
5.1	Equilibration Process . . . . .	46
5.2	Advancing in Time . . . . .	48
5.3	Validation . . . . .	50
<b>6</b>	<b>Fundamentals of Upscaling</b>	<b>55</b>
6.1	Upscaling Additive Proprieties . . . . .	57
6.2	Upscaling Absolute Permeability . . . . .	58

6.2.1	Flow-based Methods . . . . .	58
6.2.2	Averaging Methods . . . . .	59
<b>7</b>	<b>Fundamentals of Well Testing</b>	<b>62</b>
<b>8</b>	<b>Analysis of the Impacts of Heterogeneity Losses due to Up-scaling in Well Testing Simulations</b>	<b>66</b>
8.1	Models . . . . .	67
8.2	Results . . . . .	70
<b>9</b>	<b>Final Remarks</b>	<b>80</b>
9.1	Future Suggestions . . . . .	82
	<b>Appendices</b>	<b>85</b>
	<b>A Visualization of the Linear System of Equations</b>	<b>86</b>
	<b>B Sparse Matrices Representation with the CSC Method</b>	<b>93</b>
B.1	Representation of a Generic Matrix with the CSC Method . .	94
B.2	Representing the Coefficient Matrix of the Linear System of Equations with the CSC Method . . . . .	97
	<b>C Petrophysical Distributions of the Models</b>	<b>102</b>

# Nomenclature

## Acronyms

BTCS Backwards-time, central-space

CSPF Compressible, Single-Phase Flow simulator

FVF Formation Volume Factor

IPR Inflow Performance Relationship

NNZ Number of non-zero elements of a given matrix

PI Productivity Index

UMFPACK Unsymmetric Multifrontal sparse LU Factorization Package

## Greek Symbols

$\alpha_c$  Volumetric conversion factor

$\beta_c$  Transmissibility conversion factor

$\Delta x$  Length of the grid block in the  $x$  direction

$\Delta y$  Length of the grid block in the  $y$  direction

$\Delta z$  Length of the grid block in the  $z$  direction

$\epsilon$  Tolerance of the iteration

$\gamma$  Specific weight

$\Gamma_{i,j,k}$  Accumulation coefficient

$\gamma_{wb}$  Average specific weight inside the wellbore

$\mu$  Dynamic viscosity

$\Omega$  Region that will be upscaled

$\Phi$  Fluid potential

$\phi$  Porosity

$\rho$  Specific mass

### Roman Symbols

$A$  Left-side matrix for the linear system

$A$  Transversal area

$A_1$  Arithmetic average operator

$A_p$  Generic average operator utilizing the power average notation

$A_{-1}$  Harmonic average operator

$A_{G_{i,j,k}}$  Modified transmissibility coefficient for  $Z_{i,j,k+1/2}$  in matrix notation

$A_{i,j,k}$  Transmissibility coefficient of  $p_{i,j,k+1/2}$  in matrix notation

$B$  Formation volume factor

$B$  Right-side matrix for the linear system

$B_{G_{i,j,k}}$  Modified transmissibility coefficient for  $Z_{i,j,k-1/2}$  in matrix notation

$B_{i,j,k}$  Transmissibility coefficient of  $p_{i,j,k-1/2}$  in matrix notation

$c$  Compressibility

$c$  Generic constant

$C_{G_{i,j,k}}$  Modified transmissibility coefficient for  $Z_{i,j,k}$  in matrix notation

$C_{i,j,k}$  Transmissibility coefficient of  $p_{i,j,k}$  in matrix notation

$E_{G_{i,j,k}}$  Modified transmissibility coefficient for  $Z_{i+1/2,j,k}$  in matrix notation

$E_{i,j,k}$  Transmissibility coefficient of  $p_{i+1/2,j,k}$  in matrix notation

$G_{i,j,k}$  Geometric transmissibility

$H$  Total height in a reservoir

$h$  Reservoir height

$J_w$	Productivity index for the well
$K$	Permeability tensor
$k$	Absolute permeability
$k_H$	Radial permeability
$L$	Total length of a reservoir
$m$	Mass
$m_a$	Mass that accumulates inside a control volume
$m_i$	Incoming mass in a control volume
$m_o$	Outgoing mass in a control volume
$m_s$	Mass that enters or leaves a control volume through inside boundaries (wells)
$n$	A generic number for representing the number of grid blocks in a matrix
$n$	Number of grid blocks in a given direction
$N_{G_{i,j,k}}$	Modified transmissibility coefficient for $Z_{i,j+1/2,k}$ in matrix notation
$N_{i,j,k}$	Transmissibility coefficient of $p_{i,j+1/2,k}$ in matrix notation
$NZCount$	Count of non-zero elements for a given column of a matrix $M$
$p$	Pressure
$P_0$	Reference pressure for calculating the porosity
$p_e$	Reservoir external pressure
$p_i$	Initial pressure in a buildup or drawdown test
$p_{wf}$	Bottom-hole flowing pressure
$\phi_0$	Porosity of a given reference pressure
$q$	Flow rate
$q_m$	Mass flow rate

$Q_{i,j,k}$	Known right side of the single-phase flow equation in matrix notation, volume at standard conditions
$q_{spsc}$	Total specified flow rate for the well in the standard conditions
$r$	Radial dimension for cylindrical coordinates
$r_e$	Reservoir external radius
$r_w$	Well radius
$r_{eq}$	Equivalent radius
$S$	Saturation
$s$	Skin factor
$S_{G_{i,j,k}}$	Modified transmissibility coefficient for $Z_{i,j-1/2,k}$ in matrix notation
$S_{i,j,k}$	Transmissibility coefficient of $p_{i,j-1/2,k}$ in matrix notation
$T$	Temperature
$t$	Time
$T_{i,j,k}$	Transmissibility
$u$	Superficial velocity of the fluid
$V$	Volume
$V_o$	Porous volume
$V_{res}$	Reservoir volume
$w$	Mass flow rate
$W_{G_{i,j,k}}$	Modified transmissibility coefficient for $Z_{i-1/2,j,k}$ in matrix notation
$W_{i,j,k}$	Transmissibility coefficient of $p_{i-1/2,j,k}$ in matrix notation
$x$	Pressure matrix for the linear system
$Z$	Relative depth
a	Generic number for the harmonic average equation
M	A generic matrix

n Number of elements for being averaged

### Superscripts

\* Upscaled cell

$\nu$  Iteration index

$c$  Coarse cell

n Time index

### Subscripts

$\Omega$  Region that will be upscaled

$f$  Formation

$g$  Gas

$i$  Index related to the  $x$  direction

$ind$  Index of the grid block in the example of Appendix A

$j$  Index related to the  $y$  direction

$j$  Phase of a homogeneous material

$k$  Index related to the  $z$  direction

$k$  Layer index

$o$  Oil

$out$  Indicates that the grid block is out of the domain of the reservoir

$p$  Pore

$r$  Rock

$ref$  Reference

$sc$  Standard conditions

$t$  Total

$w$  Water

$x$   $x$  direction

$y$   $y$  direction

$z$   $z$  direction

BU Build up

Dd Drawdown

i For a given  $M$  sparse matrix, the array  $M_i$  is the list of coordinates of the non-zero entries in terms of row indexes for each column of  $M$ , utilized in the CSC storage method

p For a given  $M$  sparse matrix,  $M_p$  is an array with the list of the cumulative count of non-zero entries in each column of  $M$ , utilized in the CSC storage method

x For a given  $M$  sparse matrix, the array  $M_x$  is the list of values of the non-zero elements of the matrix  $M$ , utilized in the CSC storage method

# Chapter 1

## Introduction

The exploration and production of oil and gas are essential activities for fulfilling the needs of contemporary society. Delivering those resources is often associated with projects of high costs and risks. A standard way to mitigate those risks and maximize return on investment is to utilize reservoir models, which allows decision-makers to evaluate the economic viability of their projects and select the best strategies for their development. The process of building and updating those models is broad and multidisciplinary, requiring data from different sources including seismic surveys, cores, well logs, and well tests.

A well test, according to Bourdet (2002), is a formation evaluation technique that consists of monitoring the pressure of a well in production or injection during a relatively short time compared to the life cycle of the reservoir. This analysis can provide information about the reservoir and the well during a dynamic state, as opposed to geological and geophysical sources that usually only provides data of static periods. The data gathered in a well test can thus be processed with interpretation techniques, generating valuable input for reservoir models.

The well test interpretation is an inverse problem, in which the interpreter has to create or update a model based on what the output of this model has to be. In other words, the interpreter has to build a reservoir model that, under flow simulation, produces similar values of pressure than the experimental data collected from the well test. This process allows to determine different proprieties in the reservoir model, such as the wellbore storage factor, skin factor, permeability and flow regime.

When numerical models are utilized to assist well test interpretations, it is usually necessary to run simulations in models with lower resolution than the geological model available, an essential practice for optimizing the usage of computational power. According to Christie (1996), geostatistical

algorithms can describe petrophysical proprieties of a reservoir with such a high resolution that implies in geological models being far too detailed to be utilized as grids in reservoir simulators. As a result, before running numerical simulations, it is commonly necessary to upscale the geological model into a representative model with a lower resolution. This process is known as upscaling and can be visualized in Figure 1.1 below.

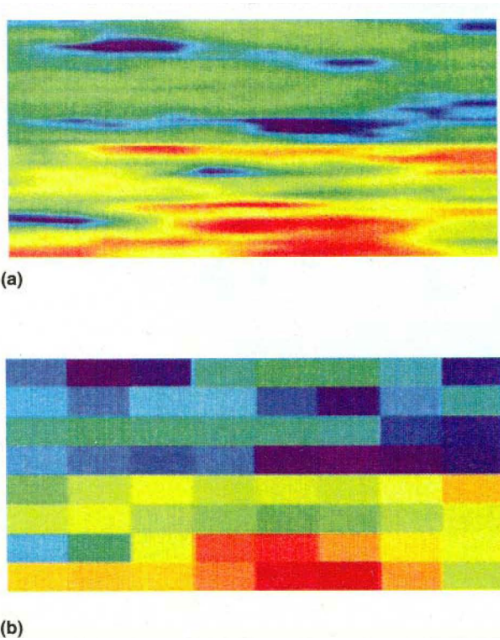


Figure 1.1: Absolute permeabilities. a) in 128x128 grid. b) in an 8x8 upscaled grid. Source: Christie (1996).

Lie (2015) states that even if one had all the computational power necessary to run simulations in high-resolution, geological models, this practice could still be ineffective for several reasons. Firstly, the industry trend indicates that a surplus in computational power would enable geologists and reservoir engineers to build even larger and more complex geological models, outperforming the improvements of flow simulation capabilities. Second, for many reservoir modeling workflows, it would be preferential to utilize the surplus in computational power to run more simulations in a low-resolution model, hence contemplating different development scenarios and spanning their range of plausible outputs; than performing a smaller number of simulations in a high-resolution, geological model. Lastly, low-resolution models contain fewer parameters than high-resolution ones, so it is easier to calibrate them with observed data in inverse modeling workflows.

## 1.1 Objectives

This project's main objective is to analyze the effects of heterogeneity losses due to upscaling in well test simulations. The idea is to build four fine-grid models and upscale those models into four coarse-grid ones. Then, well test simulations will be done in each of those eight models, and the results of bottom-hole pressure, pressure drop, and Bourdet derivative will be compared and analyzed. Such analysis will make possible a better understanding of the effects of upscaling in well test simulations, which could help to avoid quantitative and qualitative biases when utilizing numerical models to support well testing.

This study requires utilizing a reservoir simulator, which will be developed in this project as an intermediate objective. The idea is to develop this software as an open-source tool for studies and researches in reservoir simulation. It should contain the following features:

- Single-phase fluid.
- Compressible flow.
- Cartesian grid.
- Domain comprising a vertical well.
- Peaceman well model.
- Well model supporting multiple perforated layers.
- Sealed reservoir as a Neumann-type boundary condition.
- Software developed in C language.
- Linearization by what Ertekin et al. (2001) describes as the simple iteration of the transmissibility terms.
- Sparse, unsymmetrical system of equations solved by utilizing the UMF-PACK solvers, as seen in Davis (1995).

On the whole, those are the first characteristics of the reservoir simulator developed and utilized in this project, but the idea is to change or extend those features in the future for serving to other projects. After developing the simulator, it will be validated by comparing its results with simulation done by industry-standard software.

Next, four fine-grid reservoir models will be created with different levels of petrophysical dispersion. The first model will be homogeneous in terms of porosity and permeability. From this base model, the other three models will be created with the same mean values of porosity and permeability, but with different standard deviations. They will be generated by following a normal distribution for porosity and a log-normal distribution for permeability, calculated by a correlation. The permeability should have vertical anisotropy, also obtained by the utilization of a correlation.

After that, the bottom-hole pressures will be calculated by putting those eight models under flow simulation. The simulation scenario will be the drawdown stage of the test of a production well. The well will be initially closed, then opened with a constant flow rate until the end of the simulation. Then, the pressure drop and Bourdet derivative will be calculated from the bottom-hole pressure and the elapsed time. Finally, the plots of bottom-hole pressure, pressure drop, and Bourdet derivative for the eight models will be compared and analyzed.

# Chapter 2

## Mathematical Formulation

This chapter describes the mathematical formulation of the single-phase flow equation, which constitutes the basic framework for the simulator developed. The next chapters will show how this equation has been discretized and linearized for allowing its solution by numerical methods. Next, the well modeling process will be shown in a succeeding chapter, along with its attachment to the single-phase flow equation. Finally, a later chapter will show how the resulting system of equations will be linearized and solved for the boundary conditions of the problem.

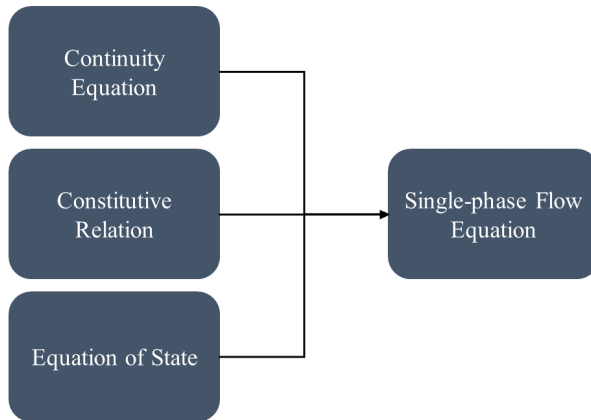


Figure 2.1: Diagram illustrating the development of the single-phase flow equation.

According to Ertekin et al. (2001), the single-phase flow in porous media can be modeled by utilizing three fundamental equations: the equation of continuity (or mass conservation) which relates the mass quantity of the

incoming and outgoing components with the accumulated mass in a given control volume; a constitutive relation, which describes the fluid momentum in the control volume; and an equation of state, relating the specific mass of the fluid in the function of its pressure, temperature, and composition. The following sections show the development of those three equations: the continuity equation, constitutive relation, and equation of state. Later, a posterior section shows how those three equations will be assembled into the single-phase flow equation.

## 2.1 Continuity Equation

The equation of continuity can be developed by utilizing the continuum assumption. This is the assumption that on a macroscopic scale, certain properties in a fluid such as density, temperature, pressure, and velocity can be defined at infinitesimal volume elements. Those elements are representative sampling volumes of the property, so it is possible to neglect the microscopic discontinuities. Thus, it is possible to assume that those variables vary continuously from one control volume to another. According to Fox et al. (2008), the continuum assumption is one of the bases of classical fluid mechanics.

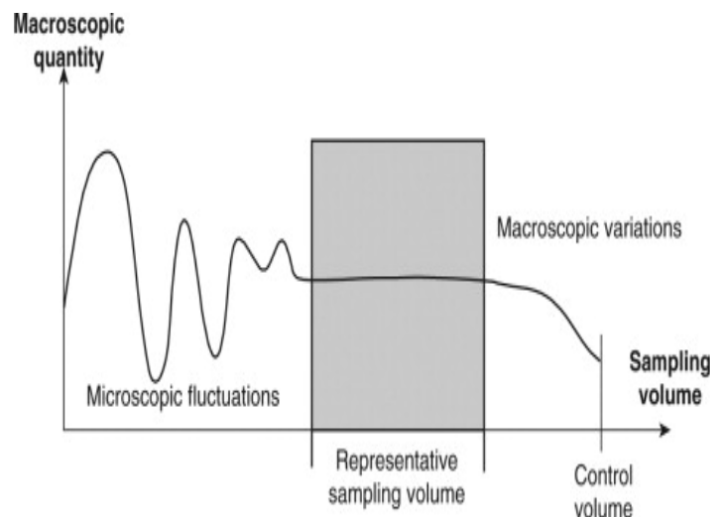


Figure 2.2: The variation of a given macroscopic property in different levels of scale. Source: Kandlikar et al. (2014).

With this assumption, the reservoir properties (e.g., porosity and permeability) can be described in terms of the average values in a control volume. Figure 2.3 represents a control volume in a Cartesian coordinate system.

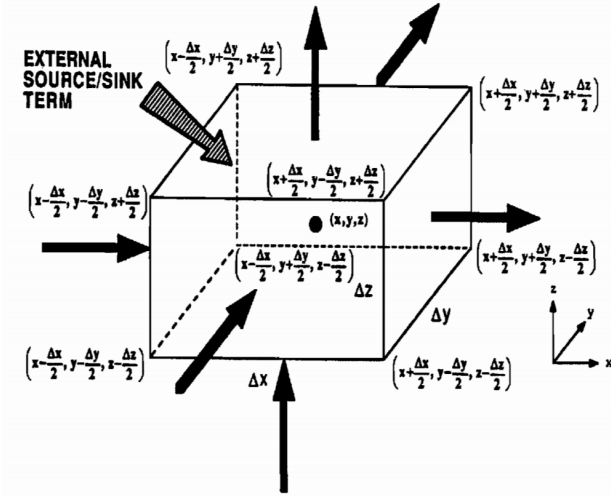


Figure 2.3: Example of a control volume in a Cartesian coordinate system.  
Source: Ertekin et al. (2001).

Mass conservation principle for classical fluid dynamics states that mass can neither be created nor destroyed within a closed system. If the inflow mass flow rate is different from the outflow mass flow rate for a closed system, then necessarily there should be variations in volume or density within that system. Mathematically:

$$(m_i - m_o) + m_s = m_a, \quad (2.1.1)$$

in which  $m_i$  and  $m_o$  are, respectively, the incoming and outgoing mass in the control volume faces,  $m_a$  is the accumulated mass inside it and  $m_s$  is the source term, which represents the mass that is added or removed in the control volume but not passes through the external boundaries (a source term typically represents the well in the case of a reservoir simulator). A quantity of mass  $m$  can also be described by:

$$m = w\Delta t, \quad (2.1.2)$$

where  $w$  is the average mass flow rate in a time interval of  $\Delta t$ . The mass flow rate can also be described in function of the average volumetric flow rate  $q$  and the specific mass of the fluid  $\rho$ :

$$w = q\rho. \quad (2.1.3)$$

The fluid volume  $V_o$  is dependent on the rock dimensions and its porous volume:

$$V_o = \Delta x \Delta y \Delta z \phi, \quad (2.1.4)$$

where  $\phi$  is the porosity and  $\Delta x$ ,  $\Delta y$  and  $\Delta z$  are the block dimensions. Therefore, Eq. 2.1.1 can be rewritten as:

$$\begin{aligned} & [(w)_{x-\Delta x/2}\Delta t + (w)_{y-\Delta y/2}\Delta t + (w)_{z-\Delta z/2}\Delta t] - \\ & [(w)_{x+\Delta x/2}\Delta t + (w)_{y+\Delta y/2}\Delta t + (w)_{z+\Delta z/2}\Delta t] + \\ & q_m\Delta t = (\Delta x\Delta y\Delta z\phi\rho)_{t+\Delta t} - (\Delta x\Delta y\Delta z\phi\rho)_t. \end{aligned} \quad (2.1.5)$$

In the Eq. 2.1.5, the two first terms, in brackets, represents the incoming and outgoing mass in the faces of the control volume. The third term describes the transference of mass through a source term; in the case of petroleum reservoirs, it models the wells in the control volume. The factor  $q_m$  is defined as the wells' mass flow rate, and it will be consistently considered positive for the injection and negative for the production. Finally, the right side of the equation defines the fluid mass accumulation in the block as the variation of its volume  $V_o$  during a time interval of  $\Delta t$ . Additionally,  $w$  can be described as:

$$\begin{aligned} w_x &= \alpha_c\rho u_x A_x, \\ w_y &= \alpha_c\rho u_y A_y, \\ w_z &= \alpha_c\rho u_z A_z, \end{aligned} \quad (2.1.6)$$

where  $u_x$ ,  $u_y$  and  $u_z$  are the superficial velocities, and  $A_x$ ,  $A_y$  and  $A_z$  are the transversal areas in the directions  $x$ ,  $y$  and  $z$ . The  $\alpha_c$  is known as the volumetric conversion factor. Substituting the Eqs. 2.1.6 in the Eq. 2.1.5:

$$\begin{aligned} & -[(\rho u_x A_x)_{x+\Delta x/2} - (\rho u_x A_x)_{x-\Delta x/2}] - [(\rho u_y A_y)_{y+\Delta y/2} - (\rho u_y A_y)_{y-\Delta y/2}] \\ & - [(\rho u_z A_z)_{z+\Delta z/2} - (\rho u_z A_z)_{z-\Delta z/2}] + \frac{q_m}{\alpha_c} \\ & = \frac{1}{\alpha_c} \frac{(\phi\rho\Delta x\Delta y\Delta z)_{t+\Delta t} - (\phi\rho\Delta x\Delta y\Delta z)_t}{\Delta t}. \end{aligned} \quad (2.1.7)$$

Applying a simultaneous limit in that the time interval and the block dimensions tend to zero:

$$\begin{aligned} & \lim_{\substack{\Delta x \rightarrow 0 \\ \Delta y \rightarrow 0 \\ \Delta z \rightarrow 0 \\ \Delta t \rightarrow 0}} \left\{ -[(\rho u_x A_x)_{x+\Delta x/2} - (\rho u_x A_x)_{x-\Delta x/2}] - [(\rho u_y A_y)_{y+\Delta y/2} - (\rho u_y A_y)_{y-\Delta y/2}] \right. \\ & \left. - [(\rho u_z A_z)_{z+\Delta z/2} - (\rho u_z A_z)_{z-\Delta z/2}] + \frac{q_m}{\alpha_c} \right\} \\ & = \lim_{\substack{\Delta x \rightarrow 0 \\ \Delta y \rightarrow 0 \\ \Delta z \rightarrow 0 \\ \Delta t \rightarrow 0}} \left[ \frac{1}{\alpha_c} \frac{(\phi\rho\Delta x\Delta y\Delta z)_{t+\Delta t} - (\phi\rho\Delta x\Delta y\Delta z)_t}{\Delta t} \right]. \end{aligned} \quad (2.1.8)$$

Developing the limit and considering  $V_b = \Delta x \Delta y \Delta z$ :

$$-\frac{\partial}{\partial x}(\rho u_x A_x) \Delta x - \frac{\partial}{\partial y}(\rho u_y A_y) \Delta y \\ - \frac{\partial}{\partial z}(\rho u_z A_z) \Delta z + \frac{q_m}{\alpha_c} = \frac{V_b}{\alpha_c} \frac{\partial}{\partial t}(\phi \rho). \quad (2.1.9)$$

Finally is obtained the Eq. 2.1.9, which is the most general form of the continuity equation for Cartesian coordinates.

## 2.2 Darcy's Law

Darcy's law is a constitutive equation that describes the laminar fluid flow in the porous media. It is an empiric relationship between apparent fluid velocity and gradient of the potential. For a given fluid flowing in Cartesian coordinates, Darcy's law is:

$$\begin{aligned} u_x &= -\beta_c \frac{k_x}{\mu} \frac{\partial \Phi}{\partial x}, \\ u_y &= -\beta_c \frac{k_y}{\mu} \frac{\partial \Phi}{\partial y}, \\ u_z &= -\beta_c \frac{k_z}{\mu} \frac{\partial \Phi}{\partial z}, \end{aligned} \quad (2.2.1)$$

where the factor  $\beta_c$  is the transmissibility conversion factor,  $k_d$  is the permeability in a given  $d$  direction, and  $\mu$  is the dynamic viscosity of the fluid. The parameter  $\Phi$  is the fluid potential, which represents the pressure added to gravitational effects. Considering  $p$  the pressure,  $Z$  a relative depth and  $\gamma$  the specific weight of the fluid, its potential can be described by:

$$\nabla \Phi = \nabla p - \gamma \nabla Z. \quad (2.2.2)$$

In this way:

$$\begin{aligned} u_x &= -\beta_c \frac{k_x}{\mu} \left( \frac{\partial p}{\partial x} - \gamma \frac{\partial Z}{\partial x} \right), \\ u_y &= -\beta_c \frac{k_y}{\mu} \left( \frac{\partial p}{\partial y} - \gamma \frac{\partial Z}{\partial y} \right), \\ u_z &= -\beta_c \frac{k_z}{\mu} \left( \frac{\partial p}{\partial z} - \gamma \frac{\partial Z}{\partial z} \right). \end{aligned} \quad (2.2.3)$$

Ertekin et al. (2001) notes that the development of Darcy's law is based on the following assumptions:

- The flowing fluid is homogeneous, single-phase, and Newtonian.
- There is no chemical reaction between the fluid and the porous medium.
- The laminar flow conditions prevail.
- The permeability is a property of the porous medium that is independent of the pressure, temperature and flowing fluid.
- There is no slipping effect (Klinkenberg phenomenon).
- There are no electrokinetic effects.

## 2.3 Equation of State

An equation of state relates the specific mass of a fluid with its pressure, temperature, and composition. One way to perform this relation is by utilizing the formation volume factor,  $B$ . Also abbreviated as FVF, the formation volume factor is defined as the ratio of the specific mass of the fluid in surface conditions,  $\rho_{sc}$ , to its specific mass in a given state of pressure and temperature in the formation. Mathematically:

$$B = \frac{\rho_{sc}}{\rho}. \quad (2.3.1)$$

Thus, the single-phase flow equation utilizes the FVF as its form to relate the volume of the fluid with its conditions.

## 2.4 Compressibility

A fluid is classified as incompressible if the effects of pressure in its specific mass are zero or negligible. It is considered slightly compressible if its compressibility, defined by Eq. 2.4.1, is small and constant for small pressure gradients. In other words, for small changes of pressure, its volume variates at a constant rate. Finally, the fluid is considered compressible if its compressibility can not be assumed to be constant for pressure variations. Thus, changing the pressure in a compressible fluid will imply a considerable variation in its volume. The isothermal compressibility of a homogeneous material,  $c_j$ , is the fractional change of its volume  $V_j$  at constant temperature  $T$ , or:

$$c_j = -\frac{1}{V_j} \frac{\partial V_j}{\partial p} \Big|_T. \quad (2.4.1)$$

In terms of specific mass:

$$c_j = \frac{1}{\rho} \frac{\partial \rho}{\partial p} \Big|_T. \quad (2.4.2)$$

For the case of water:

$$c_w = \frac{1}{\rho_w} \frac{\partial \rho_w}{\partial p} \Big|_T. \quad (2.4.3)$$

where  $c_w$  is the water compressibility and  $\rho_w$  is its specific mass. Moreover, considering  $V_r$  the volume of the solid rock material, the rock matrix compressibility  $c_r$  is defined as:

$$c_r = -\frac{1}{V_r} \frac{\partial V_r}{\partial p} \Big|_T. \quad (2.4.4)$$

Analogously, the pore volume compressibility  $c_p$  relates the fractional change in pore volume  $V_p$  of a rock with a pressure variation:

$$c_p = -\frac{1}{V_p} \frac{\partial V_p}{\partial p} \Big|_T. \quad (2.4.5)$$

According to Ahmed (1946), the Eq. 2.4.5 can also be expressed in terms of porosity, considering that this property gets higher with an increase of pore pressure:

$$c_p = \frac{1}{\phi} \frac{\partial \phi}{\partial p} \Big|_T. \quad (2.4.6)$$

The formation compressibility  $c_f$  is used to describe the total compressibility in the formation. Since for most of the times, the pore compressibility is significantly higher than the rock matrix compressibility, it is possible to define:

$$c_f = c_p = \frac{1}{\phi} \frac{\partial \phi}{\partial p} \Big|_T. \quad (2.4.7)$$

Finally, the total reservoir compressibility  $c_t$  is defined by the expression:

$$c_t = S_o c_o + S_w c_w + S_g c_g + c_f. \quad (2.4.8)$$

Since the problem considers single-phase flow, the Eq. 2.4.8 can be reduced to:

$$c_t = S_o c_o + c_f. \quad (2.4.9)$$

This simulator has been developed considering the most general case in fluid compressibility, which is the compressible fluid. Notwithstanding, it could also be utilized to describe slightly compressible and incompressible fluids, which can be seen just as particular cases of the same mathematical formulation.

## 2.5 Porosity

The porosity of a rock is dependent on the pressure upon it. When the formation experiences higher external stress, it is compacted, leading to a decrease of porous space. The porosity in a given formation can be related to the pressure by the Eq. 2.4.7. This equation is based on the assumption that the formation compressibility does not change for small variations of pressure. Rearranging it:

$$\frac{\partial \phi}{\partial p} = \phi c_f. \quad (2.5.1)$$

Integrating the equation from a porosity  $\phi_0$  relative to a pressure  $P_0$  to a porosity  $\phi$  relative to a pressure  $P$ :

$$\phi = \int_{P_0}^P \phi c_f dp, \quad (2.5.2)$$

$$\phi = \phi_0^{c_f(P-P_0)}. \quad (2.5.3)$$

Expanding in Taylor's series and truncating the first term, the porosity could be finally approximated by:

$$\phi \approx \phi_0[1 + c_f(P - P_0)]. \quad (2.5.4)$$

For each cell, this simulator considers  $\phi_0$  as its initial porosity value, at time zero. This porosity value is related to the initial pressure in the cell,  $P_0$ . Then, for other values of pressure at different time steps, the porosity value of the cell is calculated using the Eq. 2.5.4.

## 2.6 Single-Phase Flow Equation

After defining the continuity equation, a constitutive relation (Darcy's law), and an equation of state (FVF), it is possible to assemble them to define the single-phase flow equation. Applying Darcy's law, Eq. 2.2.3, in the continuity equation, Eq. 2.1.9:

$$\frac{\partial}{\partial x} \left[ \rho \beta_c \frac{A_x k_x}{\mu} \frac{\partial(p - \gamma Z)}{\partial x} \right] \Delta x + \frac{\partial}{\partial y} \left[ \rho \beta_c \frac{A_y k_y}{\mu} \frac{\partial(p - \gamma Z)}{\partial y} \right] \Delta y + \frac{\partial}{\partial z} \left[ \rho \beta_c \frac{A_z k_z}{\mu} \frac{\partial(p - \gamma Z)}{\partial z} \right] \Delta z + \frac{q_m}{\alpha_c} = \frac{V_b}{\alpha_c} \frac{\partial}{\partial t} (\phi \rho). \quad (2.6.1)$$

The mass flow rate can be described as:

$$q_m = \alpha_c q \rho. \quad (2.6.2)$$

Utilizing the definition of formation volume factor, Eq. 2.3.1, for considering the volumes in surface conditions, as well as applying the Eq. 2.6.2 in the Eq. 2.6.1:

$$\frac{\partial}{\partial x} \left[ \rho_{sc} \beta_c \frac{A_x k_x}{\mu B} \frac{\partial(p - \gamma Z)}{\partial x} \right] \Delta x + \frac{\partial}{\partial y} \left[ \rho_{sc} \beta_c \frac{A_y k_y}{\mu B} \frac{\partial(p - \gamma Z)}{\partial y} \right] \Delta y + \frac{\partial}{\partial z} \left[ \rho_{sc} \beta_c \frac{A_z k_z}{\mu B} \frac{\partial(p - \gamma Z)}{\partial z} \right] \Delta z + q_{sc} \rho_{sc} = \frac{V_b}{\alpha_c} \frac{\partial}{\partial t} \left( \frac{\rho_{sc} \phi}{B} \right), \quad (2.6.3)$$

where  $q_{sc}$  is the well flow rate at surface conditions.  $\rho_{sc}$  is a constant and therefore can be eliminated in all terms of the equation:

$$\frac{\partial}{\partial x} \left[ \beta_c \frac{A_x k_x}{\mu B} \frac{\partial(p - \gamma Z)}{\partial x} \right] \Delta x + \frac{\partial}{\partial y} \left[ \beta_c \frac{A_y k_y}{\mu B} \frac{\partial(p - \gamma Z)}{\partial y} \right] \Delta y + \frac{\partial}{\partial z} \left[ \beta_c \frac{A_z k_z}{\mu B} \frac{\partial(p - \gamma Z)}{\partial z} \right] \Delta z + q_{sc} = \frac{V_b}{\alpha_c} \frac{\partial}{\partial t} \left( \frac{\phi}{B} \right). \quad (2.6.4)$$

Finally, Eq. 2.6.4 is the single-phase flow equation in Cartesian coordinates. It constitutes a partial-differential equation and has a nonlinearity which can not be solved analytically (except for some individual cases). The next chapter discusses how it will be discretized and linearized for enabling it to be solved numerically.

# Chapter 3

## Numerical Formulation

The previous chapter has shown the mathematical formulation for the single-phase flow equation, Eq. 2.6.4. This chapter will show its discretization for solving it numerically. This discretization will be done by the finite-differences method, which, according to Ertekin et al. (2001), is the most widely utilized method by the industry. It consists of approximating the derivatives by finite differences, as illustrated in Figure 3.1:

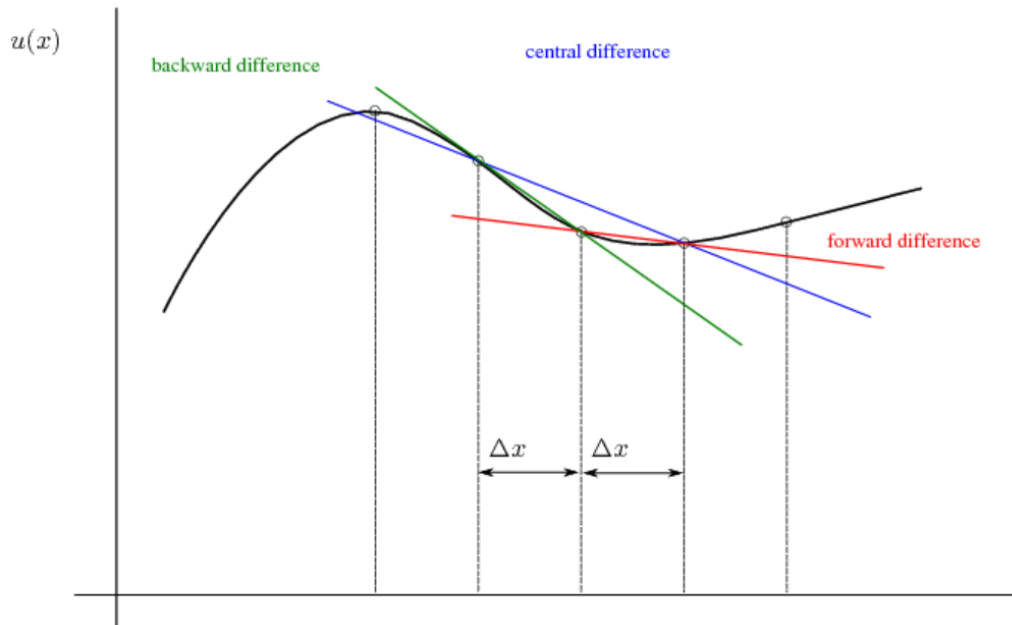


Figure 3.1: Illustration of three finite differences methods: central difference, forward difference, and backward difference. Source: Heinzl (1988).

For a given  $f(x)$  function, its first-order derivative is defined as:

$$f'(x) = \lim_{\Delta x \rightarrow 0} \frac{f(x + \Delta x) - f(x)}{\Delta x}. \quad (3.0.1)$$

Assuming  $\Delta x$  having a fixed, non-zero value, this limit can be approximated by:

$$f'(x) \approx \frac{f(x + \Delta x) - f(x)}{\Delta x}. \quad (3.0.2)$$

This is a finite-difference approach known as the forward difference method, since a posterior value,  $x + \Delta x$ , is utilized for the approximation. Another way of discretizing the Eq. 3.0.1 is:

$$f'(x) \approx \frac{f(x) - f(x - \Delta x)}{\Delta x}, \quad (3.0.3)$$

this, on the other hand, is known as the backward difference method. In this approach, the previous value  $x - \Delta x$  is utilized for calculating  $f'(x)$ . There is also the central difference method, in which both the  $x - \Delta x$  and  $x + \Delta x$  are utilized for approximating the derivative:

$$f'(x) \approx \frac{f(x + \Delta x) - f(x - \Delta x)}{2\Delta x}, \quad (3.0.4)$$

For the simulator developed in this project, the spatial derivatives will be approximated with the central difference, and the time derivatives will be dealt with the backward difference. This approach is known as the BTCS method (backward-time, central-space) and characterizes an implicit model that, according to Ertekin et al. (2001), is unconditionally stable.

### 3.1 Grid Definition

After doing a superimposition of a finite-block grid in a petroleum reservoir model, it is possible to approximate the continuum distribution of its properties (e.g., pressure, porosity, and permeability) by the average value of them inside each grid block. The grid-type utilized in the simulator will be the block-centered grid. Ertekin et al. (2001) shows the utilization of this type of grid for a unidimensional flow, as depicted in Figure 3.2. For a simple

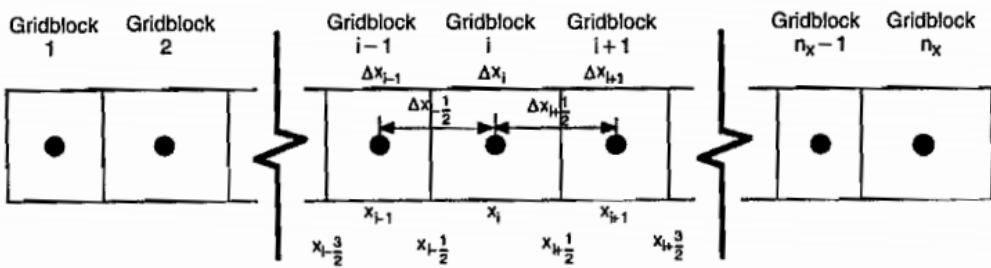


Figure 3.2: Unidimensional example of a block-centered grid. Source: Ertekin et al. (2001).

illustration, a unidimensional reservoir is represented by a grid composed of  $n_x$  blocks of predetermined dimensions,  $\Delta x_i$ , not necessarily equals, which must satisfy:

$$\sum_{i=1}^{n_x} \Delta x = L_x. \quad (3.1.1)$$

In other words, the sum of the blocks' length should be equal to the reservoir length. Once the blocks are defined, the points in that the pressures are calculated are disposed of in their interior. In Cartesian coordinates, those points coincide with their center. The boundaries of a determined block with index  $i$  are defined as  $x_{i-1/2}$  and  $x_{i+1/2}$ , and their center is designated as  $x_i$ . Therefore, the following relations are valid for the block properties:

$$x_i = (x_{i-1/2} + x_{i+1/2}) \quad (3.1.2)$$

and

$$x_i = x_{i+1/2} - x_{i-1/2}. \quad (3.1.3)$$

Expanding this idea for a tridimensional, parallelepipedal reservoir, we can model it by dividing the grid into small volumetric elements that fit into the

entire volume of the reservoir. For a grid block with indexes  $i, j, k$ , its center is defined in the point  $(x_{i,j,k}, y_{i,j,k}, z_{i,j,k})$ . Thus, the dimensions of this grid block would be  $\Delta x_{i,j,k}$ ,  $\Delta y_{i,j,k}$ ,  $\Delta z_{i,j,k}$  and its volume  $V_{i,j,k}$ :

$$V_{i,j,k} = \Delta x_{i,j,k} \Delta y_{i,j,k} \Delta z_{i,j,k}. \quad (3.1.4)$$

Therefore:

$$\sum_{i=1}^{n_x} \sum_{j=1}^{n_y} \sum_{k=1}^{n_z} \Delta x_{i,j,k} \Delta y_{i,j,k} \Delta z_{i,j,k} = V_{res}. \quad (3.1.5)$$

Figure 3.3 illustrates such a model. As one can see, the grid blocks are allowed

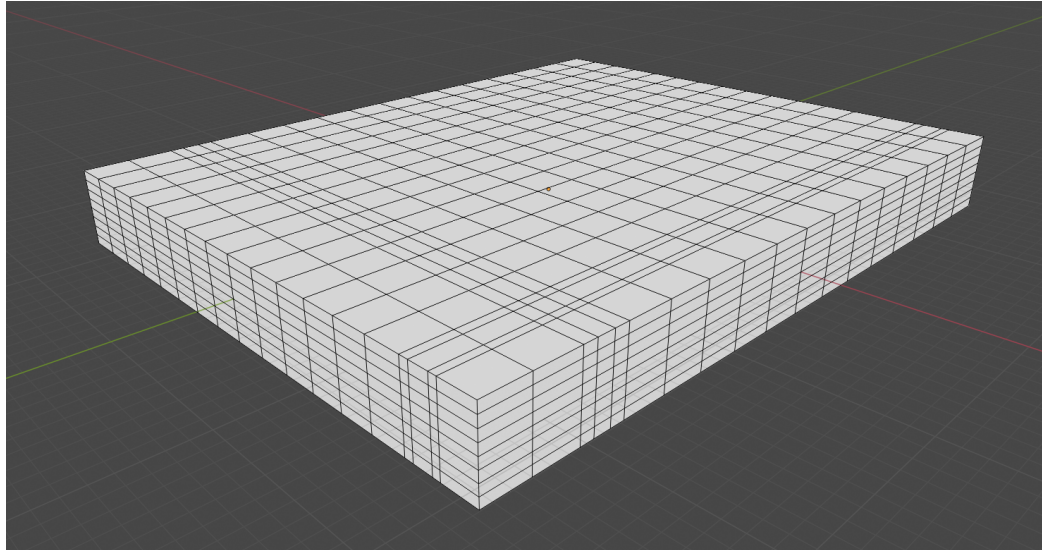


Figure 3.3: Example of a tridimensional grid representing an artificial, par-allelepipedal reservoir.

to have different sizes of  $\Delta x$ ,  $\Delta y$ , and  $\Delta z$ , and they don't have to be equal from one grid block to another.

## 3.2 Discretization in Space

After the grid type has been defined, it is then possible to follow ahead with the Eq. 2.6.4 discretization. Considering the term of the equation regarding the spatial derivative in the  $x$  direction:

$$\frac{\partial}{\partial x} \left( \beta_c \frac{A_x k_x}{\mu B} \frac{\partial p}{\partial x} \right) \Delta x \quad (3.2.1)$$

Following the Ertekin et al. (2001) approach of approximating it by central differences, as shown in Eq. 3.0.4:

$$\begin{aligned} & \frac{\partial}{\partial x} \left( \beta_c \frac{A_x k_x}{\mu B} \frac{\partial p}{\partial x} \right)_i \Delta x \\ & \approx \frac{1}{\Delta x_i} \left[ \left( \beta_c \frac{A_x k_x}{\mu B} \frac{\partial p}{\partial x} \right)_{i+1/2} - \left( \beta_c \frac{A_x k_x}{\mu B} \frac{\partial p}{\partial x} \right)_{i-1/2} \right] \Delta x_i \end{aligned} \quad (3.2.2)$$

That resulted not in an equation, but an approximation. However, the approximation sign will be substituted for an equal sign in the following developments for simplicity. After performing this substitution and doing some rearrangements:

$$\begin{aligned} & \frac{1}{\Delta x_i} \left[ \left( \beta_c \frac{A_x k_x}{\mu B} \frac{\partial p}{\partial x} \right)_{i+1/2} - \left( \beta_c \frac{A_x k_x}{\mu B} \frac{\partial p}{\partial x} \right)_{i-1/2} \right] \Delta x_i \\ & = \left( \beta_c \frac{A_x k_x}{\mu B} \right)_{i+1/2} \left( \frac{\partial p}{\partial x} \right)_{i+1/2} - \left( \beta_c \frac{A_x k_x}{\mu B} \right)_{i-1/2} \left( \frac{\partial p}{\partial x} \right)_{i-1/2} \end{aligned} \quad (3.2.3)$$

For the derivative terms inside the brackets, their central-differences approximations are:

$$\left( \frac{\partial p}{\partial x} \right)_{i+1/2} = \frac{p_{i+1} - p_i}{x_{i+1} - x_i} = \frac{p_{i+1} - p_i}{\Delta x_{i+1/2}} \quad (3.2.4)$$

and:

$$\left( \frac{\partial p}{\partial x} \right)_{i-1/2} = \frac{p_i - p_{i-1}}{x_{i+1} - x_i} = \frac{p_i - p_{i-1}}{\Delta x_{i-1/2}}. \quad (3.2.5)$$

Substituting those into Eq. 3.2.3:

$$\begin{aligned} & \left( \beta_c \frac{A_x k_x}{\mu B} \right)_{i+1/2} \left( \frac{\partial p}{\partial x} \right)_{i+1/2} - \left( \beta_c \frac{A_x k_x}{\mu B} \right)_{i-1/2} \left( \frac{\partial p}{\partial x} \right)_{i-1/2} \\ & = \left( \beta_c \frac{A_x k_x}{\mu B \Delta x} \right)_{i+1/2} (p_{i+1} - p_i) - \left( \beta_c \frac{A_x k_x}{\mu B \Delta x} \right)_{i-1/2} (p_i - p_{i-1}) \end{aligned} \quad (3.2.6)$$

This equation can be simplified even further by utilizing the definition of transmissibilities, as it is commonly done in the industry. The coefficients  $T_{x_{i+1/2}}$  and  $T_{x_{i-1/2}}$ , known as the transmissibilities of the porous medium, are defined as:

$$T_{x_{i+1/2}} = \left( \beta_c \frac{A_x k_x}{\mu B \Delta x} \right)_{i+1/2} \quad (3.2.7)$$

and

$$T_{x_{i-1/2}} = \left( \beta_c \frac{A_x k_x}{\mu B \Delta x} \right)_{i-1/2} \quad (3.2.8)$$

As indicated by their indexes, the transmissibilities are defined at the grid blocks' boundaries, since they are utilized for evaluating the flow between adjacent blocks. Those transmissibilities have pressure-dependent factors, notably the FVF ( $B$ ) and the viscosity ( $\mu$ ); as well as pressure-independent ones: the transversal area ( $A_x$ ), permeability ( $k_x$ ), grid block length ( $\Delta x$ ), and the transmissibility conversion factor ( $\beta_c$ ). Splitting the transmissibility into a pressure-dependent and a pressure-independent factor simplifies the computational process. The constant part can be calculated just one time for the entire simulation, and the pressure-dependent factor needs to be reevaluated at each iteration. Thus, rearranging the Eqs. 3.2.7 and 3.2.8, the transmissibilities could be rewritten as:

$$T_{x_{i+1/2}} = \beta_c \left( \frac{A_x k_x}{\Delta x} \right)_{i+1/2} \left( \frac{1}{\mu B} \right)_{i+1/2} = \beta_c G_{x_{i+1/2}} \left( \frac{1}{\mu B} \right)_{i+1/2}, \quad (3.2.9)$$

and

$$T_{x_{i-1/2}} = \beta_c \left( \frac{A_x k_x}{\Delta x} \right)_{i-1/2} \left( \frac{1}{\mu B} \right)_{i-1/2} = \beta_c G_{x_{i-1/2}} \left( \frac{1}{\mu B} \right)_{i-1/2}, \quad (3.2.10)$$

where  $G$  is the geometric transmissibility, representing the pressure-independent part. The pressure-dependent part can be calculated in function of the pressure at the grid blocks' faces, by interpolating the FVF and viscosity with a value of pressure for a given fluid. The next subchapters will discuss in more detail the determination of those pressure-dependent variables. Substituting the Eqs. 3.2.7 and 3.2.8 into Eq. 3.2.6:

$$\begin{aligned} & \left( \beta_c \frac{A_x k_x}{\mu B \Delta x} \right)_{i+1/2} (p_{i+1} - p_i) - \left( \beta_c \frac{A_x k_x}{\mu B \Delta x} \right)_{i-1/2} (p_i - p_{i-1}) \\ &= T_{x_{i+1/2}} (p_{i+1} - p_i) - T_{x_{i-1/2}} (p_i - p_{i-1}) \end{aligned} \quad (3.2.11)$$

Regarding the spatial derivative of the relative depth, its finite-difference approximation is:

$$\begin{aligned} \frac{\partial}{\partial x} \left( \beta_c \frac{A_x k_x}{\mu B} \gamma \frac{\partial Z}{\partial x} \right)_i \Delta x \\ \approx \frac{\gamma}{\Delta x_i} \left[ \left( \beta_c \frac{A_x k_x}{\mu B} \frac{\partial Z}{\partial x} \right)_{i+1/2} - \left( \beta_c \frac{A_x k_x}{\mu B} \frac{\partial Z}{\partial x} \right)_{i-1/2} \right] \Delta x_i \quad (3.2.12) \end{aligned}$$

It is possible to see that, except for the coefficient  $\gamma$ , the Eqs. 3.2.2 and 3.2.12 are analogous. Taking a similar procedure for Eq. 3.2.2:

$$\begin{aligned} \frac{\gamma}{\Delta x_i} \left[ \left( \beta_c \frac{A_x k_x}{\mu B} \frac{\partial Z}{\partial x} \right)_{i+1/2} - \left( \beta_c \frac{A_x k_x}{\mu B} \frac{\partial Z}{\partial x} \right)_{i-1/2} \right] \Delta x_i \\ = \gamma_{i+1/2} T_{x_{i+1/2}} (Z_{i+1} - Z_i) - \gamma_{i-1/2} T_{x_{i-1/2}} (Z_i - Z_{i-1}) \quad (3.2.13) \end{aligned}$$

Expanding the approximation of the spatial terms for the directions  $y$  and  $z$ , and utilizing the definition of transmissibility again:

$$\begin{aligned} \frac{\partial}{\partial y} \left( \beta_c \frac{A_y k_y}{\mu B} \gamma \frac{\partial Z}{\partial y} \right)_j \Delta y \\ = \gamma_{j+1/2} T_{y_{j+1/2}} (Z_{j+1} - Z_j) - \gamma_{j-1/2} T_{y_{j-1/2}} (Z_j - Z_{j-1}) \quad (3.2.14) \end{aligned}$$

and:

$$\begin{aligned} \frac{\partial}{\partial z} \left( \beta_c \frac{A_z k_z}{\mu B} \gamma \frac{\partial Z}{\partial z} \right)_k \Delta z \\ = \gamma_{k+1/2} T_{z_{k+1/2}} (Z_{k+1} - Z_k) - \gamma_{k-1/2} T_{z_{k-1/2}} (Z_k - Z_{k-1}) \quad (3.2.15) \end{aligned}$$

After those approximations are applied in the single-phase flow equation, Eq. 2.6.4, that partial-differential equation is then in the process of being substituted by a system of algebraic equations in the form:

$$\begin{aligned} & T_{i+1/2,j,k} (p_{i+1,j,k} - p_{i,j,k}) - T_{i-1/2,j,k} (p_{i,j,k} - p_{i-1,j,k}) + \\ & T_{i,j+1/2,k} (p_{i,j+1,k} - p_{i,j,k}) - T_{i,j-1/2,k} (p_{i,j,k} - p_{i,j-1,k}) + \\ & T_{i,j,k+1/2} (p_{i,j,k+1} - p_{i,j,k}) - T_{i,j,k-1/2} (p_{i,j,k} - p_{i,j,k-1}) + q_{sc_{i,j,k}} = \\ & \gamma_{i+1/2,j,k} T_{i+1/2,j,k} (Z_{i+1,j,k} - Z_{i,j,k}) - \gamma_{i-1/2,j,k} T_{i-1/2,j,k} (Z_{i,j,k} - Z_{i-1,j,k}) + \\ & \gamma_{i,j+1/2,k} T_{i,j+1/2,k} (Z_{i,j+1,k} - Z_{i,j,k}) - \gamma_{i,j-1/2,k} T_{i,j-1/2,k} (Z_{i,j,k} - Z_{i,j-1,k}) + \\ & \gamma_{i,j,k+1/2} T_{i,j,k+1/2} (Z_{i,j,k+1} - Z_{i,j,k}) - \gamma_{i,j,k-1/2} T_{i,j,k-1/2} (Z_{i,j,k} - Z_{i,j,k-1}) + \\ & \frac{V_b}{\alpha_c} \frac{\partial}{\partial t} \left( \frac{\phi}{B} \right). \quad (3.2.16) \end{aligned}$$

The indexes  $i, j, k$  are utilized since this equation has to be calculated for each grid block of the model. That spans a system of  $n_x n_y n_z$  equations, where  $n_x$ ,  $n_y$ , and  $n_z$  are the number of grid blocks in each direction. However, Eq. 3.2.16 is still not complete since the time derivatives:

$$\frac{V_b}{\alpha_c} \frac{\partial}{\partial t} \left( \frac{\phi}{B} \right),$$

have not been discretized yet. The next subchapter will proceed with its discretization.

### 3.3 Discretization in Time

The previous section has shown how the central-differences method has been utilized for approximating the spatial derivatives of the single-phase flow equation. On the other hand, the time derivatives will be approximated by backward difference. The approximation by backward difference of a derivative related to time  $t^{n+1}$  is:

$$\frac{\partial p}{\partial t} \approx \frac{p(t^{n+1}) - p(t^n)}{\Delta t}. \quad (3.3.1)$$

The following definitions will be utilized for the sake of simplicity:

$$p^n = p(t^n) \quad (3.3.2)$$

and

$$p^{n+1} = p(t^{n+1}). \quad (3.3.3)$$

Therefore, for a block with indexes  $i, j, k$ :

$$\frac{\partial p_{i,j,k}}{\partial t} \approx \frac{p_{i,j,k}^{n+1} - p_{i,j,k}^n}{\Delta t}. \quad (3.3.4)$$

Going back to the right term of the single-phase flow equation, Eq. 2.6.4. Utilizing the chain rule of differentiation:

$$\frac{V_b}{\alpha_c} \frac{\partial}{\partial t} \left( \frac{\phi}{B} \right) = \frac{V_b}{\alpha_c} \frac{\partial}{\partial p} \left( \frac{\phi}{B} \right) \frac{\partial p}{\partial t}. \quad (3.3.5)$$

A new variable  $\Gamma$  will be defined for facilitating the numerical calculations:

$$\Gamma = \frac{V_b}{\alpha_c} \frac{\partial}{\partial p} \left( \frac{\phi}{B} \right). \quad (3.3.6)$$

Expanding the derivatives of  $\phi/B$  in relation to the pressure and considering a constant  $c_f$  for small pressure changes:

$$\Gamma_{i,j,k}^{n,n+1} = \frac{V_{b_{i,j,k}}}{\alpha_c} \left[ \frac{\phi_{i,j,k}^{n+1} c_f}{B_{i,j,k}^{n+1}} + \frac{\phi_{i,j,k}^n (B_{i,j,k}^n / B_{i,j,k}^{n+1} - 1)}{(p_{i,j,k}^{n+1} - p_{i,j,k}^n)} \right]. \quad (3.3.7)$$

The index  $n, n + 1$  in  $\Gamma$  means that some parameters in the  $\Gamma$  definition are evaluated at  $n$  and others at  $n + 1$ . Utilizing the concept of the backward-difference method shown in Eq. 3.0.3.

$$\frac{V_{b_{i,j,k}}}{\alpha_c} \left[ \frac{\phi_{i,j,k}^{n+1} c_f}{B_{i,j,k}^{n+1}} + \frac{\phi_{i,j,k}^n (B_{i,j,k}^n / B_{i,j,k}^{n+1} - 1)}{(p_{i,j,k}^{n+1} - p_{i,j,k}^n)} \right] \frac{\partial p}{\partial t} = \Gamma_{i,j,k}^{n,n+1} \frac{(p_{i,j,k}^{n+1} - p_{i,j,k}^n)}{\Delta t}. \quad (3.3.8)$$

This is the discretized form of the time-dependent term of the single-phase flow equation. Applying this definition back in Eq. 3.2.16:

$$\begin{aligned}
 & T_{i+1/2,j,k}^{n+1}(p_{i+1,j,k}^{n+1} - p_{i,j,k}^{n+1}) - T_{i-1/2,j,k}^{n+1}(p_{i,j,k}^{n+1} - p_{i-1,j,k}^{n+1}) + \\
 & T_{i,j+1/2,k}^{n+1}(p_{i,j+1,k}^{n+1} - p_{i,j,k}^{n+1}) - T_{i,j-1/2,k}^{n+1}(p_{i,j,k}^{n+1} - p_{i,j-1,k}^{n+1}) + \\
 & T_{i,j,k+1/2}^{n+1}(p_{i,j,k+1}^{n+1} - p_{i,j,k}^{n+1}) - T_{i,j,k-1/2}^{n+1}(p_{i,j,k}^{n+1} - p_{i,j,k-1}^{n+1}) + q_{sc,i,j,k}^{n+1} = \\
 & \gamma_{i+1/2,j,k}^{n+1} T_{i+1/2,j,k}^{n+1} (z_{r_{i+1,j,k}}^{n+1} - z_{r_{i,j,k}}^{n+1}) - \gamma_{i-1/2,j,k}^{n+1} T_{i-1/2,j,k}^{n+1} (z_{r_{i,j,k}}^{n+1} - z_{r_{i-1,j,k}}^{n+1}) + \\
 & \gamma_{i,j+1/2,k}^{n+1} T_{i,j+1/2,k}^{n+1} (z_{r_{i,j+1,k}}^{n+1} - z_{r_{i,j,k}}^{n+1}) - \gamma_{i,j-1/2,k}^{n+1} T_{i,j-1/2,k}^{n+1} (z_{r_{i,j,k}}^{n+1} - z_{r_{i,j-1,k}}^{n+1}) + \\
 & \gamma_{i,j,k+1/2}^{n+1} T_{i,j,k+1/2}^{n+1} (z_{r_{i,j,k+1}}^{n+1} - z_{r_{i,j,k}}^{n+1}) - \gamma_{i,j,k-1/2}^{n+1} T_{i,j,k-1/2}^{n+1} (z_{r_{i,j,k}}^{n+1} - z_{r_{i,j,k-1}}^{n+1}) + \\
 & \frac{\Gamma_{i,j,k}^{n,n+1}}{\Delta t} (p_{i,j,k}^{n+1} - p_{i,j,k}^n). \tag{3.3.9}
 \end{aligned}$$

Finally, this is the single-phase flow equation discretized by the BTCS method. It is necessary to set boundary conditions for the solution of this equation. The problem considers a sealed reservoir, which means a model with a flow rate equals zero in the boundaries. That can be modeled by setting the transmissibilities equal to zero for the grid block's faces at the reservoir boundaries. The next section will show another form of representing 3.3.9 for its simplification.

### 3.4 Matrix Notation

Ertekin et al. (2001) defines a matrix coefficients notation that simplifies the utilization of the Eq.3.3.9. Rearranging the equation:

$$\begin{aligned}
 & T_{i,j,k+1/2}^{n+1} p_{i,j,k+1}^{n+1} + T_{i,j+1/2,k}^{n+1} p_{i,j+1,k}^{n+1} + T_{i+1/2,j,k}^{n+1} p_{i+1,j,k}^{n+1} - \\
 & \left( \frac{\Gamma_{i,j,k}^{n+1}}{\Delta t} + T_{i,j,k+1/2}^{n+1} + T_{i,j+1/2,k}^{n+1} + T_{i+1/2,j,k}^{n+1} + \right. \\
 & \left. T_{i,j,k-1/2}^{n+1} + T_{i,j-1/2,k}^{n+1} + T_{i-1/2,j,k}^{n+1} \right) p_{i,j,k}^{n+1} + \\
 & T_{i,j,k-1/2}^{n+1} p_{i,j,k-1}^{n+1} + T_{i,j-1/2,k}^{n+1} p_{i,j-1,k}^{n+1} + T_{i-1/2,j,k}^{n+1} p_{i-1,j,k}^{n+1} = \\
 & \gamma_{i+1/2,j,k}^{n+1} T_{i+1/2,j,k}^{n+1} (z_{r_{i,j,k}}^{n+1} - z_{r_{i,j,k}}^{n+1}) - \gamma_{i-1/2,j,k}^{n+1} T_{i-1/2,j,k}^{n+1} (z_{r_{i,j,k}}^{n+1} - z_{r_{i,j-1,k}}^{n+1}) + \\
 & \gamma_{i,j+1/2,k}^{n+1} T_{i,j+1/2,k}^{n+1} (z_{r_{i,j+1,k}}^{n+1} - z_{r_{i,j,k}}^{n+1}) - \gamma_{i,j-1/2,k}^{n+1} T_{i,j-1/2,k}^{n+1} (z_{r_{i,j,k}}^{n+1} - z_{r_{i,j-1,k}}^{n+1}) + \\
 & \gamma_{i,j,k+1/2}^{n+1} T_{i,j,k+1/2}^{n+1} (z_{r_{i,j,k+1}}^{n+1} - z_{r_{i,j,k}}^{n+1}) - \gamma_{i,j,k-1/2}^{n+1} T_{i,j,k-1/2}^{n+1} (z_{r_{i,j,k}}^{n+1} - z_{r_{i,j,k-1}}^{n+1}) - \\
 & \frac{\Gamma_{i,j,k}^{n,n+1}}{\Delta t} p_{i,j,k}^n - q_{sc_{i,j,k}}^{n+1} \tag{3.4.1}
 \end{aligned}$$

By looking at this equation, one can see that the transmissibilities are evaluated in different faces of a grid block of indexes  $i, j, k$ . The idea of the matrix coefficient notation is to assign the transmissibilities evaluated in each face with a letter that symbolizes the face. Figure 3.4 shows the definition of some of those new coefficients. The following set of equations show the definition

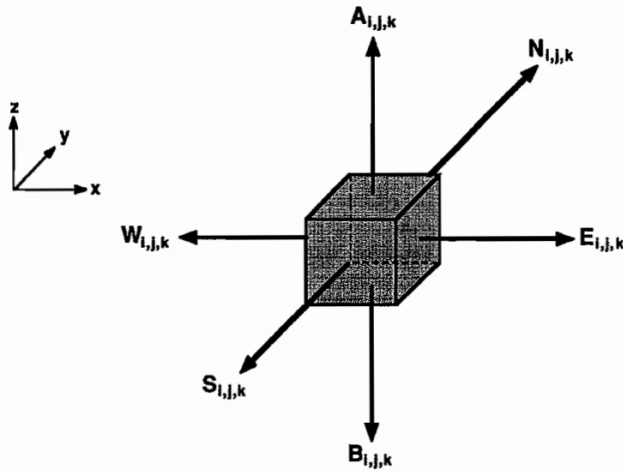


Figure 3.4: Illustration of the matrix coefficients utilized for representing the transmissibilities. Source: Ertekin et al. (2001).

of those new coefficients:

$$W_{i,j,k}^{n+1} = T_{i-1/2,j,k}^{n+1}, \quad (3.4.2)$$

$$E_{i,j,k}^{n+1} = T_{i+1/2,j,k}^{n+1}, \quad (3.4.3)$$

$$S_{i,j,k}^{n+1} = T_{i,j-1/2,k}^{n+1}, \quad (3.4.4)$$

$$N_{i,j,k}^{n+1} = T_{i,j+1/2,k}^{n+1}, \quad (3.4.5)$$

$$B_{i,j,k}^{n+1} = T_{i,j,k+1/2}^{n+1}, \quad (3.4.6)$$

$$A_{i,j,k}^{n+1} = T_{i,j,k-1/2}^{n+1}, \quad (3.4.7)$$

$$C_{i,j,k}^{n+1} = - \left( \frac{\Gamma_{i,j,k}^{n,n+1}}{\Delta t} + W_{i,j,k}^{n+1} + E_{i,j,k}^{n+1} + S_{i,j,k}^{n+1} + N_{i,j,k}^{n+1} + B_{i,j,k}^{n+1} + A_{i,j,k}^{n+1} \right), \quad (3.4.8)$$

$$W_{G_{i,j,k}}^{n+1} = \gamma_{i-1/2,j,k}^{n+1} T_{i-1/2,j,k}^{n+1}, \quad (3.4.9)$$

$$E_{G_{i,j,k}}^{n+1} = \gamma_{i+1/2,j,k}^{n+1} T_{i+1/2,j,k}^{n+1}, \quad (3.4.10)$$

$$S_{G_{i,j,k}}^{n+1} = \gamma_{i,j-1/2,k}^{n+1} T_{i,j-1/2,k}^{n+1}, \quad (3.4.11)$$

$$N_{G_{i,j,k}}^{n+1} = \gamma_{i,j+1/2,k}^{n+1} T_{i,j+1/2,k}^{n+1}, \quad (3.4.12)$$

$$B_{G_{i,j,k}}^{n+1} = \gamma_{i,j,k+1/2}^{n+1} T_{i,j,k+1/2}^{n+1}, \quad (3.4.13)$$

$$A_{G_{i,j,k}}^{n+1} = \gamma_{i,j,k-1/2}^{n+1} T_{i,j,k-1/2}^{n+1}, \quad (3.4.14)$$

$$C_{G_{i,j,k}}^{n+1} = - \left( W_{G_{i,j,k}}^{n+1} + E_{G_{i,j,k}}^{n+1} + S_{G_{i,j,k}}^{n+1} + N_{G_{i,j,k}}^{n+1} + B_{G_{i,j,k}}^{n+1} + A_{G_{i,j,k}}^{n+1} \right) \quad (3.4.15)$$

and

$$\begin{aligned} Q_{i,j,k}^{n,n+1} = & - \left( \frac{\Gamma_{i,j,k}^{n,n+1}}{\Delta t} p_{i,j,k}^n + q_{sc_{i,j,k}} - W_{G_{i,j,k}}^{n+1} Z_{i-1/2,j,k}^{n+1} - E_{G_{i,j,k}}^{n+1} Z_{i+1/2,j,k}^{n+1} \right. \\ & \left. - S_{G_{i,j,k}}^{n+1} Z_{i,j-1/2,k}^{n+1} - N_{G_{i,j,k}}^{n+1} Z_{i,j+1/2,k}^{n+1} - B_{G_{i,j,k}}^{n+1} Z_{i,j,k-1/2}^{n+1} - A_{G_{i,j,k}}^{n+1} Z_{i,j,k+1/2}^{n+1} \right). \end{aligned} \quad (3.4.16)$$

Applying those new definitions in the 3.3.9:

$$\begin{aligned} & W_{i,j,k}^{n+1} p_{i-1,j,k}^{n+1} + E_{i,j,k}^{n+1} p_{i+1,j,k}^{n+1} + S_{i,j,k}^{n+1} p_{i,j-1,k}^{n+1} \\ & + N_{i,j,k}^{n+1} p_{i,j+1,k}^{n+1} + B_{i,j,k}^{n+1} p_{i,j,k-1}^{n+1} + A_{i,j,k}^{n+1} p_{i,j,k+1}^{n+1} + C_{i,j,k}^{n+1} p_{i,j,k}^{n+1} = Q_{i,j,k}^{n,n+1}. \end{aligned} \quad (3.4.17)$$

This is the single-phase flow equation discretized with the BTCS method and simplified with the Ertekin et al. (2001) matrix coefficients notation. For calculating the pressure at the next time step,  $p^{n+1}$ , the simulator has to compute this equation for every grid block, for the entire model. Thus, it spans a system of  $n$  equations, in which  $n$  is the total number of the

blocks in the grid. However, this system of equations is non-linear because the coefficients  $W, E, S, N, A, B, C, Q$  have terms that depend on the pressure. The next subchapter will show how this problem will be handled by transforming this non-linear system of equations into a linear one.

### 3.5 Linearization

As discussed in the previous subchapter, the non-linear system of equations represented by Eq. 3.3.9 needs to be linearized for enabling it to be solved by methods of linear algebra. There are several different ways to do that, but this project approaches it by what Ertekin et al. (2001) describes as the simple iteration of the transmissibility terms. There are more efficient techniques of linearization for achieving a faster convergency, like the Newton-Raphson method, but their implementation is more complex and doesn't fit in the initial scope of this project. In terms of accuracy, there is no significant difference between those methods, as shown in the results when compared to industry-standard software.

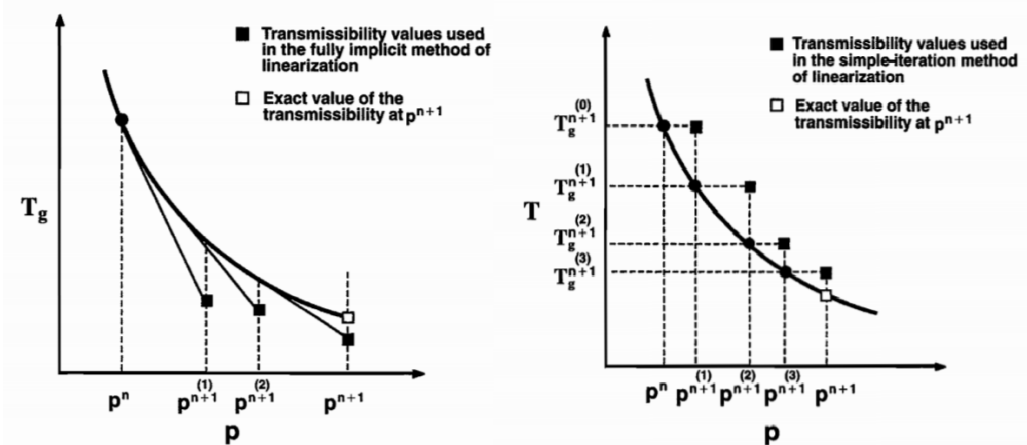


Figure 3.5: The convergence of the Newton-Raphson method in comparison with the Simple Iteration of the Transmissibility Terms. Source: Ertekin et al. (2001).

The problem described at the end of the previous subchapter is that the pressure coefficients in Eq. 3.3.9 are also pressure-dependent variables, thus the resultant system of equation is non-linear. The simple iteration described by Ertekin et al. (2001) consists of evaluating those dependent variables utilizing the pressure value of one iteration level bellow the pressure level used for solving the linear system. By the definition of transmissibility from the Eqs. 3.2.9 and 3.2.10, using  $\nu$  is the iteration index:

$$T_{i\pm 1/2,j,k}^{n+1} \approx T_{i\pm 1/2,j,k}^{(\nu)} = \beta_c \left( \frac{A_x k_x}{\Delta x} \right)_{i\pm 1/2,j,k} \left( \frac{1}{\mu B} \right)_{i\pm 1/2,j,k}^{n+1}. \quad (3.5.1)$$

Using the concept of geometric factor,  $G_{i,j,k}$ , defined in Eq. 3.2.10:

$$T_{i \pm 1/2, j, k}^{(\nu)} = \beta_c G_{i \pm 1/2, j, k} \left( \frac{1}{\mu B} \right)_{i \pm 1/2, j, k}^{n+1}. \quad (3.5.2)$$

The variables inside the transmissibility factor are evaluated in the grid blocks' faces, while the grid block properties are assigned in the center of the blocks for a block-centered grid. Therefore, it is necessary to determine the properties at the blocks' faces by applying some averaging technique. The method utilized in this project has been the harmonic averaging,  $A_{-1}$ , which is recommended by Ertekin et al. (2001) and defined as:

$$\frac{1}{A_{-1}(a)} = \frac{1}{n} \left( \frac{1}{a_1} + \frac{1}{a_2} + \dots + \frac{1}{a_n} \right), \quad (3.5.3)$$

where  $n$  is the number of the averaged property  $a$ . Thus, the geometric transmissibility at the face  $i + 1/2, j, k$  can be calculated by:

$$\frac{1}{G_{i+1/2, j, k}} = \frac{1}{A_{-1}(G_{i, j, k}, G_{i+1, j, k})} = \frac{1}{2} \left[ \left( \frac{\Delta x}{A_x k_x} \right)_{i, j, k} + \left( \frac{\Delta x}{A_x k_x} \right)_{i+1, j, k} \right], \quad (3.5.4)$$

$$\begin{aligned} \frac{1}{A_{-1}(G_{i, j, k}, G_{i+1, j, k})} &= \\ \frac{1}{2} \left[ \frac{\Delta x_{i+1, j, k} (A_{x_{i, j, k}} k_{x_{i, j, k}}) + \Delta x_{i, j, k} (A_{x_{i+1, j, k}} k_{x_{i+1, j, k}})}{A_{x_{i, j, k}} A_{x_{i+1, j, k}} K_{x_{i, j, k}} K_{x_{i+1, j, k}}} \right], \end{aligned} \quad (3.5.5)$$

$$\begin{aligned} G_{i+1/2, j, k} &= A_{-1}(G_{i, j, k}, G_{i+1, j, k}) = \\ \frac{2 A_{x_{i, j, k}} A_{x_{i+1, j, k}} K_{x_{i, j, k}} K_{x_{i+1, j, k}}}{\Delta x_{i+1, j, k} (A_{x_{i, j, k}} k_{x_{i, j, k}}) + \Delta x_{i, j, k} (A_{x_{i+1, j, k}} k_{x_{i+1, j, k}})}. \end{aligned} \quad (3.5.6)$$

The same approach can be utilized for calculating the geometric transmissibilities at the different faces of the grid blocks.

The software developed in this project requires a fluid table as a parameter for the simulation. This table should relate the pressure-dependent properties (FVF, viscosity, and specific weight) to a set of pressure values. Interpolation is done to obtain those properties at grid block's faces. Figures 3.6 to 3.8 show an example of relationships between pressure and those pressure-dependent properties, as well as a linear regression utilized for interpolating their values for a given pressure.

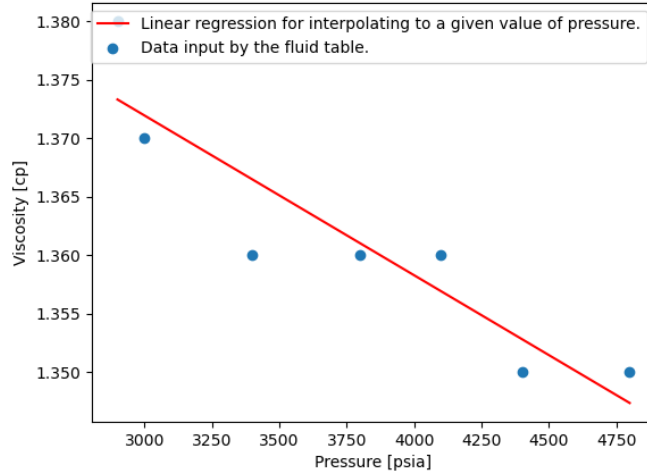


Figure 3.6: Example of a relationship between pressure and viscosity in a fluid model.

Thus, the pressure-dependent factor of the transmissibility can be written as:

$$\left(\frac{1}{\mu B}\right)_{i \pm 1/2, j, k}^{(n+1)} = \left(\frac{1}{\mu_{i \pm 1/2, j, k} B_{i \pm 1/2, j, k}}\right)^{(n+1)}. \quad (3.5.7)$$

The pressure at the grid block's faces will be determined by an arithmetic mean of the pressures at the center of the grid blocks:

$$p_{i \pm 1/2, j, k}^{(n+1)} = \frac{p_{i \pm 1/2, j, k}^{(n+1)} + p_{i, j, k}^{(n+1)}}{2}. \quad (3.5.8)$$

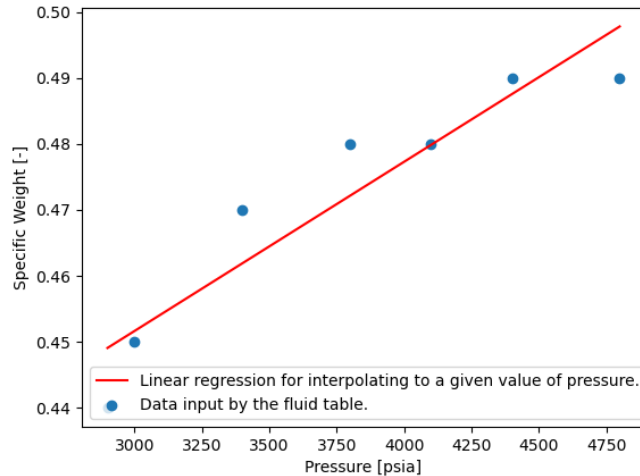


Figure 3.7: Example of a relationship between pressure and specific weight in a fluid model.

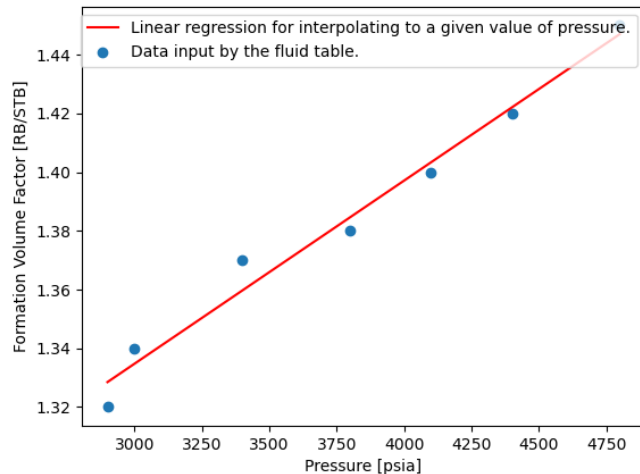


Figure 3.8: Example of a relationship between pressure and FVF in a fluid model.

After calculating those properties, it is then possible to obtain the transmissibilities in the iteration level  $\nu$ . Applying the iteration indexes in the Eq.

3.4.17:

$$W_{i,j,k}^{n+1} p_{i-1,j,k}^{n+1} + E_{i,j,k}^{n+1} p_{i+1,j,k}^{n+1} + S_{i,j,k}^{n+1} p_{i,j-1,k}^{n+1} + N_{i,j,k}^{n+1} p_{i,j+1,k}^{n+1} + B_{i,j,k}^{n+1} p_{i,j,k-1}^{n+1} + A_{i,j,k}^{n+1} p_{i,j,k+1}^{n+1} + C_{i,j,k}^{n+1} p_{i,j,k}^{n+1} = Q_{i,j,k}^{n,n+1}. \quad (3.5.9)$$

This is the main equation utilized in the simulation: the single-phase flow equation discretized by the BTCS method and linearized by the simple iteration of the transmissibility terms. This equation should be calculated for each grid block at each iteration. That would result in a linear system of equations for being solved at each iteration. The next chapter will show how the well will be modeled for being assembled in this equation before its solution.

# Chapter 4

## Well Representation

This chapter shows how the well has been modeled in the simulator developed in this project. According to Ertekin et al. (2001), wells are considered to be internal boundaries of the reservoir system, and therefore boundary conditions must be specified for the problem to be solved. One possible boundary condition is to utilize a specified flowing sandface pressure  $p_{wf}$ , characterizing a Dirichlet-type boundary condition. Another approach is by specifying a well flow rate, which characterizes a Neumann-type boundary condition. This simulator has been developed considering the well to be flow-rate specified. The well will be linked to the single-phase flow equation, Eq. 3.4.1, by the utilization of a source/sink term  $q_{sc}$ . This term is present in every cell of the model, but it is only non-zero if the grid block contains a producing or injecting well completion. The source/sink term  $q_{sc}$  can change with time, enabling the flow rate to be changed in the simulation input. Figure 4.1 shows an example of  $q_{sc}$  for a flow-rate specified well. The values of  $q_{sc}$  are negative in this graphic since the well is set to be producing, and negative values stand for production, while positive ones represent injection. Considering a steady-state flow near the wellbore, the radial form of Darcy's law is:

$$q = \frac{-2\pi\beta_c k h r_w}{\mu} \left. \frac{\partial p}{\partial r} \right|_{r=r_w}, \quad (4.0.1)$$

in which  $r_w$  is the well radius. Rearranging and considering a flow rate fixed in a specific value:

$$\left. \frac{\partial p}{\partial r} \right|_{r=r_w} = -\frac{\mu}{2\pi\beta_c k h r_w} q_{sp}. \quad (4.0.2)$$

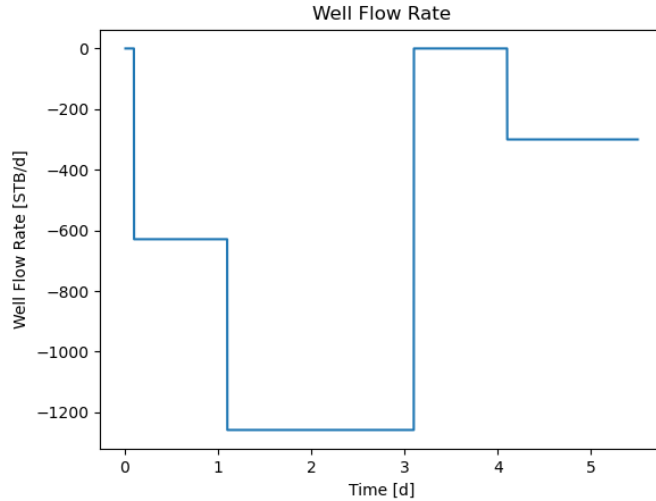


Figure 4.1: Example of a flow-rate specified well.

Since  $\mu$ ,  $\beta_c$ ,  $k$ ,  $h$  and  $r_w$  are specific for the problem, the pressure gradient should be constant:

$$\frac{\partial p}{\partial r} = c, \quad (4.0.3)$$

in which  $c$  represents a generic constant. Thus, it characterizes a Neumann-type boundary condition. Determining the well performance in a given perforated grid block requires knowing the grid block pressure,  $p_{i,j,k}$ , the flowing sandface pressure,  $p_{wf}$ , and the production rate,  $q_{sc}$ . Therefore, it is necessary to develop equations to relate the grid block unknowns to the unknowns added by the well model.

## 4.1 Inflow Performance Relationship

For a steady-state flow in the wellbore's vicinity, the radial form of Darcy's law is:

$$q = -\frac{2\pi\beta_c k_H h r}{\mu} \frac{\partial p}{\partial r}, \quad (4.1.1)$$

in which  $k_H$  is the radial permeability, equals to the geometrical mean of  $k_x$  and  $k_y$ . Rearranging and integrating it:

$$\int_{r_w}^r \frac{1}{r} \partial r = -\frac{2\pi\beta_c k_H h}{q\mu} \int_{p_{wf}}^p \partial p. \quad (4.1.2)$$

Thus:

$$p = p_{wf} - \frac{q\mu}{2\pi\beta_c k_H h} \ln\left(\frac{r}{r_w}\right). \quad (4.1.3)$$

In terms of flow rate:

$$q = -\frac{2\pi\beta_c k_H h}{\mu \log_e(r_e/r_w)} (p_e - p_{wf}), \quad (4.1.4)$$

where  $p_e$  is the reservoir external pressure, and  $r_e$  is the reservoir external radius. Considering the flow rate in the surface conditions:

$$q_{sc} = -\frac{2\pi\beta_c k_H h}{\mu B \ln(r_e/r_w)} (p_e - p_{wf}), \quad (4.1.5)$$

This is the inflow performance relationship (IPR) for an undamaged well under a steady-state flow. However, in reservoir engineering, the IPR is usually expressed in terms of the average reservoir pressure, instead of the external boundary pressure. According to Ertekin et al. (2001), for a cylindrical reservoir, its average pressure,  $\bar{p}$ , could be described as:

$$\bar{p} = \left[ \int_{r_w}^{r_e} 2\pi r h p dr \right] / \left[ \int_{r_w}^{r_e} 2\pi r h dr \right]. \quad (4.1.6)$$

Substituting Eq. 4.1.3 in Eq. 4.1.6:

$$\bar{p} = \frac{2}{(r_e^2 - r_w^2)} \int_{r_w}^{r_e} p r dr. \quad (4.1.7)$$

Developing the equation:

$$\bar{p} = \frac{2}{(r_e^2 - r_w^2)} \int_{r_w}^{r_e} \left[ p_{wf} - \frac{q\mu}{2\pi\beta_c k_H h} \log_e\left(\frac{r_e}{r_w}\right) \right] r dr. \quad (4.1.8)$$

Solving the integral in the right term:

$$\bar{p} = p_{wf} - \frac{q\mu}{2\pi\beta_c k_H h(r_e^2 - r_w^2)} \left[ r_e^2 \log_e \left( \frac{r_e}{r_w} \right) (r_e^2 - r_w^2) \right]. \quad (4.1.9)$$

When  $r_e \gg r_w$ , the term  $(r_e^2 - r_w^2)$  tends to  $r_e^2$ . Rearranging:

$$\bar{p} = p_{wf} - \frac{q\mu}{2\pi\beta_c k_H h} \left[ \log_e \left( \frac{r_e}{r_w} \right) \right] \quad (4.1.10)$$

In terms of flow rate:

$$q = \frac{-2\pi\beta_c k_H h}{\mu \left[ \log_e \left( \frac{r_e}{r_w} \right) \right]} (\bar{p} - p_{wf}), \quad (4.1.11)$$

In standard conditions:

$$q_{sc} = \frac{-2\pi\beta_c k_H h}{\mu B \left[ \log_e \left( \frac{r_e}{r_w} \right) \right]} (\bar{p} - p_{wf}), \quad (4.1.12)$$

The skin factor  $s$  is a dimensionless pressure drop utilized for representing damage (if positive) or a stimulation (if negative) in the wellbore. Including it in the equation:

$$q_{sc} = \frac{-2\pi\beta_c k_H h}{\mu B \left[ \log_e \left( \frac{r_e}{r_w} \right) + s \right]} (\bar{p} - p_{wf}), \quad (4.1.13)$$

This is the final form of the IPR equation for a well considering a steady-state flow in its boundaries. Utilizing the definition of the well's productivity index (PI),  $J_w$ :

$$J_w = \frac{2\pi\beta_c k_H h}{\mu B \left[ \log_e \left( \frac{r_e}{r_w} \right) + s \right]}, \quad (4.1.14)$$

thus, the IPR equation could be simplified as:

$$q_{sc} = -J_w (\bar{p} - p_{wf}), \quad (4.1.15)$$

The next subchapter shows a model for calculating  $r_e$  as the equivalent well radius  $r_{eq}$ . Assembling that definition into Eq. 4.1.14 will make it possible to calculate  $q_{sc}$  and utilize it as the sources/sinks terms in the single-phase flow equation, 3.4.1. However, this is only possible in rate-specified wells passing across a single perforated grid block. In wells with multiple perforated layers, it is necessary to decompose the total specified well flow rate into individual flow rates of each perforated grid block. This process will be shown in the last part of this chapter.

## 4.2 Peaceman Model

The simulator has been developed for considering a vertical well passing across the center of the grid blocks. The well grid block is not necessarily square, and the simulator considers an anisotropic reservoir in terms of petrophysical proprieties. Then, the  $r_e$  in the Eq. 4.1.14 will be approximated by the equivalent well radius  $r_{eq}$  in the Peaceman model for non-square grid blocks with anisotropic permeability. According to Ertekin et al. (2001), the

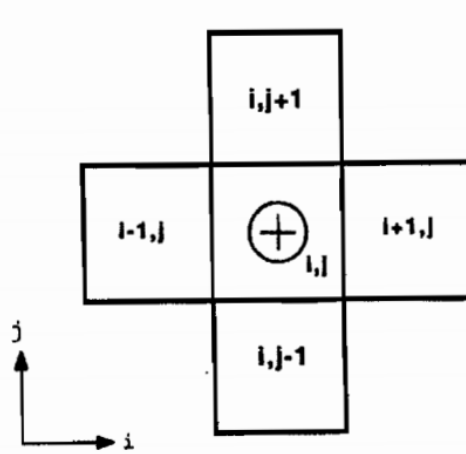


Figure 4.2: Vertical section of the wellbore and the grid blocks considered in its flow model. Source: Ertekin et al. (2001).

equivalent well radius,  $r_{eq}$ , in which the steady-state reservoir pressure is equal to the pressure in the well grid block,  $p_{i,j,k}$ , is:

$$r_{eq} = 0.28 \frac{\{[(k_y/k_x)^{1/2}(\Delta x)^2] + [(k_x/k_y)^{1/2}(\Delta y)^2]\}^{1/2}}{(k_y/k_x)^{1/4} + (k_x/k_y)^{1/4}} \quad (4.2.1)$$

This is the Peaceman model for non-square grid blocks with anisotropic permeability. This definition of  $r_{eq}$  can then be assembled into Eq. 4.1.14, making possible the calculation of the well productivity index,  $J_w$ .

### 4.3 Well Model for Multiple Perforated Layers

The Eqs. 4.1.3 and 4.2.1 alone can only represent a well with producing/injecting intervals inside a single grid block. For wells with more than one cell containing open completions, a different approach is required. Figure 4.3 illustrates a well passing across multiple layers. Each perforated cell can and probably

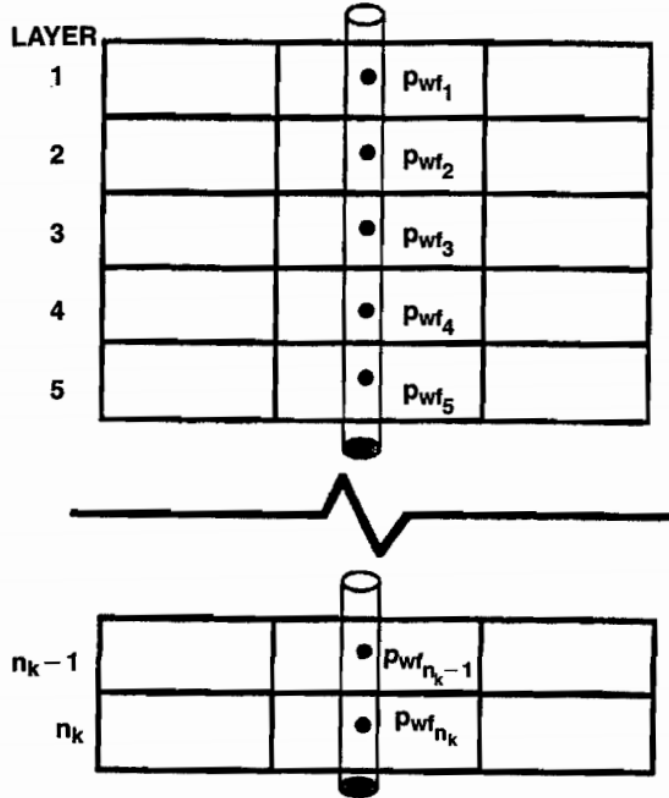


Figure 4.3: Wellbore with multiple layers. Source: Ertekin et al. (2001).

have different properties such as permeabilities,  $k_{H_k}$ , skin factor,  $s_k$ , radii,  $r_{w_k}$ , and, consequently, productivity indexes,  $J_{w_k}$ . Furthermore, each perforated layer can have different flowing sandface pressures,  $p_{wf_k}$ , and grid blocks pressures,  $p_k$ . In reservoir engineering, flow-rate specified wells usually are described by their total flow rate in surface conditions,  $q_{spsc}$ . That, however, is not the flow rate value utilized in the source/sink terms  $q_{sc}$  in the Eq. 3.4.1.  $q_{spsc}$  represents the flow rate of the entire well, while  $q_{sc}$  is only the individual flow rate of a given grid block region. Decomposing this total flow

rate,  $q_{spsc}$ , in the individual flow rates of each layer,  $q_{sc_k}$ , can not be done by just dividing it equally for each perforated grid block. Since each of the cells has different  $p_{i,j,k}$ ,  $p_{wf}$  and  $J_w$ , the  $q_{sc_k}$  are not necessarily equal fractions of  $q_{spsc}$ . Figures 4.4 and 4.5 help to visualize this idea. The first image shows an unrealistic well model in which each grid block in the wellbore region has the same source/sink term, while the second image shows a realistic model, in which the total flow rate  $q_{spsc}$  is decomposed in different individual flow rates  $q_{sc_k}$  for each grid block.

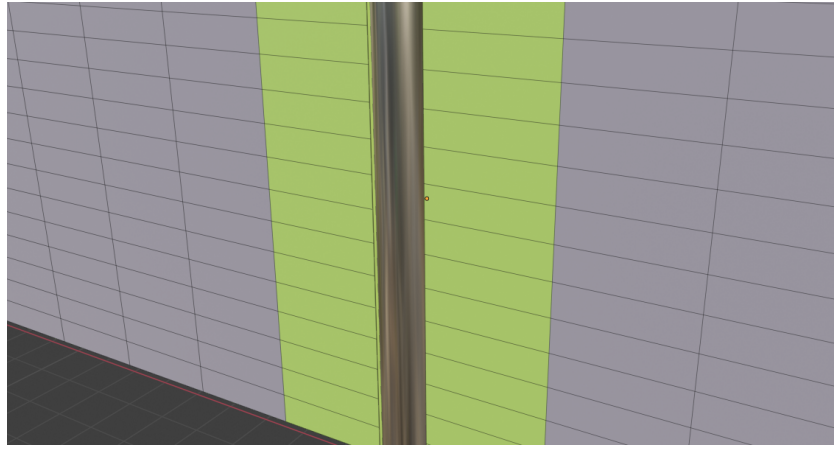


Figure 4.4: Example of well completions passing across multiple grid blocks. The color represents the source/sink term of each grid block in a given time step for a production scenario. This image represents an unrealistic scenario since each layer has the same value of individual flow rate.

The well model developed in this project approaches the multilayering by a method proposed by Ertekin et al. (2001). In a final analysis, the objective is to calculate the individual flow rates  $q_{sc_k}$  for all the cells in the well perforations domain. Then it would be possible to input them as the source/sink terms in the single-phase flow equation, 3.4.1. This needs to be done for each time step, since  $q_{sc_k}$  depends on some proprieties that can change with time (e.g.  $\mu$ ,  $B$ ,  $\gamma_{wb}$ ,  $\bar{p}$  and  $q_{spsc}$ ). This process will result in an iteration, since the specific weight inside the wellbore  $\gamma_{wb}$  and the flowing sandface pressure  $p_{wf}$  are unknowns and mutually dependent. This process will be described below.

The IPR equation, Eq. 4.1.13, for a given perforated grid block in a layer  $k$ , is:

$$q_{sc_k} = \frac{-2\pi\beta_ck_{Hk}h_k}{\mu_k B_k \left[ \log_e \left( \frac{r_{eq_k}}{r_w} \right) + s_k \right]} (\bar{p}_k - p_{wf_k}), \quad (4.3.1)$$

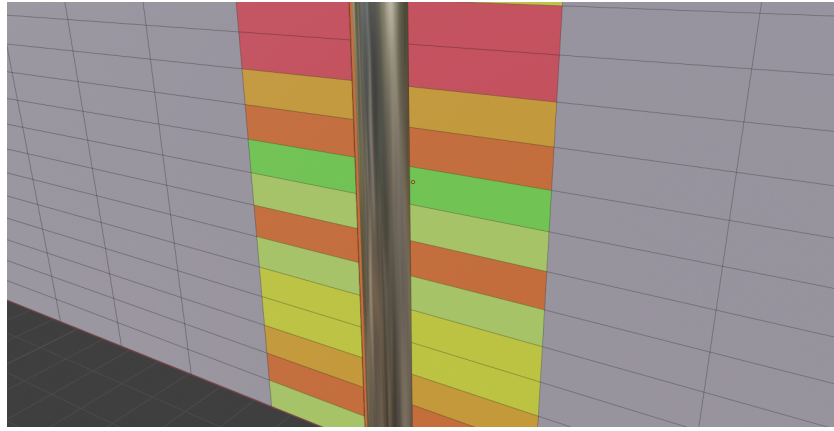


Figure 4.5: Example of well completions passing across multiple grid blocks. The color represents the source/sink term of each grid block in a given time step for a production scenario. This image depicts a realistic scenario in which each layer has a different value of individual flow rate.

which could be rewritten in terms of the PI as:

$$q_{sc_k} = -J_{w_k} (p_k - p_{wf_k}), \quad (4.3.2)$$

in which:

$$J_{w_k} = \frac{2\pi\beta_c k_{H_k} h_k}{\mu_k B_k \left[ \log_e \left( \frac{r_{eq_k}}{r_w} \right) + s_k \right]}. \quad (4.3.3)$$

The total flow rate of the well,  $q_{spsc}$ , is the sum of all the individual flow rates of the perforated layers,  $q_{sc_k}$ . Thus:

$$q_{spsc} = - \sum_k J_{w_k} (p_k - p_{wf_k}), \quad (4.3.4)$$

in which  $k \in \psi_w$ , where  $\psi_w$  is the set of all the perforated grid blocks. Similarly to the variables in the flow equation, it is necessary to determine a time level in which the well flow rates will be evaluated. The simple iteration method has been utilized, where the IPR parameters are evaluated at the time level  $n + 1$ , but at the previous iteration level,  $\nu$ .

For determining the pressure distribution inside the wellbore, the conventional approach in reservoir simulation is to neglect the friction losses inside the tubing and downhole equipment. Although this is not the most realistic approach, integrating those effects in a reservoir simulator would result in a system with high complexity, requiring an unfeasible amount of computational power. There are simulators specially made for analyzing the flow

inside the well and pipeline systems, but those are not commonly integrated to reservoir simulators. After neglecting the friction losses inside the wellbore, the flowing sandface pressures for each layer,  $p_{wf_k}$ , can be obtained by:

$$p_{wf_k} = p_{wf_{ref}} + \int_{H_{ref}}^{H_k} \gamma_{wb} dH, \quad (4.3.5)$$

where  $p_{wf_{ref}}$  is the flowing sandface pressure of a reference layer, and  $\gamma_{wb}$  is the specific weight inside the wellbore in the perforated grid blocks. For the simulator developed in this project, the selected reference layer has been the topmost perforated grid block. Ertekin et al. (2001) recommends the following approximation to this integral:

$$p_{wf_k} = p_{wf_{ref}} + \bar{\gamma}_{wb}(H_k - H_{ref}). \quad (4.3.6)$$

in which  $H_{ref}$  is the depth of the reference layer,  $H_k$  is the depth of a given layer  $k$  and  $\bar{\gamma}_{wb}$  is the average specific weight in the well for the perforated region. The average flowing sandface pressure,  $\bar{p}_{wf}$ , could be described as the arithmetic average between the lowest and the highest pressures inside the perforated regions of the wellbore, those are  $p_{wf_{ref}}$  and  $p_{wf_n}$ :

$$\bar{p}_{wf} = \frac{p_{wf_{ref}} + p_{wf_n}}{2}, \quad (4.3.7)$$

where  $n$  is the index of the lowermost perforated cell. For allocating the quotes of the total well flow rate in each perforated layer, the following relationship is valid:

$$q_{sc_k} = \frac{q_{sc_k}}{q_{spsc}} q_{spsc}, \quad (4.3.8)$$

Applying the IPR equation, Eq 4.3.2:

$$q_{sc_k} = \frac{J_{w_k} (p_k - p_{wf_k})}{\sum_m J_{w_m} (p_m - p_{wf_m})} q_{spsc}, \quad (4.3.9)$$

where  $m$  and  $k \in \psi_w$ . Ertekin et al. (2001) describes it as the potential method for multilayering. Substituting the Eq. 4.3.6 in the IPR equation for the total flow rate in the well, Eq. 4.3.2:

$$q_{spsc} = \sum_k J_{w_k} \left\{ p_k - [p_{wf_{ref}} + \bar{\gamma}_{wb} (H_k - H_{ref})] \right\}, \quad (4.3.10)$$

Rearranging:

$$q_{spsc} = \sum_k J_{w_k} [p_k - \bar{\gamma}_{wb} (H_k - H_{ref})] + \sum_k J_{w_k} p_{wf_{ref}}, \quad (4.3.11)$$

After further rearrangements, in terms of  $p_{wf_{ref}}$ :

$$p_{wf_{ref}} = \frac{\sum_k \{J_{w_k} [p_k - \bar{\gamma}_{wb}(H_k - H_{ref})] + q_{spsc}\}}{\sum_k J_{w_k}}, \quad (4.3.12)$$

Since both  $\bar{\gamma}_{wb}$  and  $p_{wf_k}$  are unknowns and mutually dependent, it is necessary to perform an iterative process. Table 4.1 shows the iterative approach that has been utilized:

Table 4.1: Algorithm for modeling a well with multiple perforated grid blocks.

- 
- 1) At the initial conditions,  $p_{wf_k}$  are set to be equal to  $p_k$ .
  - 2)  $\bar{p}_{wf}$  is calculated by utilizing the Eq. 4.3.7.
  - 3)  $\bar{\gamma}_{wb}$  is interpolated in the fluid table for  $\bar{p}_{wf}$ .
  - 4)  $J_{w_k}$  is calculated for each perforated cell with Eq. 4.3.3.
  - 5)  $p_{wf_{ref}}$  is obtained by the Eq. 4.3.12.
  - 6)  $p_{wf_k}$  is calculated with Eq. 4.3.6 for each perforated grid block.
  - 7)  $\bar{p}_{wf}$  is again calculated using the Eq. 4.3.7.
  - 8)  $\bar{\gamma}_{wb}^{new}$  is interpolated for the new value of  $\bar{p}_{wf}$ .
  - 9) If  $|\bar{\gamma}_{wb}^{new} - \bar{\gamma}_{wb}| > \epsilon$ ,  $\bar{\gamma}_{wb} = \bar{\gamma}_{wb}^{new}$  and return to 4). Otherwise, go to 10).
  - 10) Finally,  $q_{sc_k}$  is calculated with Eq. 4.3.9 for each perforated cell.
- 

After performing this process, the individual well flow rates  $q_{sc_k}$  are finally obtained. Then it is possible to utilize those values in the single-phase flow equation 3.4.1. Note that this process has to be done for each time step, since, as shown above,  $q_{sc_k}$  depends on time-dependent properties.

# Chapter 5

## Solution

The previous chapters have shown how the single-phase flow equation has been defined, discretized, simplified, linearized, and linked with the well model. Then it is possible to initialize the simulation and advance it in time. This chapter is composed of two sections, the equilibration process and the advancement in time. The first shows how the pressure distribution in the reservoir will be calculated for time zero. The second shows how the pressure at the next time step will be calculated, thus advancing the simulation in time. Finally, the last section shows how the simulator has been validated by comparing its results with reliable data.

## 5.1 Equilibration Process

At the beginning of the simulation, the initial pressures at each grid block  $p_{i,j,k}^{n=0}$  are usually unknown. Thus, it is necessary to calculate them before advancing in time. Typically, the user of a reservoir simulator has to input one or more value of pressures  $P^0$  at reference depths  $Z^0$ , in what is called an equilibration table. Then the simulator can compute the initial pressure distribution in the entire reservoir by applying hydrostatics. This step is known as the equilibration process and will be described in this section. Assuming a hydrostatic equilibrium at the time zero,  $\nabla\Phi = 0$ , Eq. 2.2.2 can be rewritten as:

$$\nabla\Phi = \nabla p - \gamma\nabla Z = 0. \quad (5.1.1)$$

Thus:

$$P^0 - p_{i,j,k} - \gamma_{i,j,k}(Z^0 - Z_{i,j,k}) = 0, \quad (5.1.2)$$

which can be rewritten as:

$$p_{i,j,k} = P^0 + \gamma_{i,j,k}(Z_{i,j,k} - Z^0), \quad (5.1.3)$$

Since the scenario considers a compressible fluid, its specific weight  $\gamma$  can change with pressure. Thus, it would be necessary to calculate both the pressure and the specific weight. Since they are mutually dependent unknowns, it is necessary to perform an iteration. Utilizing an index  $\nu$  for the iteration level, the specific weight  $\gamma$  will be evaluated in level  $\nu$  and the pressure  $p_{i,j,k}$  will be evaluated in the level  $\nu + 1$ :

$$p_{i,j,k}^{(\nu+1)} = P^0 + \gamma_{i,j,k}^{(\nu)}(Z_{i,j,k} - Z^0). \quad (5.1.4)$$

Figure 5.1 shows this iterative process for a grid block  $i, j, k$ .  $\epsilon$  is the tolerance of the iteration. It is set to be equal to  $10^{-8}$  for all the simulations in this project. The equilibration process consists in applying this process for every grid block in the model. After that, the pressure initialization is done, and it is then possible to advance the simulation in time.

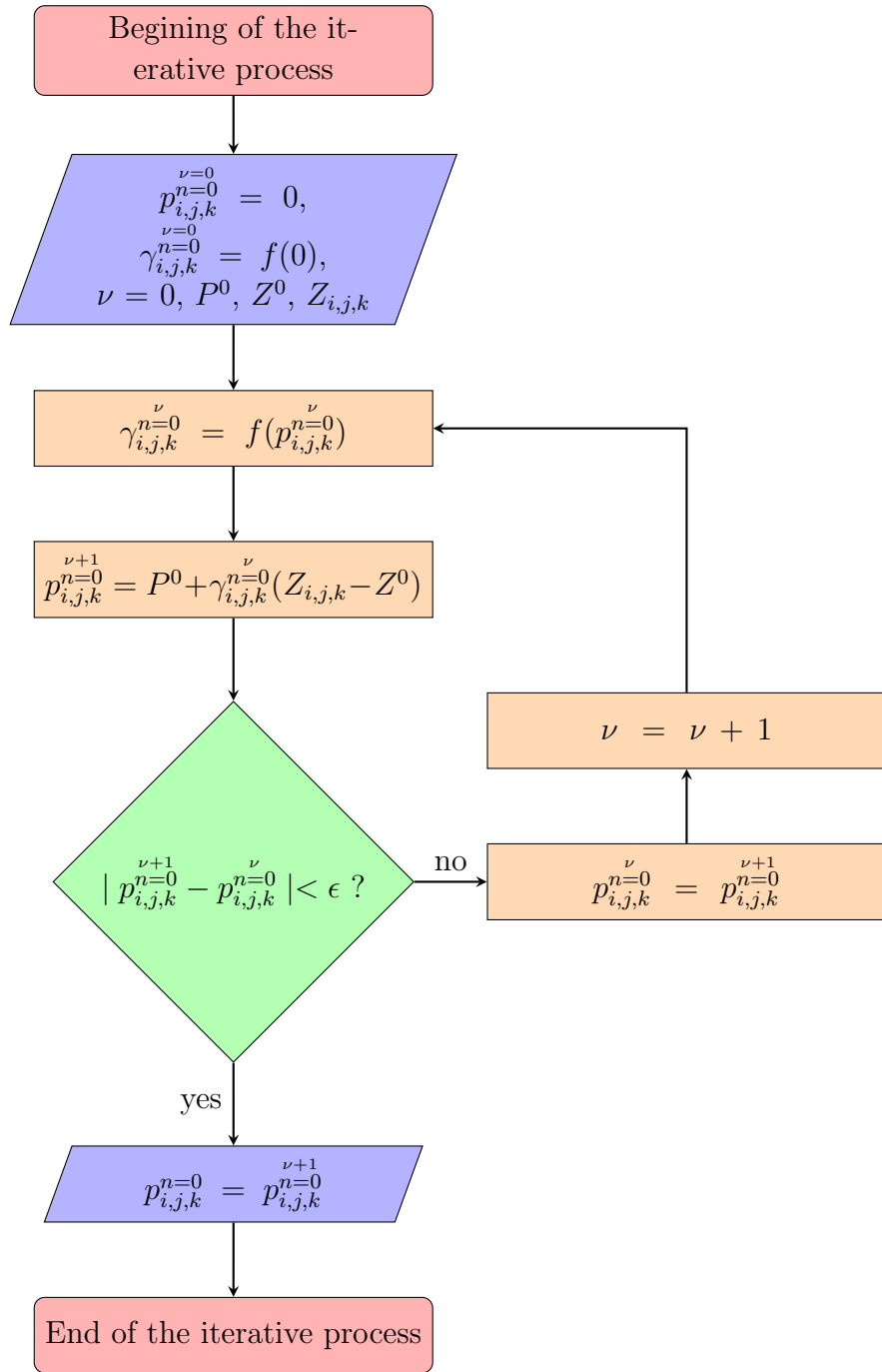


Figure 5.1: Iteration in the equilibration process.

## 5.2 Advancing in Time

The chapter 3 presents the discretized and linearized form of the single-phase flow equation, Eq. 3.5.9. After applying this equation to every grid block in the model, a linear system of equations is obtained. The Appendix A shows how such a system is generated for a simple example of a tridimensional grid. This section shows how to utilize this linear system of equations to calculate the pressure at a new time step, hence, advancing the simulation in time.

Developing a linear algebra solver is not the focus of this project. Thus, an external, open-source library has been utilized for solving the linear system of equations. This library is the UMFPACK, which stands for Unsymmetric, Multifrontal Sparse LU Factorization Package. It is a package that allows the solution of sparse linear systems by the method of LU factorization. Appendix B shows how the linear system of equations has been represented in a compressed format (CSC) for enabling its solution with UMFPACK.

After the equilibration process has been finished, as described in the previous section, the initial pressure distribution in the reservoir  $p_{i,j,k}^{n=0}$  is obtained and then it is possible to calculate  $p_{i,j,k}^{n+1}$ . Figure 5.2 shows the algorithm for advancing the simulation in time, based on the Eq. 3.5.9. Its convergence condition is that the absolute value of the difference between the norms of the pressures at the iteration levels of  $\nu + 1$  and  $\nu$  should be inferior to the tolerance  $\epsilon$ , defined as  $1 \times 10^{-8}$  for the models run in this project.

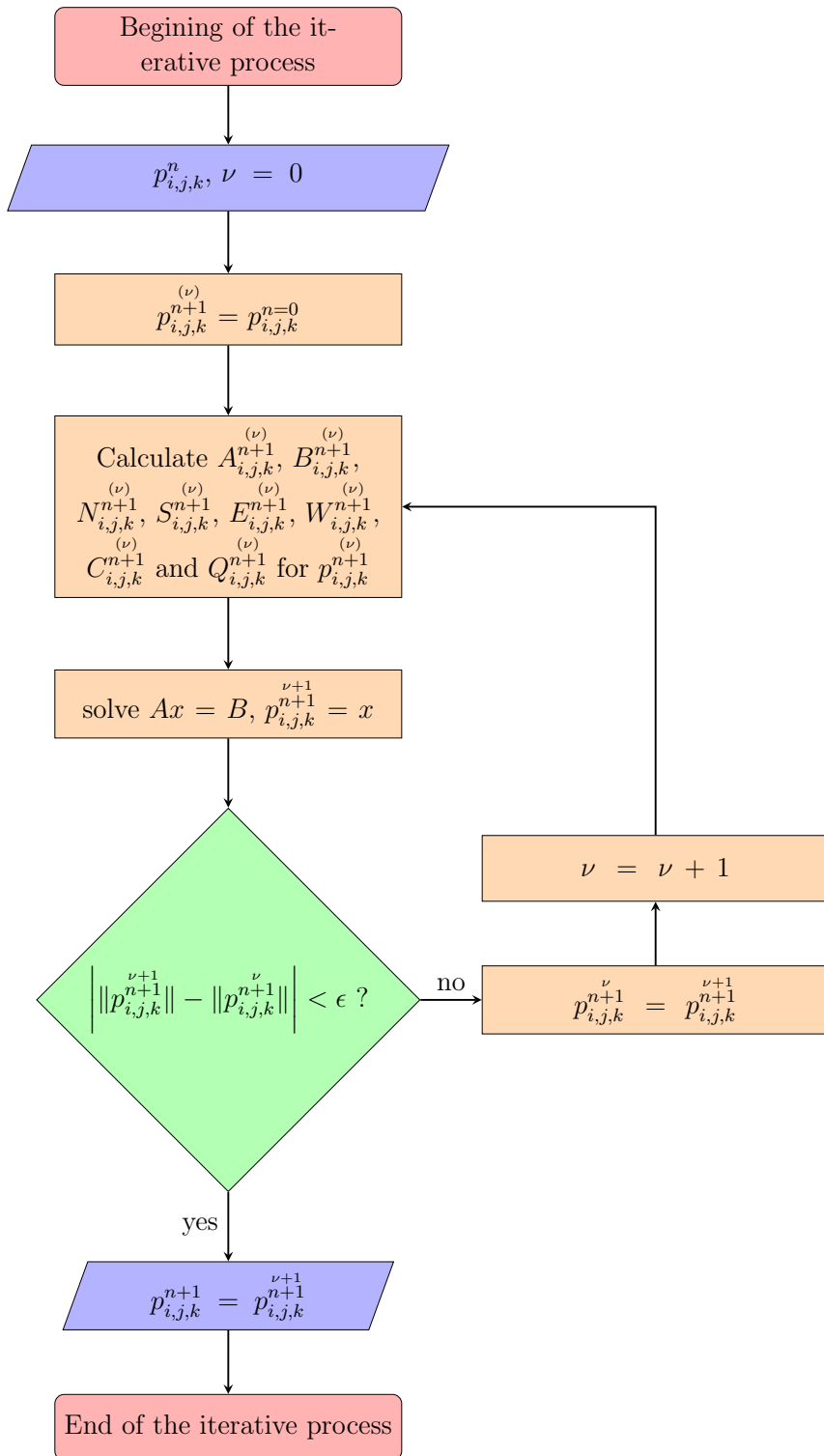


Figure 5.2: Iteration for calculating the pressure distribution after a time step.

## 5.3 Validation

A model should provide an accurate representation of a real system. Thus, an essential part of developing a reservoir simulation model is to ensure accuracy by validating its simulation results by comparing them with reliable data. This validation has been done in this project by comparing the CSPF (a possible name for this simulator, which stands for Compressible, Single-Phase Flow simulator) simulation results with the ones generated by an industry-standard simulator for the same models.

Two models have been utilized for this validation. The first is a buildup/drawdown well test scenario with homogeneous porosity and permeabilities. The second is a similar scenario, but the only difference is that the porosities and permeabilities are heterogeneous, generated by utilizing normal and log-normal distributions, respectively. Table 5.1 shows the parameters utilized in the first validation model:

Table 5.1: Parameters of the homogeneous scenario for the validation.

Parameter	Value (if applicable)
Number of grid blocks in the $x$ direction	15
Number of grid blocks in the $y$ direction	15
Number of grid blocks in the $z$ direction	10
Boundary conditions	Sealed reservoir
Well	Vertical well in the center of the reservoir
Completions	From the top to the bottom of the reservoir
Length of the grid blocks in the $x$ direction	164.042 ft
Length of the grid blocks in the $y$ direction	164.042 ft
Length of the grid blocks in the $z$ direction	16.4042 ft
Average porosity	10%
Average horizontal permeability	200 mD
Average vertical permeability	20 mD
Formation compressibility	$1.31 \times 10^{-4} \text{ psi}^{-1}$
Fluid compressibility	$1.41 \times 10^{-5} \text{ psi}^{-1}$
Depth of the topmost layer	10,498.69 ft
Reference depth for the initial pressure	10,498.69 ft
Initial pressure at the reference depth	3,916.01 psi
Well radius	6 in
Skin factor	-0.5

The fluid utilized in both models has its properties described in Figure 5.3. In the single-phase flow equation, the FVF, viscosity, and specific weight are obtained by applying a linear interpolation in these data. The fluid bubble point pressure is 3296.27 psi. This specific fluid model has been chosen since the pressure in the reservoir never reaches a value lower than its bubble point pressure and, therefore, would avoid a scenario of multiphase flow inferred by dissociated gas. The simulator developed in this project can not represent a situation of multiphase flow and would give unrealistic results.

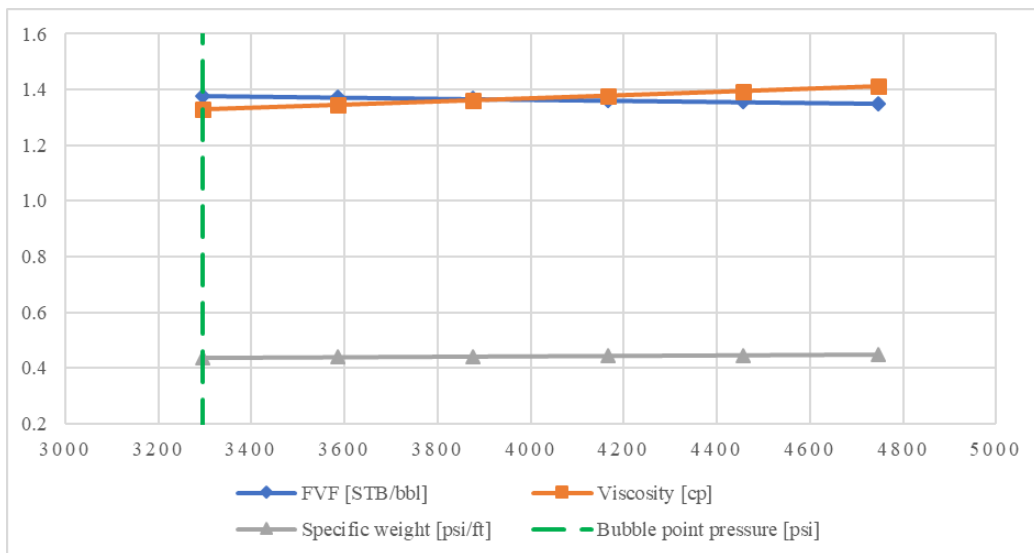


Figure 5.3: Fluid properties for the simulation.

The well has been initially set to be closed. At the time of 0.1 days, the well began producing at the flow rate of 2515.92 bbl/d and ceased its production at the time 1.1 days. Thus, a drawdown/buildup test has been simulated. Figure 5.4 illustrates these flow rate changes.

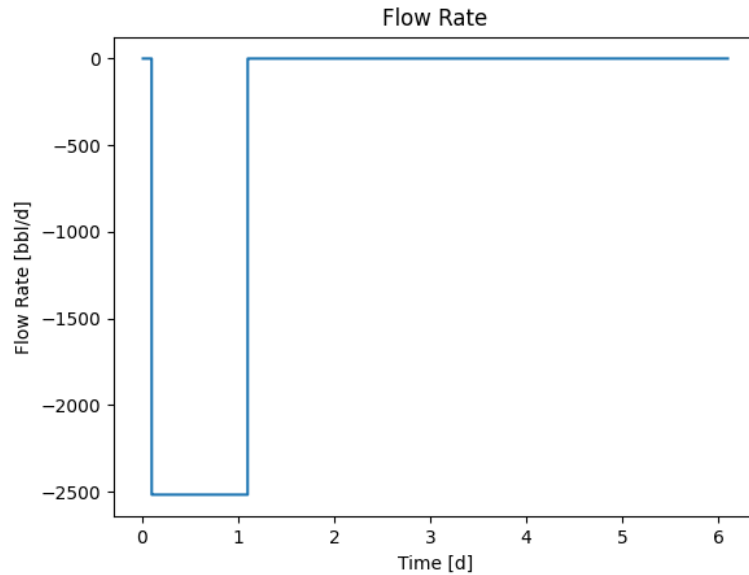


Figure 5.4: Well flow rate in the simulation. Negative values indicate production.

Figure 5.5 shows the bottom hole pressure for this test, both for the results from CSPF and IMEX.

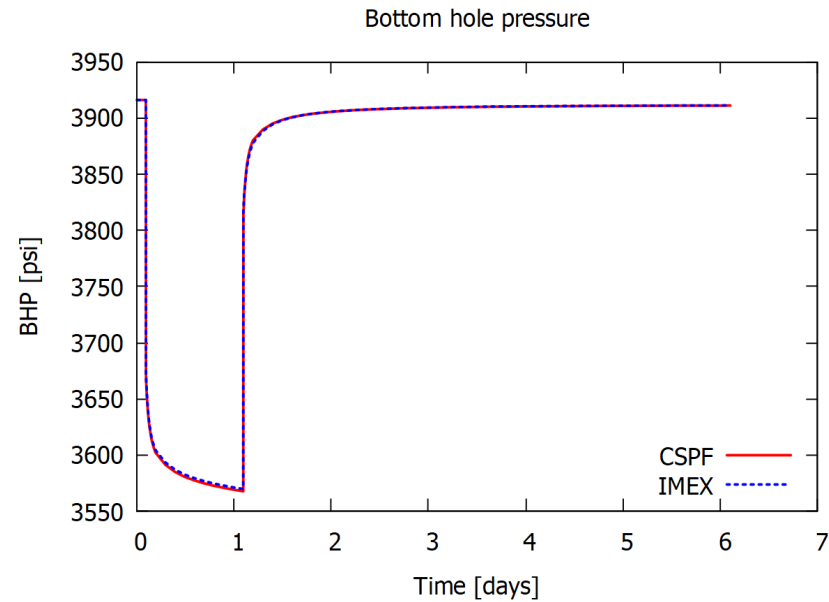


Figure 5.5: Comparison between the CSPF and IMEX for a drawdown/buildup well test in a homogeneous reservoir.

Between 0 and 0.1 days, the well is closed, therefore its bottom hole pressure does not change. When the production starts, the BHP gets a steep decline until the production ceases. Then, the pressure rises again, stabilizing itself with asymptotic behavior. The difference between the initial stable BHP and the value stabilized after the test is proportional to the amount of oil produced in the reservoir because the production of oil will cause a depletion in the reservoir. One could see that the results from CSPF and IMEX are very close. A similar simulation has been done for the heterogeneous scenario, its results are shown in Figure 5.6.

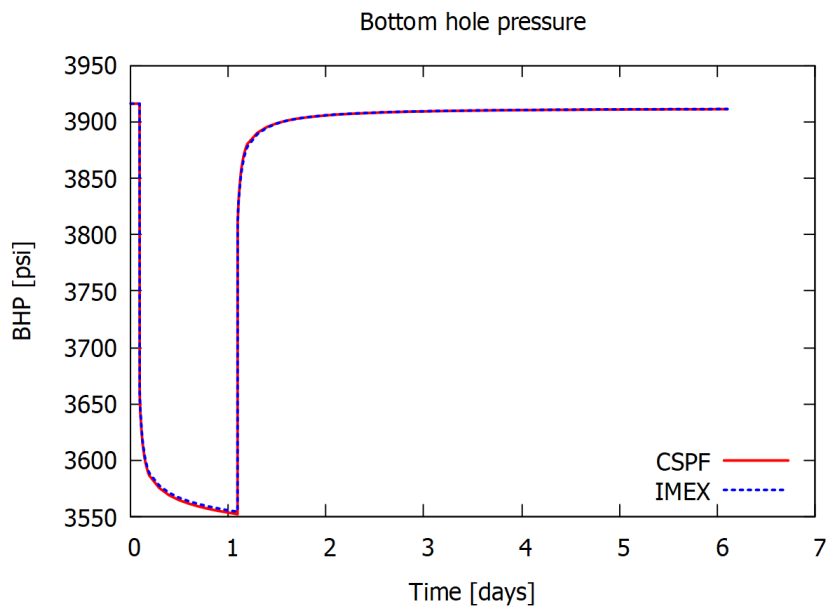


Figure 5.6: Comparison between the CSPF and IMEX for a drawdown/buildup well test in a heterogeneous and anisotropic reservoir.

Looking at the results for the heterogeneous case in Figure 5.6, one could see a modest change in comparison to the homogeneous results shown by Figure 5.5. One difference is the minimum BHP, which is slightly lower in the second case. Again, the CSPF results are very similar to IMEX's.

The difference between IMEX and CSPF for both scenarios has been plotted and displayed in Figure 5.7. One explanation for these disparities could be the rounding dissimilarities between IMEX and CSPF, but overall the results are very similar. When juxtaposing the Figure 5.7 with the Figures 5.5 and 5.6, one could note that the relative differences are higher when the BHP variation is steeper.

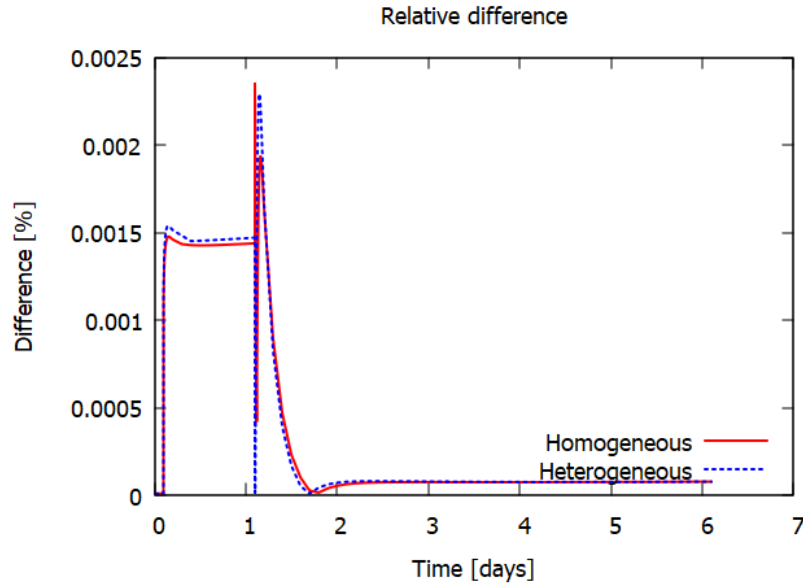


Figure 5.7: Relative differences between CSPF and IMEX for the heterogeneous and homogeneous cases.

In conclusion, the results above show high accuracy in the simulator developed in this project compared to industry-standard software.

# Chapter 6

## Fundamentals of Upscaling

According to Lie (2015), upscaling or homogenization is defined as the process of propagating properties from a model with a high spatial resolution to one with a lower spatial resolution. In the case of reservoir simulation, upscaling consists of representing heterogeneous properties that variate inside a coarse grid block by single, effective values for the grid block. Therefore, there are two models which should be considered: the coarse and the fine-grid model. For the case considered in this study, the boundaries of the coarse grid blocks will always coincide with the limit of the fine grid blocks, which means that there will be an integer number of fine grid blocks inside each of the coarse ones. Figure 6.1 illustrates the upscaling process and represents how this coarse grid will be defined.

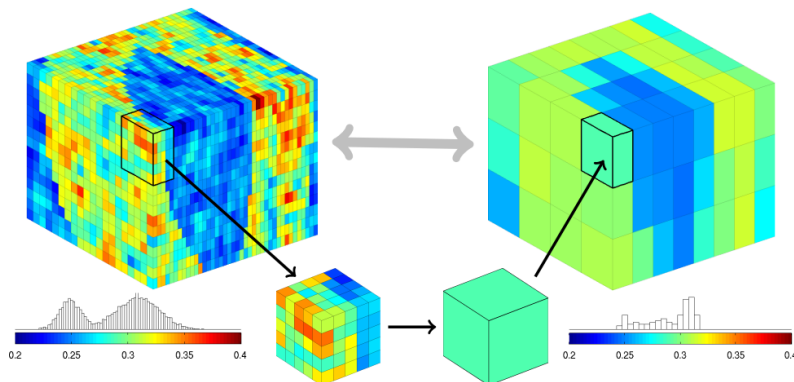


Figure 6.1: Illustration of porosity upscaling from a fine to a coarse grid.  
Source: Lie (2015).

Lie (2015) defines two kinds of properties: additive and non-additive. Additive properties could be upscaled by utilizing a single non-additive av-

eraging, while non-additive could only be averaged analytically in individual cases, and the conventional approach is to approximate it in numerical methods. Examples of additive properties include porosity, net-to-gross, saturations, and concentrations, while non-additive includes absolute permeability, relative permeability, and transmissibilities. This project is limited to the upscaling of porosity and permeability, the first being an additive and the second, non-additive property.

## 6.1 Upscaling Additive Properties

According to Lie (2015), porosity is the simplest example of additive property and could be averaged by a simple non-additive averaging. Considering  $\Omega$  the region that will be upscaled, the average porosity or the porosity of the coarse grid,  $\phi^c$  will be:

$$\phi^c = \frac{1}{\Omega} \int_{\Omega} \phi(x, y, z) dV. \quad (6.1.1)$$

The  $c$  index will be consistently utilized to represent an upscaled value, which is the effective, representative value for the coarse grid blocks. Other additive properties can be upscaled in a similar form, except that their bulk average should be weighted with porosity. Considering  $a$  an additive property other than porosity:

$$a^c = \left[ \int_{\Omega} \phi(x, y, z) dV \right]^{-1} \int_{\Omega} a(x, y, z) \phi(x, y, z) dV. \quad (6.1.2)$$

## 6.2 Upscaling Absolute Permeability

Lie (2015) divides upscaling into two distinct segments: single-phase and multiphase. The property scaled up in single-phase upscaling is the absolute permeability, while in multiphase upscaling it is the relative permeability. Since this project does not comprise a multiphase flow scenario, the only permeability to be averaged will be the absolute one. Since it is a non-additive property, it is not possible to utilize a simple volumetric averaging. Lie (2015) explains the process of absolute permeability upscaling by utilizing the flow described by the Poisson equation:

$$\nabla \cdot K \nabla p = 0. \quad (6.2.1)$$

where  $K$  is the permeability tensor. The majority of upscaling techniques consists in determining an effective permeability tensor  $K^c$  that reproduces in the coarse grid blocks the flow rate inside it, in the fine-scale region. Mathematically:

$$\int_{\Omega} K(x, y, z) \nabla p dV = K^c \int_{\Omega} \nabla p dV. \quad (6.2.2)$$

Eq. 6.2.2 states that the net flow rate  $v_{\Omega}$  through  $\Omega$  is associated with the average pressure gradient  $\nabla_{\Omega} p$  in  $\Omega$  by the upscaled Darcy's law, which its tensorial form is:

$$v_{\Omega} = -K^c \nabla_{\Omega} p. \quad (6.2.3)$$

Lie (2015) states that the permeability tensor is not uniquely defined by Eq. 6.2.2 for a pressure field  $p$ , in other words, there is not a unique  $K^c$  tensor that accounts for any  $p$ . Thus,  $K^c$  depends on the flow through  $\Omega$ , determined by the boundary conditions in the fine-scale region. Lie (2015) also states that if those boundary conditions are precisely known, it is possible to compute the true effective permeability. However, one could not know what those boundary conditions exactly are unless the problem is already solved. Therefore, what is generally done is performing a reasonable and representative guess giving reasonably accurate results for several flow scenarios.

### 6.2.1 Flow-based Methods

Lie (2015) states that the permeability tensor is not uniquely defined by Eq. 6.2.2 for a pressure field  $p$ . In other words, there is not a unique  $K^c$  tensor that accounts for any  $p$ . According to Nunna et al. (2015), the industry has

been focused on developing upscaling algorithms based on permanent, incompressible flow. This project approaches upscaling by utilizing the averaging techniques, which, besides being simple, are foreseen to give a more accurate representation than the flow-based methods.

### 6.2.2 Averaging Methods

According to Lie (2015), averaging methods for upscaling consist of utilizing analytical averaging, most of the times following the power average formula:

$$K^c = A_p(K) = \left( \frac{1}{|\Omega|} \int_{\Omega} K(x, y, z)^p dV \right)^{\frac{1}{p}}, \quad (6.2.4)$$

where  $p = 1$  and  $p = -1$  respectively refer to the arithmetic and harmonic means, and  $p \rightarrow 0$  corresponds to the geometric mean. According to Wiener (1912), for a statistic homogeneous medium, the correct upscaled permeability is bounded above by the arithmetic mean, and below by the harmonic mean. For a steady-state the Eq. 6.2.3 is:

$$\frac{\partial}{\partial t} v_{\Omega} = 0, \quad (6.2.5)$$

$$\frac{\partial}{\partial t} (-K^c \nabla_{\Omega} p) = 0. \quad (6.2.6)$$

Considering a permanent permeability tensor:

$$-K \frac{\partial}{\partial t} (^c \nabla_{\Omega} p) = 0. \quad (6.2.7)$$

Considering a system of layers with homogeneous permeability values in perpendicular to the pressure gradient, as illustrated in Figure 6.2.8: It is possible to write:

$$K \int_0^L \frac{dp(x)}{dx} dx = K^c(p_L - p_0). \quad (6.2.8)$$

Moreover, from Eq. 6.2.5:

$$\int_0^L K(x) \frac{dp(x)}{dx} dx = \int_0^L v dx = -Lv. \quad (6.2.9)$$

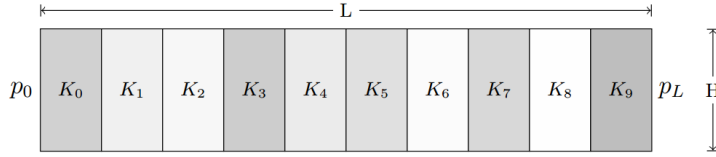


Figure 6.2: Illustration of a perfectly stratified medium with layers perpendicular to the pressure gradient. According to Lie (2015), in this setting, harmonic is the appropriate averaging for upscaling permeability. Source: Lie (2015).

Applying Eqs. 6.2.8 and 6.2.9 in Eq. 6.2.2:

$$v = -K^c \frac{(p_L - p^0)}{L}. \quad (6.2.10)$$

From Darcy's law, Eq. 6.2.7:

$$\int_0^L \frac{dp}{dx}(x) dx = - \int_0^L \frac{v}{K(x)} dx, \quad (6.2.11)$$

$$\int_0^L \frac{dp}{dx}(x) dx = K^c \frac{(p_L - p^0)}{L} \int_0^L \frac{1}{K(x)} dx, \quad (6.2.12)$$

$$\int_0^L \frac{dp}{dx}(x) dx = K^c \left( \int_0^L p(x) dx \right) \frac{1}{L} \int_0^L \frac{1}{K(x)} dx, \quad (6.2.13)$$

Hence:

$$K^c = A_{-1}(K) = \left( \frac{1}{L} \int_0^L \frac{1}{K(x)} dx \right)^{-1}, \quad (6.2.14)$$

which shows that harmonic is the correct way to upscale permeability in such a scenario. On the other hand, for a system of homogeneous permeabilities values parallel to the pressure gradient, according to Figure 6.2. Since the permeability, in this case, is constant along the direction  $x$ , the pressure could be described as:

$$p(x, y) = p_0 + \frac{x(p_L - p_0)}{L}. \quad (6.2.15)$$

Moreover, it is possible to write:

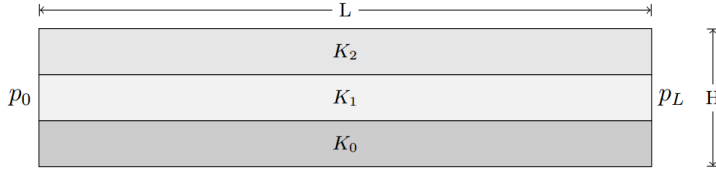


Figure 6.3: Illustration of a perfectly stratified medium with layers parallel to the pressure gradient. According to Lie (2015), in this setting, arithmetic is the appropriate averaging for upscaling permeability. Source: Lie (2015).

$$K^c \int_0^H \int_0^L \frac{\partial p(x, y)}{\partial x} dx dy = K^c H(p_L - p_0) \quad (6.2.16)$$

and

$$\int_0^H \int_0^L K(x, y) \frac{\partial p(x, y)}{\partial x} dx dy = \frac{p_L - p_0}{L} \int_0^H \int_0^L K(x, y) dx dy. \quad (6.2.17)$$

Applying Eqs. 6.2.16 and 6.2.17 in Eq. 6.2.2:

$$K^c = A_1(K) = \frac{1}{HL} \int_0^H \int_0^L K(x, y) dx dy, \quad (6.2.18)$$

which is arithmetic averaging. By those two methods, it is possible to create a permeability tensor for scenarios like the described in the Figures 6.2.8 and 6.3:

$$K^c = \begin{bmatrix} A_{-1}^x(K) & 0 \\ 0 & A_1^x(K) \end{bmatrix} \quad (6.2.19)$$

and

$$K^c = \begin{bmatrix} A_1^y(K) & 0 \\ 0 & A_{-1}^y(K) \end{bmatrix} \quad (6.2.20)$$

where the superscripts x and y in the averaging operator  $A$  means that it is only applied in that direction. For modeling flow in more directions and also for less idealized heterogeneous regions, it is possible to combine those two methods through the tensor:

$$K^c = \begin{bmatrix} A_1^{yz}(A_{-1}^x(K)) & 0 & 0 \\ 0 & A_1^{xz}(A_{-1}^y(K)) & 0 \\ 0 & 0 & A_1^{xy}(A_{-1}^z(K)) \end{bmatrix} \quad (6.2.21)$$

This method is called the harmonic-arithmetic averaging and, according to Lie (2015), might give a fair upscaling in layered reservoirs when the main direction of flow is along with the layers. This method provides a tight lower bound on permeability, while its inverse, the arithmetic-harmonic averaging, provides a tight upper bound.

## Chapter 7

# Fundamentals of Well Testing

This chapter will give a brief description of well testing and the diagnostic tools utilized in this project.

Well testing is commonly utilized in the industry for obtaining information about the reservoir and the well. Those data are then included in reservoir models for predicting the well and field responses to different development scenarios. According to Bourdet (2002), the information obtained in a well test include:

- Average horizontal and vertical permeabilities in an investigated region.
- The presence or absence of heterogeneities in the reservoir, such as natural fractures, layering, and variation in the reservoir characteristics.
- The presence or absence of boundaries close to the well, their distance, and shape.
- Initial pressure in an investigated region.
- Average pressure in an investigated region.
- Well productivity index, or PI.
- Well skin factor (a dimensionless pressure drop due to damage or stimulation in the interface between the well and the reservoir).
- Well geometry.

Different than the static data obtained with geological and logging methods, a well test provides the reservoir properties in dynamic conditions. Workflows of integrated reservoir characterization commonly utilize both kinds of data to build a robust model.

In a well testing operation, a change in the flow rate originates a transient in the bottom hole pressure. This transient is then monitored in a usually short time period (compared to the field life cycle). Commonly, the pressure is recorded down-hole with a tool, while the flow rate is controlled in the surface. In the initial conditions, the bottom hole pressure, BHP, is constant. After opening the well, this pressure decreases while the well produces. This drawdown pressure drop,  $\Delta p_{Dd}$ , is described as:

$$\Delta p_{Dd} = p_i - p(t). \quad (7.0.1)$$

When the well ceases its production, the build-up pressure change,  $\Delta p_{BU}$  is:

$$\Delta p_{BU} = p(t) - p(t = 0), \quad (7.0.2)$$

where  $p(t = 0)$  is the pressure in the last time recorded with the well flowing. Figure 7.1 shows a typical sequence of a drawdown/build-up well test.

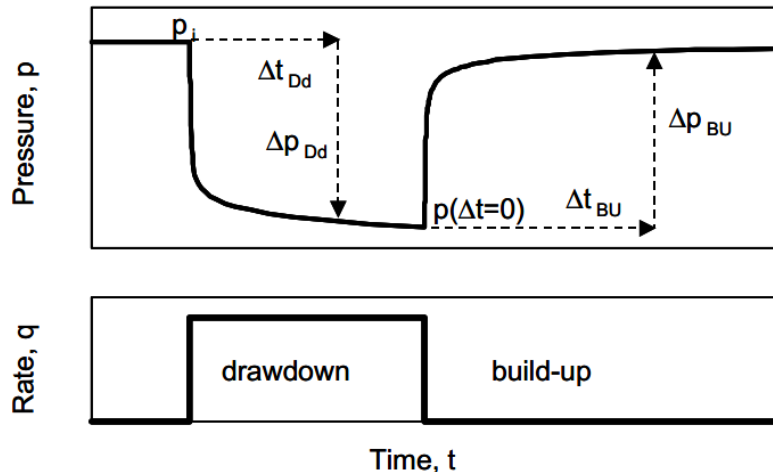


Figure 7.1: Typical representation of a bottom hole pressure behavior in a drawdown/build-up test. Source: Bourdet (2002).

Besides the previous plots shown above, a log-log plot is also utilized in the post-processing of data. That helps to identify patterns that could not be seen initially. Bourdet (2002) shows an example of such analysis in the diagnostic of a well in partial penetration in a reservoir. Figures 7.2 and 7.3 illustrates this example.

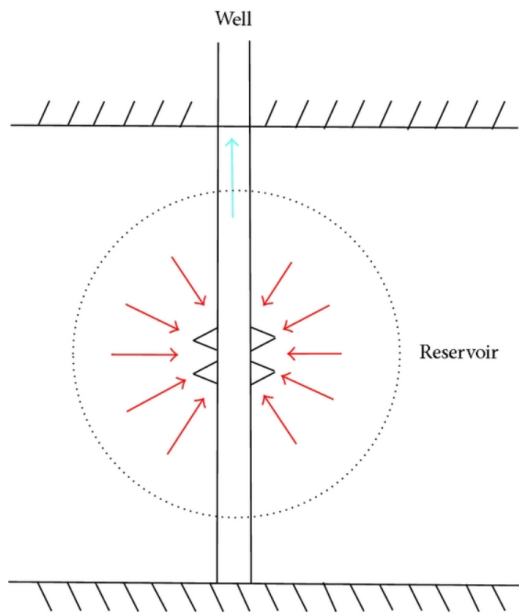


Figure 7.2: Schematical representation of a spherical flow in a reservoir.  
Source: Bourdet (2002).

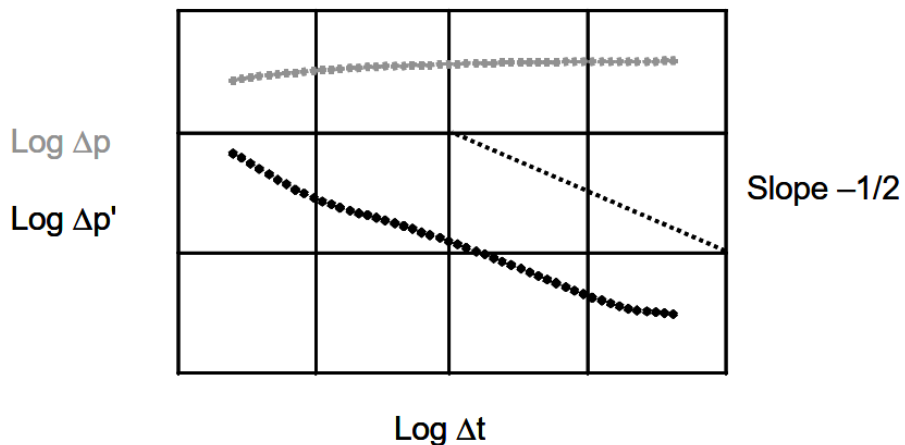


Figure 7.3: Pressure drop and its derivative in a log-log plot for a well with partial penetration. Bourdet (2002) shows that the slope of the pressure derivative curve is equal to  $-\frac{1}{2}$  in this scenario. Source: Bourdet (2002).

This log-log diagnostic graphic plots the pressure drop and its derivative for a drawdown test. The equations below show how those plots are drawn:

$$\Delta p_{wf} = p_{wf} - p_i, \quad (7.0.3)$$

$$\frac{\partial \Delta p_{wf}}{\partial \log t} \approx \frac{\Delta p_{wf}(\log t) + \Delta p_{wf}(\Delta \log t)}{\Delta \log t}, \quad (7.0.4)$$

In the example above, the fluid enters the well by a spherical flow. Bourdet (2002) shows that for this situation, the Bourdet derivative curve follows a straight line with a negative half-unit slope. Bourdet (2002) shows several other diagnostics that could be obtained in well tests by similar analysis. This project's focus is limited to evaluating how this diagnostic log-log plot will change from a model before and after its upscaling.

## Chapter 8

# Analysis of the Impacts of Heterogeneity Losses due to Upscaling in Well Testing Simulations

Chapters 2 to 5 show how the reservoir simulator utilized in this project has been developed and validated. Chapters 6 and 7 show introductions of upscaling and well testing, the areas investigated by this project. This chapter shows the analysis of the effects of upscaling in well testing simulations, the main application of the simulator developed in this project. Several models have been created and put under flow simulation. The results of bottom hole pressure, pressure drop, and Bourdet derivative have been plotted and compared. The idea is to visualize how a numerical model for a pressure transient analysis would provide different results for a fine grid versus an upscaled one. This chapter's first section shows details of each of those models and the parameters of the simulation. The last section will show the results obtained in the simulation and its analyzes.

## 8.1 Models

Eight different cases have been created and simulated for outputting bottom hole pressure, pressure drop, and the Bourdet derivative. They are parallelepipedal models of artificial sandstone reservoirs. Table 8.1 shows the common characteristics for all the cases. The fluid model for all the scenarios is the same as utilized in the validation cases, illustrated by Figure 5.3. The porosity-permeability relationship is equal for all the models and follows the correlation illustrated in Figure 8.1 and in the Eq. 8.1.1.

Table 8.1: Common characteristics for all the simulation cases.

Parameter	Value (if applicable)
Reservoir length in the $x$ direction	2559.03 ft
Reservoir length in the $y$ direction	2559.03 ft
Reservoir length in the $z$ direction	164.04 ft
Boundary conditions	Sealed reservoir
Well	Vertical well in the center of the reservoir
Completions	From the top to the bottom of the reservoir
Average porosity	20%
Average horizontal permeability	51.59 mD
Average vertical permeability	51.59 mD
Formation compressibility	$1.31 \times 10^{-4} \text{ psi}^{-1}$
Fluid compressibility	$1.41 \times 10^{-5} \text{ psi}^{-1}$
Depth of the topmost layer	10,498.69 ft
Reference depth for the initial pressure	10,498.69 ft
Initial pressure at the reference depth	3,916.01 psi
Well radius	6 in
Skin factor	-0.5

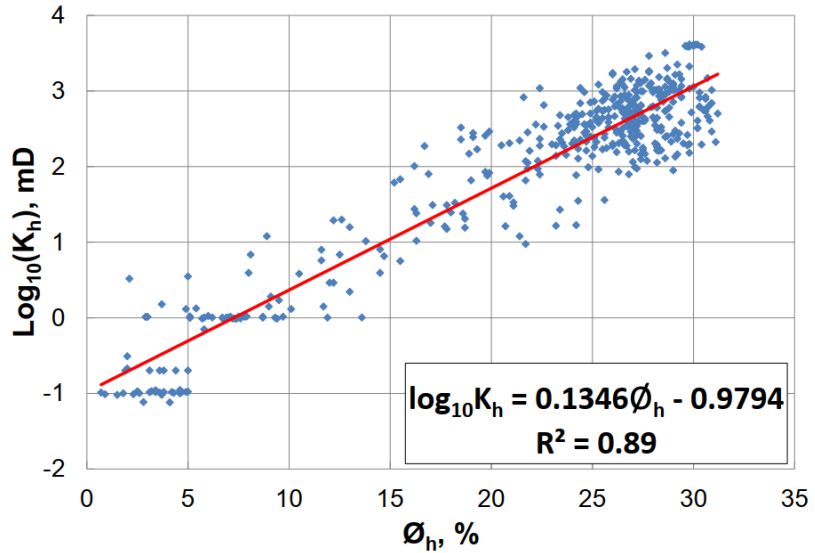


Figure 8.1: Relationship between the porosity and permeability of the UNISIM-I, a synthetic sandstone model based on the Namorado Field, Campos Basin of Brazil. Source: Avansi and Schiozer (2015). The eight models constructed in this chapter have the same porosity-permeability relationship, as shown in this picture.

$$k_h = 10^{(0.1346\phi)-0.9794}. \quad (8.1.1)$$

In other words, Table 8.1, Figure 5.3, Figure 8.1 and Eq. 8.1.1 shows the common characteristics shared between the eight models. What differs one case to another is the size and number of the grid blocks and the standard deviation of the porosity and permeability.

Scenarios 1 and 2 are homogeneous in terms of porosity and permeability. While scenario 1 has a fine grid, scenario two has a coarse grid constructed by the upscaling of scenario 1. In other words, scenario 2 is the upscaled version of scenario 1. Each direction of scenario 2 presents half the number of grid blocks in comparison to scenario 1. Since scenario 1 is homogeneous, there is no spatial variation of porosity and permeability and scaling up can be done straightforwardly, without the need for averaging techniques.

Scenario 3 has heterogeneous permeabilities and porosities. The porosity is populated by utilizing a normal distribution with a mean equals to 20%, the same as scenario 1, and a standard deviation equals 3%. Then, the horizontal permeabilities are calculated by utilizing the correlation shown in Eq. 8.1.1. Finally, the vertical permeabilities are set to be equals to 10% of the horizontal for each grid block. Thus, both the horizontal and vertical perme-

abilities follow log-normal distributions with the same means as in scenario 1. Scenario 4 is the upscaled version of scenario 3. Since porosity and permeability are not homogeneous, it is necessary to perform an upscaling technique. A simple volumetric averaging has been utilized for upscaling the porosity, as shown in Eq. 6.1.1. An arithmetic-harmonic averaging has been utilized for scaling up the permeability tensor, as demonstrated by Eq. 6.2.21.

Scenario 5 is essentially the same as scenario 3, with the difference that the standard deviation of the porosity is set to be equal to 6%, the double of the one from scenario 3. That would result in permeabilities with higher standard deviations as well since they are populated by following the same rules as in scenario 3. Scenario 6 is scenario 5 upscaled by the same approach described above.

Scenario 7 is scenario 3, with a standard deviation of porosity that equals 1.5%, half of the one from scenario 3. Again, the permeabilities have been populated in the same way as described above. Finally, the last scenario, 8, is the upscaled version of scenario 7. Table 8.2 summarizes the differences between each model:

Table 8.2: Difference between each simulation scenario.

Case	Nx	<th>Nz</th> <th>Upscaling</th> <th>Heterogeneity</th> <th><math>\phi</math></th> <th>Standard Deviation</th>	Nz	Upscaling	Heterogeneity	$\phi$	Standard Deviation
1	26	26	20	No	Homogeneous		0
2	13	13	10	No	Homogeneous		0
3	26	26	20	Yes	Heterogeneous		3%
4	13	13	10	Yes	Heterogeneous		6%
5	26	26	20	Yes	Heterogeneous		6%
6	13	13	10	Yes	Heterogeneous		6%
7	26	26	20	Yes	Heterogeneous		1.5%
8	13	13	10	Yes	Heterogeneous		1.5%

Appendix C shows in more detail the porosity-permeability distributions of scenarios 3 to 8. The next section shows the results obtained by the simulation done in those models.

## 8.2 Results

The previous section displays the details of the eight models constructed for this study. All those cases have been put under flow simulation for a drawdown test scenario. The well is initially closed and opens at the time of 0.1 days with a constant flow rate. Then, the simulation continues until time is equal to 2 days. Figure 8.2 shows the flow rate variation in this test:

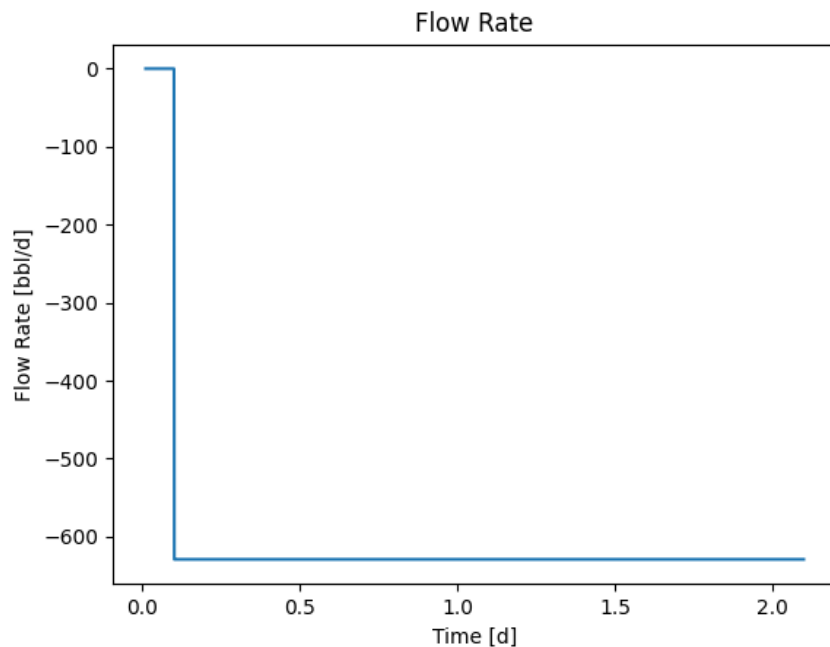


Figure 8.2: Well flow rate for all the cases in the simulation. Negative values indicate production.

This increase in flow rate implies a variation in the bottom hole pressure. Figure 8.3 shows the BHP for all the fine models.

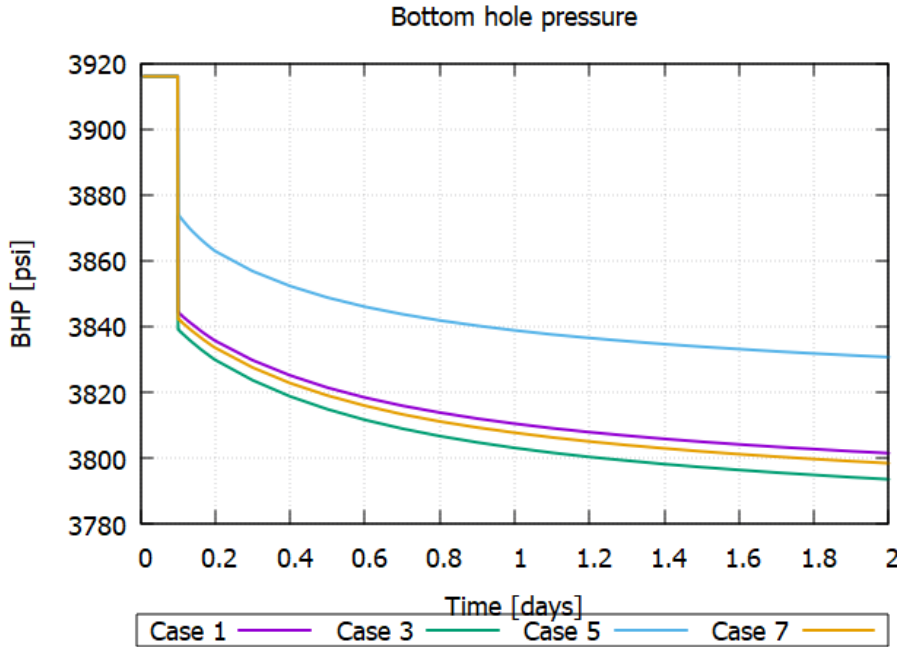


Figure 8.3: Bottom hole pressure for the fine models (case 1, case 3, case 5, and case 7).

One could see that the results for the homogeneous model (case 1) were very similar to the ones of the model with a lower standard deviation (case 7). The BHP for case 5 (higher standard deviation) was considerably higher than those for the cases with lower dispersions. Thus, the porosity-permeability dispersion can change the bottom-hole pressure results in a well test.

Figures 8.4 to 8.7 display the outputs of BHP for the simulations, for each pair of fine-grid model and its upscaled version.

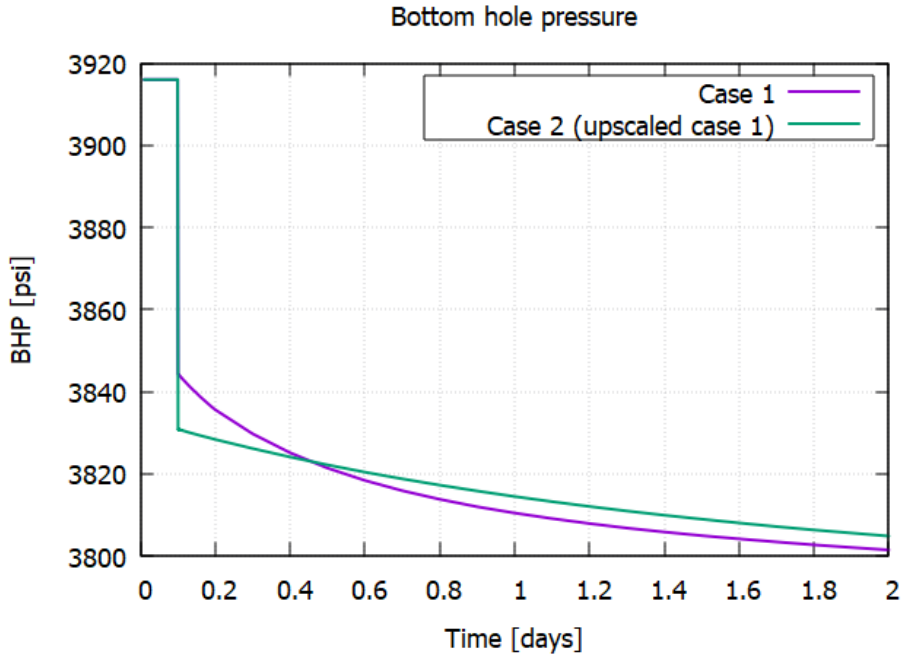


Figure 8.4: Bottom hole pressure for case 1 and its upscaled version, case 2.

Figure 8.4 above shows the BHP for case 1 and case 2 (the upscaled version of case 1). One could see that the results are quite similar from one case to another, as both cases present homogeneous porosity and permeability. In the drawdown period, the bottom-hole pressure for case 2 fits inside the range of maximum-minimum BHP for case 1. One possible explanation for this result is that, since case 1 has a larger number of grid-blocks than case 2, the pressure transient propagates more continuously the grid in case 1 than in case 2.

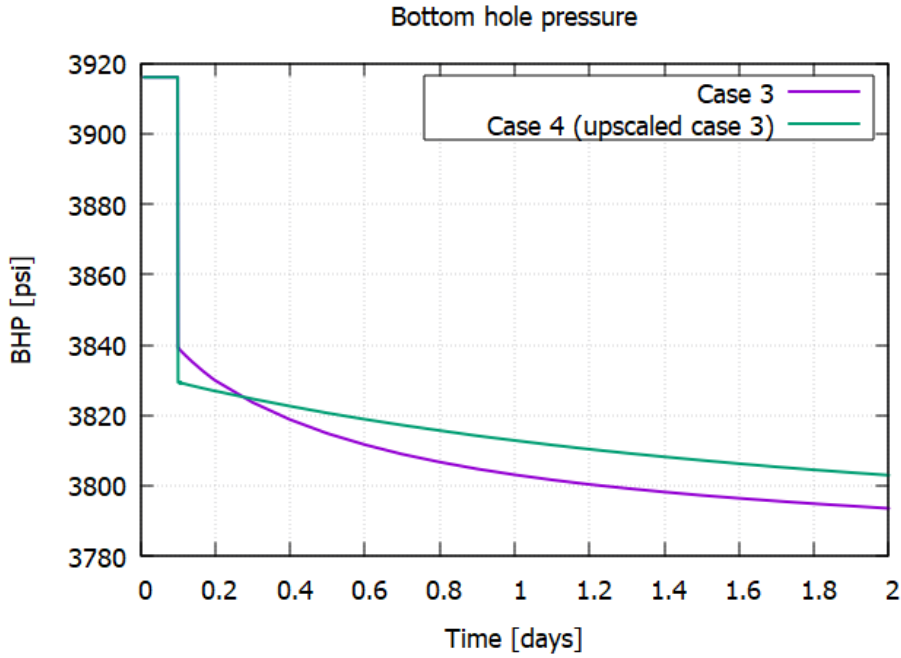


Figure 8.5: Bottom hole pressure for case 3 and its upscaled version, case 4.

Figure 8.5 shows the results for case 3 and its upscaled version, case 4. Differently than cases 1 and 2, cases 3 and 4 are heterogeneous reservoirs. Thus, the arithmetic-harmonic technique has been utilized in the upscaling for generating case 4. The difference between the curves is higher in cases 3 and 4 than in cases 1 and 2. Nevertheless, this difference is still small, showing that the arithmetic-averaging upscaling represented the fine model with reasonably good accuracy.

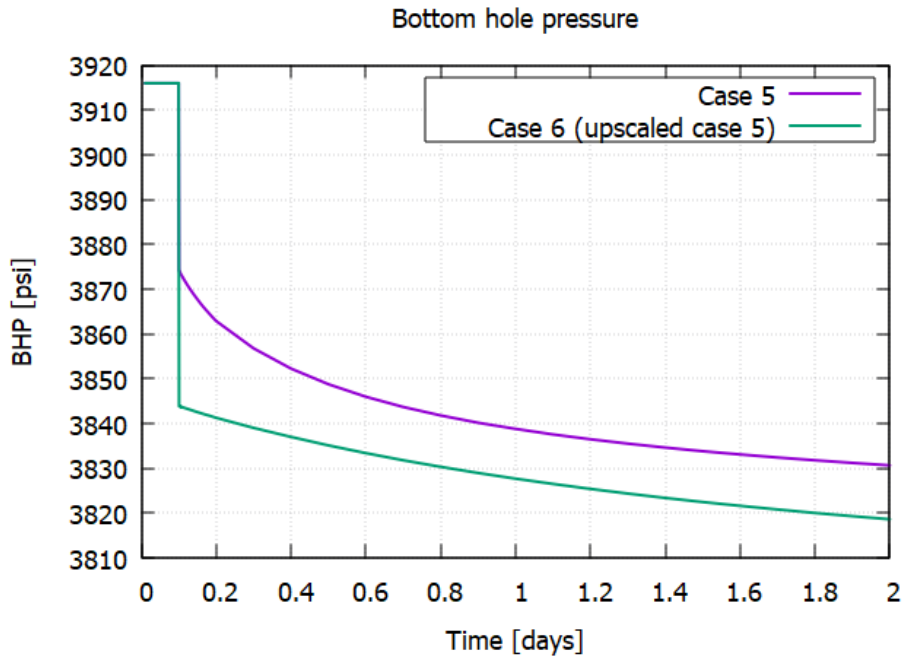


Figure 8.6: Bottom hole pressure for case 5 and its upscaled version, case 6.

Figure 8.6 above shows the results for case 5 and its upscaled version, case 6. Those are the cases with the higher standard deviation of porosity and, consequently, permeability. As shown by the image above, those are also the cases with the highest difference between the curves for the fine-grid and upscaled models.

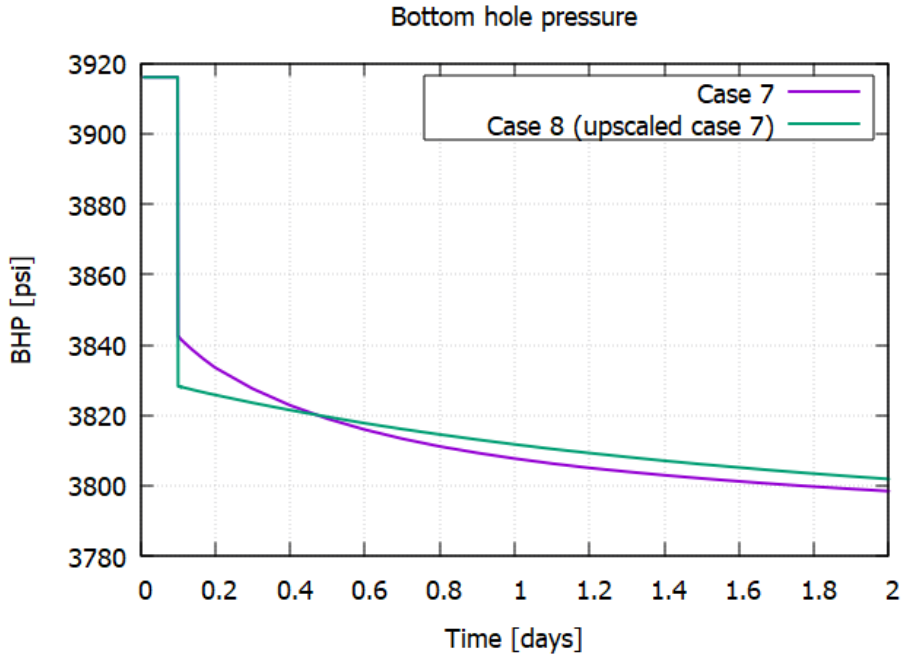


Figure 8.7: Bottom hole pressure for case 7 and its upscaled version, case 8.

Figure 8.7 displays the same information for cases 7 and 8. Those are the heterogeneous models with the lowest standard deviation in porosity and permeability. Those are also the cases in which the curves are closer to the upscaled model and its fine-grid counterpart. Looking at the previous four images, Figures 8.4 to Figure 8.7, one could see that the difference between bottom-hole pressure for the fine-grid and coarse-grid models is consistently greater when the standard deviations in the porosity-permeability are higher.

Next, Figure 8.8 below shows the diagnostic log-log plot of the pressure drop and the Bourdet derivative against the elapsed time for the fine-grid models, cases 1, 3, 5, and 7.

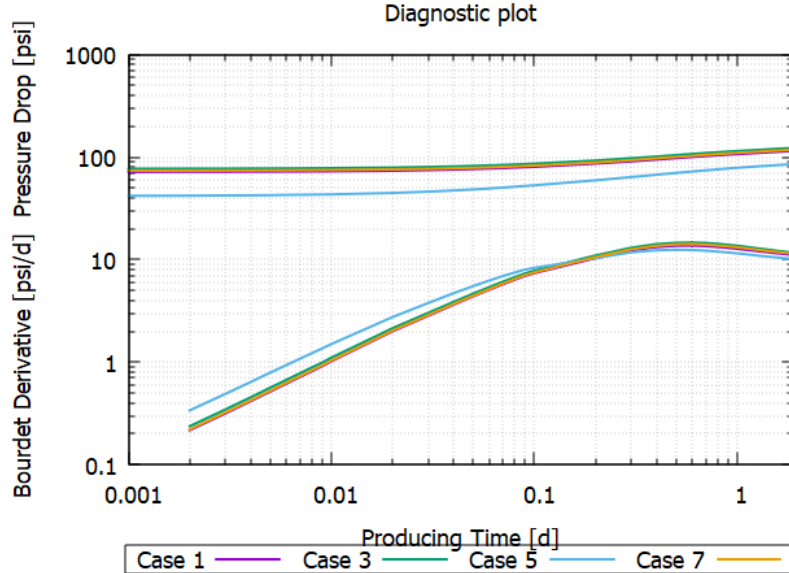


Figure 8.8: Pressure drop and Bourdet derivative for the fine-grid models (case 1, case 3, case 5, and case 7).

Looking at the figure above, one could see that the curves of cases 1, 3, and 7 are very close one to another. Case 5 presents lower pressure drops and higher Bourdet derivatives than the other scenarios due to its higher standard deviation. The next four figures, 8.9 to 8.12, show this diagnostic plot for each pair of fine-grid/upscaled models.

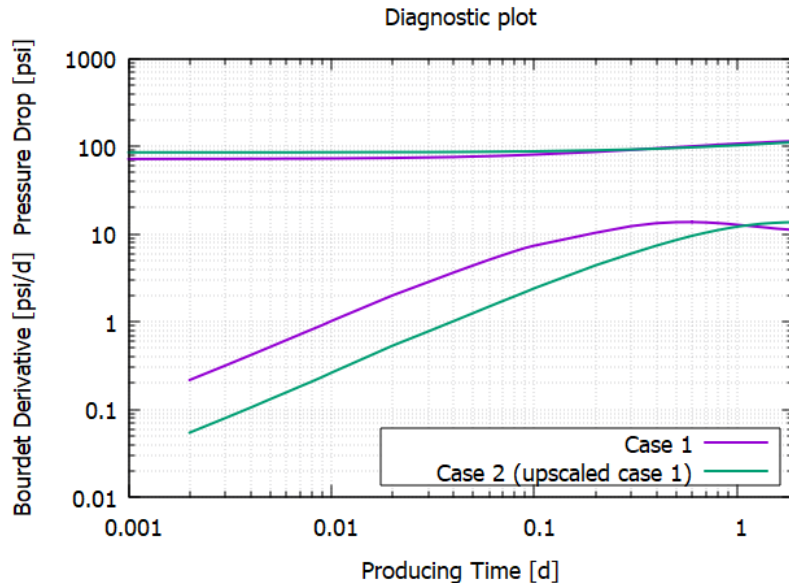


Figure 8.9: Pressure drop and Bourdet derivative for case 1 and its upscaled version, case 2.

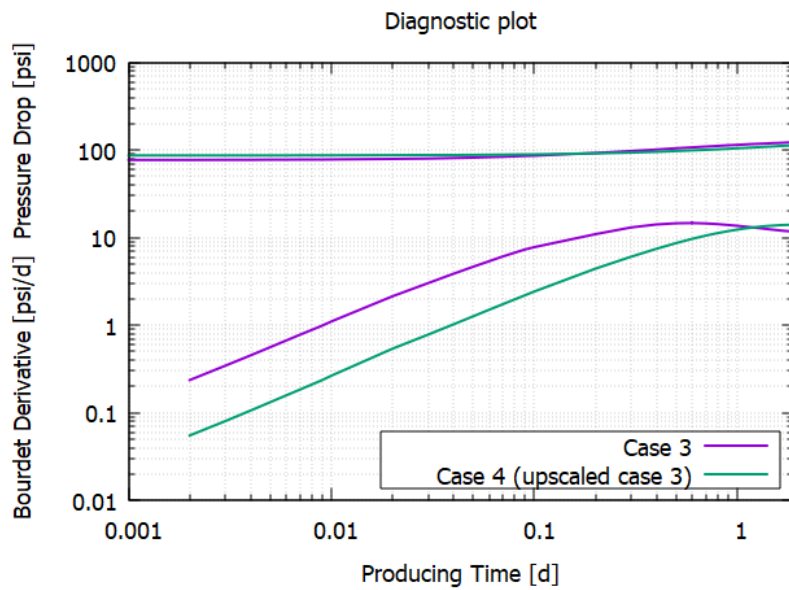


Figure 8.10: Pressure drop and Bourdet derivative the case 3 and its upscaled version, case 4.

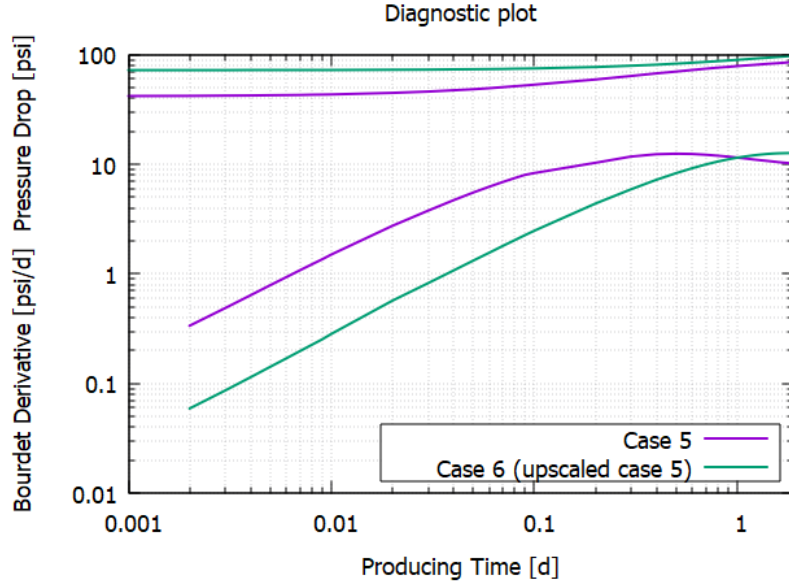


Figure 8.11: Pressure drop and Bourdet derivative the case 5 and its upscaled version, case 6.

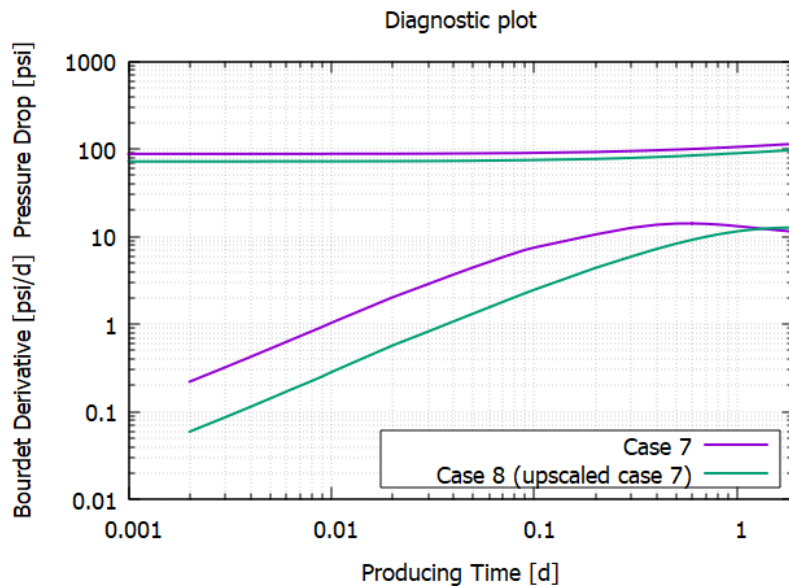


Figure 8.12: Pressure drop and Bourdet derivative the case 7 and its upscaled version, case 8.

The images above show pressure drop curves very close to each other. How-

ever, they also show a considerable difference between the Bourdet derivative curves for the fine-grid models and their upscaled version. In the rightmost part of the Bourdet derivative curves, it seems like the fine-grid models show a slightly negative decline while their upscale versions do not. This discrepancy is higher for cases with higher standard deviations. Since there are techniques of pressure transient analysis that evaluate the slope in this area of the Bourdet derivative curve (for example, describing the flow regime), the discrepancy between simulations of fine-grid models and their upscaled versions could lead to misinterpretations in well testing. Nevertheless, more profound studies are made necessary for analyzing this possibility.

# Chapter 9

## Final Remarks

The main goal of this project has been to analyze the results of well tests in reservoir models both before and after their upscaling. This analysis requires the utilization of a reservoir simulator, which was also developed in this project. The first part of this document shows the development of this reservoir simulator. Then, the basic theory behind upscaling and well testing is presented in its second part. The third and final part of the document shows the construction of the fine-grid and upscaled models and the results and analysis of their well test simulations.

The reservoir simulator has been developed for enabling the simulation of single-phase flow of compressible fluid in a tridimensional, block-centered grid representing a sealed reservoir with a well in its center. Chapter 2 shows the mathematical formulation of this simulator. The discretization has been approached by the finite-difference method known as BTCS (Backwards Time, Central Space) and the linearization has been done by the method described by Ertekin et al. (2001) as the simple iteration of the transmissibility terms. This numerical model is described in more detail in Chapter 3. The well model has been developed for taking into account the effects of multiple perforated layers, as described in Chapter 4, a necessary approach when analyzing upscaling. The simulator has been validated by comparing its results to simulations done by industry-standard software. In conclusion, the software obtained a high accuracy in its results, as shown in Chapter 5, and the validation was a success.

Next, Chapter 6 shows the fundamentals of upscaling, highlighting the simple volumetric averaging and the arithmetic-harmonic averaging upscaling, the techniques utilized in this project for the scaling up of porosity and permeability, respectively. Chapter 7 shows the basics of well testing and the plots analyzed in this project, the bottom-hole pressure, pressure drop, and Bourdet derivative curves.

At last, the analysis of the impacts of heterogeneity losses due to upscaling in well test simulations are shown in Chapter 8. Firstly, four fine-grid reservoir models have been created, cases 1, 3, 5, and 7. The only difference between one of those models to another is the dispersion of porosity and permeability. The first case is homogeneous and each other case has a different value of standard deviations. Then, four other models, cases 2, 4, 6, and 8, have been generated by the upscaling of those fine-grid models. Appendix C shows the petrophysical distributions of all those models in more detail. All those eight models have been put under flow simulation for a drawdown stage of a well test, and the results of bottom-hole pressure, pressure drop, and Bourdet derivative have been output. An analysis of the BHP plots shows that the differences in the curves of bottom-hole pressure for the fine-grid and upscaled models are higher for the cases with more porosity-permeability dispersion. This is also true for the pressure drop and Bourdet derivative, the differences of those curves for the fine-grid and upscaled models are also higher for the cases more heterogeneous. The final part of the Bourdet derivative curves have slightly different slopes for the models before and after their upscaling. This might induce biases in a pressure transient analysis, considering that this slope is often utilized for inferring dynamic characteristics of the well, such as the flow regime. Nevertheless, a more profound analysis is required.

## 9.1 Future Suggestions

Future suggestions for this line of study can be divided into two branches: the analysis of the effects of upscaling in well test simulations and the improvement of the reservoir simulator developed in this project. For the first, some suggestions for future projects include:

- Verify if the difference in fine-grid and upscaled models could generate misinterpretations in pressure transient analysis by evaluating slopes in the Bourdet derivative curve.
- Perform the evaluation above for other heterogeneity scenarios other than white noise, such as fractures, high-permeability layers, and channels.
- Analyze the effects of wellbore storage in the Bourdet derivative curves for fine-grid and upscaled models.
- Perform the evaluations above, utilizing different techniques of upscaling, such as harmonic averaging, arithmetic averaging, harmonic- arithmetic averaging, and flow-base methods.

Some suggestions for improving the simulator developed in this project are:

- Expand the simulator for handling other internal and external boundary conditions.
- Expand the simulator for allowing multiple wells and well control groups.
- Expand the mathematical/numerical model for multiphase flow, for a black oil or compositional model.
- Improve the well model for allowing horizontal wells.
- Allow the utilization of grids other than block centered, Cartesian grid. Some examples include a hybrid grid (Cartesian with cylindrical coordinates in the surroundings of the wells), Voronoi grid, and corner-point grid.
- Enable the utilization of the net-to-gross ratio for allowing the modeling of more advanced geological features.

# Bibliography

- T. H. Ahmed. *Reservoir Engineering Handbook*. Professional Publishing, 1946.
- G. D. Avansi and D. J. Schiozer. Unisim-i: Synthetic model for reservoir development and management applications. *International Journal of Modeling and Simulation for the Petroleum Industry*, 9:21–30, 2015.
- D. Bourdet. *Well Test Analysis: The use of Advanced Interpretation Models*, volume 3 of the Handbook of Petroleum Exploration and Production Series. Elsevier Science, 2002.
- M. A. Christie. Upscaling for reservoir simulation. *Journal of Petroleum Technology*, 48:1004–1010, 1996.
- T. A. Davis. *UMFPACK User Guide*, 1995.
- T. Ertekin, J. H. Abou-Kassem, and G. R. King. *Basic applied reservoir simulation*. SPE Textbook Series 7, 2001.
- R. W. Fox, A. T. McDonald, and P. J. Pritchard. *Introduction to fluid mechanics*. Wiley, Hoboken, 2008.
- G. H. Golub and C. F. Van Loan. *Matrix Computations*. Johns Hopkins, 1996.
- R. Heinzl. *Concepts for Scientific Computing*. PhD thesis, Technischen Universität Wien, 1988.
- S. G. Kandlikar, S. Garimella, D. Li, S. Colin, and M. R. King. *Heat Transfer and Fluid Flow in Minichannels and Microchannels*. Butterworth-Heinemann, Oxford, second edition edition, 2014.
- K. A. Lie. *An Introduction to Reservoir Simulation Using MATLAB: User Guide for the Matlab Reservoir Simulation Toolbox (MRST)*. SINTEF ICT, Oslo, 2015.

---

*Bibliography*

- K. Nunna, P. Zhou, and M. J. King. *Novel Diffuse Source Pressure Transient Upscaling*. Society of Petroleum Engineering, 2015.
- O. Wiener. *Abhandlungen der Matematisch*. PhD thesis, Physischen Klasse der Königlichen Sächsischen Gesellschaft der Wissenschaften, 1912.

---

## Appendices

# Appendix A

## Visualization of the Linear System of Equations

As shown in the chapter 3, obtaining the pressure distribution in the reservoir for a posterior time step  $p^{n+1}$  requires Eq. 3.5.9 to be solved for each block in the grid. That spans a linear system of  $n$  equations in which  $n$  is the number of grid blocks in the model. Ertekin et al. (2001) exemplifies this for a tridimensional grid in which  $n_x = 4$ ,  $n_y = 3$  and  $n_z = 3$ , and thus  $n = 36$ . Figure A.1 shows the reservoir model utilized in this example:

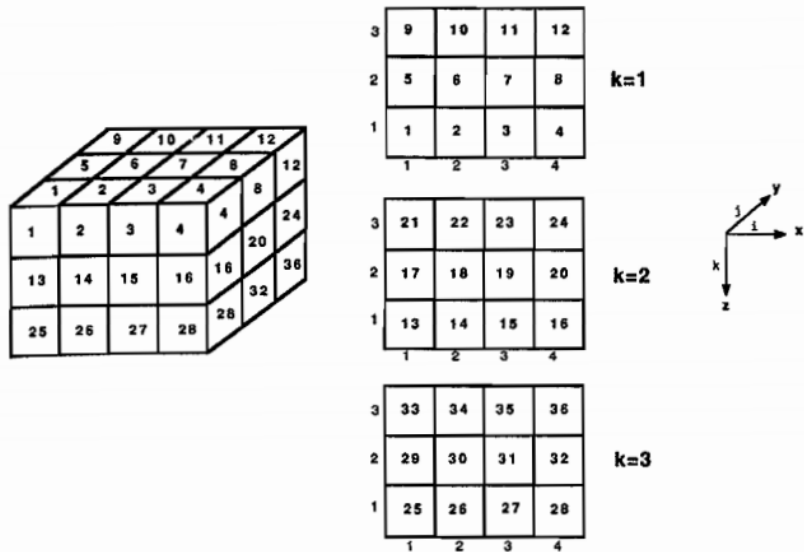


Figure A.1: Example of a  $4 \times 3 \times 3$  grid modeling a parallelepipedal reservoir.  
Source: Ertekin et al. (2001).

---

## Appendix A. Visualization of the Linear System of Equations

---

Applying the Eq. 3.4.17 in the grid block number 1 of this example:

$$W_1^{n+1} p_{out}^{n+1} + E_1^{n+1} p_2^{n+1} + S_1^{n+1} p_{out}^{n+1} + N_1^{n+1} p_5^{n+1} + B_1^{n+1} p_{13}^{n+1} + A_1^{n+1} p_{out}^{n+1} + C_1^{n+1} p_1^{n+1} = Q_1^{n,n+1}. \quad (\text{A.0.1})$$

For the sake of simplicity, the indexes *ind* of Eq. 3.4.17 were changed to the grid block indexes shown in Figure A.1. The subscript *out* indicates that the grid block is out of the domain of the reservoir. This simulator considers the boundary conditions to be a sealed reservoir, in which there is no flow through the borders of the model. That can be implemented by assigning a value equals to zero to the transmissibilities of the grid blocks if the transmissibility face is on in a reservoir's boundary. Thus, Eq. A.0.1 can be simplified as:

$$E_1^{n+1} p_2^{n+1} + N_1^{n+1} p_5^{n+1} + B_1^{n+1} p_{13}^{n+1} + C_1^{n+1} p_1^{n+1} = Q_1^{n,n+1}. \quad (\text{A.0.2})$$

For the grid block number 2:

$$W_2^{n+1} p_1^{n+1} + E_2^{n+1} p_3^{n+1} + N_2^{n+1} p_6^{n+1} + B_2^{n+1} p_{14}^{n+1} + C_2^{n+1} p_2^{n+1} = Q_2^{n,n+1}. \quad (\text{A.0.3})$$

For the other grid blocks:

$$W_3^{n+1} p_2^{n+1} + E_3^{n+1} p_4^{n+1} + N_3^{n+1} p_7^{n+1} + B_3^{n+1} p_{15}^{n+1} + C_3^{n+1} p_3^{n+1} = Q_3^{n,n+1}, \quad (\text{A.0.4})$$

$$W_4^{n+1} p_3^{n+1} + N_4^{n+1} p_8^{n+1} + B_4^{n+1} p_{16}^{n+1} + C_4^{n+1} p_4^{n+1} = Q_4^{n,n+1}, \quad (\text{A.0.5})$$

$$E_5^{n+1} p_6^{n+1} + N_5^{n+1} p_9^{n+1} + S_5^{n+1} p_1^{n+1} + B_5^{n+1} p_{17}^{n+1} + C_5^{n+1} p_5^{n+1} = Q_5^{n,n+1}, \quad (\text{A.0.6})$$

$$W_6^{n+1} p_5^{n+1} + E_6^{n+1} p_7^{n+1} + N_6^{n+1} p_{10}^{n+1} + S_6^{n+1} p_2^{n+1} + B_6^{n+1} p_{18}^{n+1} + C_6^{n+1} p_6^{n+1} = Q_6^{n,n+1}, \quad (\text{A.0.7})$$

$$W_7^{n+1} p_6^{n+1} + E_7^{n+1} p_8^{n+1} + N_7^{n+1} p_{11}^{n+1} + S_7^{n+1} p_3^{n+1} + B_7^{n+1} p_{19}^{n+1} + C_7^{n+1} p_7^{n+1} = Q_7^{n,n+1}, \quad (\text{A.0.8})$$

---

*Appendix A. Visualization of the Linear System of Equations*

---

$$W_8^{n+1}p_7^{n+1} + N_8^{n+1}p_{12}^{n+1} + S_8^{n+1}p_4^{n+1} + B_8^{n+1}p_{20}^{n+1} + C_8^{n+1}p_8^{n+1} = Q_8^{n,n+1}, \quad (\text{A.0.9})$$

$$E_9^{n+1}p_{10}^{n+1} + S_9^{n+1}p_5^{n+1} + B_9^{n+1}p_{21}^{n+1} + C_9^{n+1}p_9^{n+1} = Q_9^{n,n+1}, \quad (\text{A.0.10})$$

$$W_{10}^{n+1}p_9^{n+1} + E_{10}^{n+1}p_{11}^{n+1} + S_{10}^{n+1}p_6^{n+1} + B_{10}^{n+1}p_{22}^{n+1} + C_{10}^{n+1}p_{10}^{n+1} = Q_{10}^{n,n+1}, \quad (\text{A.0.11})$$

$$W_{11}^{n+1}p_{10}^{n+1} + E_{11}^{n+1}p_{12}^{n+1} + S_{11}^{n+1}p_7^{n+1} + B_{11}^{n+1}p_{23}^{n+1} + C_{11}^{n+1}p_{11}^{n+1} = Q_{11}^{n,n+1}, \quad (\text{A.0.12})$$

$$W_{12}^{n+1}p_{11}^{n+1} + S_{12}^{n+1}p_8^{n+1} + B_{12}^{n+1}p_{24}^{n+1} + C_{12}^{n+1}p_{12}^{n+1} = Q_{12}^{n,n+1}, \quad (\text{A.0.13})$$

$$E_{13}^{n+1}p_{14}^{n+1} + N_{13}^{n+1}p_{17}^{n+1} + A_{13}^{n+1}p_1^{n+1} + B_{13}^{n+1}p_{25}^{n+1} + C_{13}^{n+1}p_{13}^{n+1} = Q_{13}^{n,n+1}, \quad (\text{A.0.14})$$

$$\begin{aligned} W_{14}^{n+1}p_{13}^{n+1} + E_{14}^{n+1}p_{15}^{n+1} + N_{14}^{n+1}p_{18}^{n+1} + A_{14}^{n+1}p_2^{n+1} \\ + B_{14}^{n+1}p_{26}^{n+1} + C_{14}^{n+1}p_{14}^{n+1} = Q_{14}^{n,n+1}, \end{aligned} \quad (\text{A.0.15})$$

$$\begin{aligned} W_{15}^{n+1}p_{14}^{n+1} + E_{15}^{n+1}p_{16}^{n+1} + N_{15}^{n+1}p_{19}^{n+1} + A_{15}^{n+1}p_3^{n+1} \\ + B_{15}^{n+1}p_{27}^{n+1} + C_{15}^{n+1}p_{15}^{n+1} = Q_{15}^{n,n+1}, \end{aligned} \quad (\text{A.0.16})$$

$$W_{16}^{n+1}p_{15}^{n+1} + N_{16}^{n+1}p_{20}^{n+1} + A_{16}^{n+1}p_4^{n+1} + B_{16}^{n+1}p_{28}^{n+1} + C_{16}^{n+1}p_{16}^{n+1} = Q_{16}^{n,n+1}, \quad (\text{A.0.17})$$

$$\begin{aligned} E_{17}^{n+1}p_{18}^{n+1} + N_{17}^{n+1}p_{21}^{n+1} + S_{17}^{n+1}p_{13}^{n+1} + A_{17}^{n+1}p_5^{n+1} \\ + B_{17}^{n+1}p_{29}^{n+1} + C_{17}^{n+1}p_{17}^{n+1} = Q_{17}^{n,n+1}, \end{aligned} \quad (\text{A.0.18})$$

$$\begin{aligned} W_{18}^{n+1}p_{17}^{n+1} + E_{18}^{n+1}p_{19}^{n+1} + N_{18}^{n+1}p_{22}^{n+1} + S_{18}^{n+1}p_{14}^{n+1} \\ + A_{18}^{n+1}p_6^{n+1} + B_{18}^{n+1}p_{30}^{n+1} + C_{18}^{n+1}p_{18}^{n+1} = Q_{18}^{n,n+1}, \end{aligned} \quad (\text{A.0.19})$$

---

*Appendix A. Visualization of the Linear System of Equations*

---

$$\begin{aligned} W_{19}^{n+1} p_{18}^{n+1} + E_{19}^{n+1} p_{20}^{n+1} + N_{19}^{n+1} p_{23}^{n+1} + S_{19}^{n+1} p_{15}^{n+1} \\ + A_{19}^{n+1} p_7^{n+1} + B_{19}^{n+1} p_{31}^{n+1} + C_{19}^{n+1} p_{19}^{n+1} = Q_{19}^{n,n+1}, \end{aligned} \quad (\text{A.0.20})$$

$$\begin{aligned} W_{20}^{n+1} p_{19}^{n+1} + N_{20}^{n+1} p_{24}^{n+1} + S_{20}^{n+1} p_{16}^{n+1} + A_{20}^{n+1} p_8^{n+1} \\ + B_{20}^{n+1} p_{32}^{n+1} + C_{20}^{n+1} p_{20}^{n+1} = Q_{20}^{n,n+1}, \end{aligned} \quad (\text{A.0.21})$$

$$E_{21}^{n+1} p_{22}^{n+1} + S_{21}^{n+1} p_{17}^{n+1} + A_{21}^{n+1} p_9^{n+1} + B_{21}^{n+1} p_{33}^{n+1} + C_{21}^{n+1} p_{21}^{n+1} = Q_{21}^{n,n+1}, \quad (\text{A.0.22})$$

$$\begin{aligned} W_{22}^{n+1} p_{21}^{n+1} + E_{22}^{n+1} p_{23}^{n+1} + S_{22}^{n+1} p_{18}^{n+1} + A_{22}^{n+1} p_{10}^{n+1} \\ + B_{22}^{n+1} p_{34}^{n+1} + C_{22}^{n+1} p_{22}^{n+1} = Q_{22}^{n,n+1}, \end{aligned} \quad (\text{A.0.23})$$

$$\begin{aligned} W_{23}^{n+1} p_{22}^{n+1} + E_{23}^{n+1} p_{24}^{n+1} + S_{23}^{n+1} p_{19}^{n+1} + A_{23}^{n+1} p_{11}^{n+1} \\ + B_{23}^{n+1} p_{35}^{n+1} + C_{23}^{n+1} p_{23}^{n+1} = Q_{23}^{n,n+1}, \end{aligned} \quad (\text{A.0.24})$$

$$W_{24}^{n+1} p_{23}^{n+1} + S_{24}^{n+1} p_{20}^{n+1} + A_{24}^{n+1} p_{12}^{n+1} + B_{24}^{n+1} p_{36}^{n+1} + C_{24}^{n+1} p_{24}^{n+1} = Q_{24}^{n,n+1}, \quad (\text{A.0.25})$$

$$E_{25}^{n+1} p_{26}^{n+1} + N_{25}^{n+1} p_{29}^{n+1} + A_{25}^{n+1} p_{13}^{n+1} + C_{25}^{n+1} p_{25}^{n+1} = Q_{25}^{n,n+1}, \quad (\text{A.0.26})$$

$$W_{26}^{n+1} p_{25}^{n+1} + E_{26}^{n+1} p_{27}^{n+1} + N_{26}^{n+1} p_{30}^{n+1} + A_{26}^{n+1} p_{14}^{n+1} + C_{26}^{n+1} p_{26}^{n+1} = Q_{26}^{n,n+1}, \quad (\text{A.0.27})$$

$$W_{27}^{n+1} p_{26}^{n+1} + E_{27}^{n+1} p_{28}^{n+1} + N_{27}^{n+1} p_{31}^{n+1} + A_{27}^{n+1} p_{15}^{n+1} + C_{27}^{n+1} p_{27}^{n+1} = Q_{27}^{n,n+1}, \quad (\text{A.0.28})$$

$$W_{28}^{n+1} p_{27}^{n+1} + N_{28}^{n+1} p_{32}^{n+1} + A_{28}^{n+1} p_{16}^{n+1} + C_{28}^{n+1} p_{28}^{n+1} = Q_{28}^{n,n+1}, \quad (\text{A.0.29})$$

$$E_{29}^{n+1} p_{30}^{n+1} + N_{29}^{n+1} p_{33}^{n+1} + S_{29}^{n+1} p_{25}^{n+1} + A_{29}^{n+1} p_{17}^{n+1} + C_{29}^{n+1} p_{29}^{n+1} = Q_{29}^{n,n+1}, \quad (\text{A.0.30})$$

---

## Appendix A. Visualization of the Linear System of Equations

---

$$W_{30}^{n+1} p_{29}^{n+1} + E_{30}^{n+1} p_{31}^{n+1} + N_{30}^{n+1} p_{34}^{n+1} + S_{30}^{n+1} p_{26}^{n+1} + A_{30}^{n+1} p_{18}^{n+1} + C_{30}^{n+1} p_{30}^{n+1} = Q_{30}^{n,n+1}, \quad (\text{A.0.31})$$

$$W_{31}^{n+1} p_{30}^{n+1} + E_{31}^{n+1} p_{32}^{n+1} + N_{31}^{n+1} p_{35}^{n+1} + S_{31}^{n+1} p_{27}^{n+1} + A_{31}^{n+1} p_{19}^{n+1} + C_{31}^{n+1} p_{31}^{n+1} = Q_{31}^{n,n+1}, \quad (\text{A.0.32})$$

$$W_{32}^{n+1} p_{31}^{n+1} + N_{32}^{n+1} p_{36}^{n+1} + S_{32}^{n+1} p_{28}^{n+1} + A_{32}^{n+1} p_{20}^{n+1} + C_{32}^{n+1} p_{32}^{n+1} = Q_{32}^{n,n+1}, \quad (\text{A.0.33})$$

$$E_{33}^{n+1} p_{34}^{n+1} + S_{33}^{n+1} p_{29}^{n+1} + A_{33}^{n+1} p_{21}^{n+1} + C_{33}^{n+1} p_{33}^{n+1} = Q_{33}^{n,n+1}, \quad (\text{A.0.34})$$

$$W_{34}^{n+1} p_{33}^{n+1} + E_{34}^{n+1} p_{35}^{n+1} + S_{34}^{n+1} p_{30}^{n+1} + A_{34}^{n+1} p_{22}^{n+1} + C_{34}^{n+1} p_{34}^{n+1} = Q_{34}^{n,n+1}, \quad (\text{A.0.35})$$

$$W_{35}^{n+1} p_{34}^{n+1} + E_{35}^{n+1} p_{36}^{n+1} + S_{35}^{n+1} p_{31}^{n+1} + A_{35}^{n+1} p_{23}^{n+1} + C_{35}^{n+1} p_{35}^{n+1} = Q_{35}^{n,n+1}, \quad (\text{A.0.36})$$

$$W_{36}^{n+1} p_{35}^{n+1} + S_{36}^{n+1} p_{32}^{n+1} + A_{36}^{n+1} p_{24}^{n+1} + C_{36}^{n+1} p_{36}^{n+1} = Q_{36}^{n,n+1}. \quad (\text{A.0.37})$$

That constitutes a system of 36 equations with 36 unknowns: the pressures at each of the 36 grid blocks at the next time step  $p^{n+1}$ . This system can be rewritten as a matrix multiplication in the form:

$$Ax = B. \quad (\text{A.0.38})$$

Figure A.2 illustrates this system of equations in a matricial form. The left-most matrix,  $A$ , is a sparse matrix, which means it is a matrix composed mostly by zeroes. Its non-zero members are  $A_{ind}^{n+1}, N_{ind}^{n+1}, E_{ind}^{n+1}, C_{ind}^{n+1}, W_{ind}^{n+1}, S_{ind}^{n+1}$  and  $B_{ind}^{n+1}$ .  $ind$  is equals to the index of the grid block in this example. For the nature of the problem, each of those coefficients is mapped in a diagonal. Thus, the coefficient matrix  $A$  is a heptadiagonal matrix.

---

*Appendix A. Visualization of the Linear System of Equations*

$$\left[ \begin{array}{c} \text{B}_{i,j,k} \\ \text{N}_{i,j,k} \\ \text{E}_{i,j,k} \\ \text{C}_{i,j,k} \\ \text{W}_{i,j,k} \\ \text{S}_{i,j,k} \\ \text{A}_{i,j,k} \end{array} \right] = \left[ \begin{array}{c} \text{P}_{i,j,k}^{n+1} \\ \text{Q}_{i,j,k} \end{array} \right]$$

Figure A.2: Representation of the system of equations originated in the simulation of the reservoir described by Figure A.1. Source: Ertekin et al. (2001).

The non-zero entries in the coefficient matrix, the left-side matrix shown in Figure A.2, are shown in the Figure A.3 bellow:

---

*Appendix A. Visualization of the Linear System of Equations*

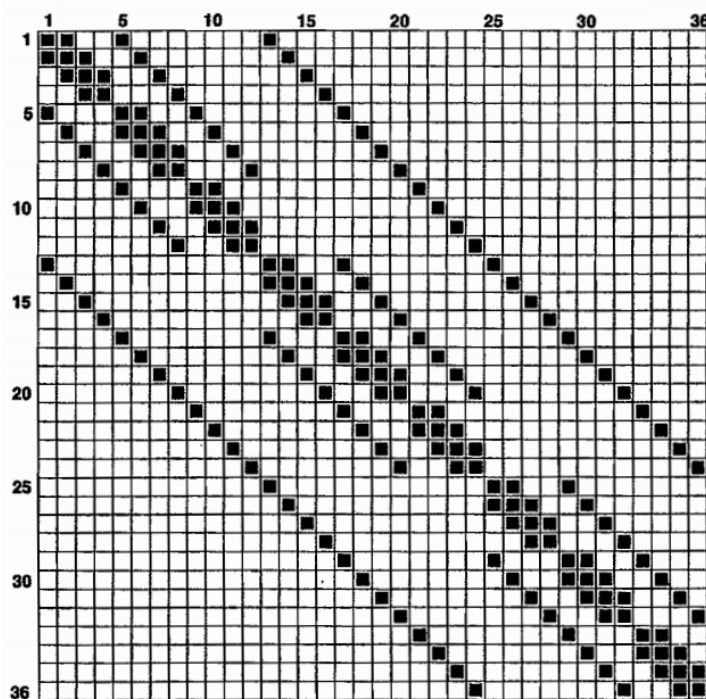


Figure A.3: Coefficient matrix of the system of equations originated from the Ertekin et al. (2001) example of a  $4 \times 3 \times 3$  reservoir with sealed boundaries. The black squares represent the non-zero entries. Source: Ertekin et al. (2001).

## Appendix B

# Sparse Matrices Representation with the CSC Method

Appendix A shows how the mathematical and numerical formulations of this project spawn a sparse system of equations. This appendix shows how the coefficient matrix of this system of equations has been compressed for solving it with linear algebra tools. The first section describes and exemplifies the compression method utilized, the CSC (Compressed Sparse Column), from a general perspective. The last section shows how this method has been utilized in this specific project.

## B.1 Representation of a Generic Matrix with the CSC Method

According to Golub and Loan (1996), a matrix is sparse if most of its elements are zero. Figure A.3 is an example of one of them. By contrast, if most of the elements in a matrix are non-zero, it is a dense one. Another form of visualizing this is by the concept of sparsity. The sparsity is defined as the number of non-zero entries in the matrix divided by the total number of elements. If the sparsity of a matrix is higher than 50%, it is sparse; otherwise, the matrix is dense.

Sparse matrices are related to systems with few pairwise interactions. Since each grid block of the model only has pairwise interactions with neighbors, the resulting linear system of equations has a sparse coefficient matrix. If all the cells in the grid had pairwise interactions with all the other grid blocks, the resulting matrix would be dense, which is not the case of this problem.

A simple way to computationally store a  $m \times n$  matrix  $M$  is by utilizing a two-dimensional array, with dimensions  $m \times n$ . If this matrix is composed of real numbers, those two-dimensional arrays will store  $m \times n$  floating-point variables. This is a common way to store data for simple, dense matrices. However, if  $M$  is a sparse matrix, there are more efficient ways for doing that, avoiding unnecessary storage of the zeroes. For this project, the sparse matrix has been stored with the CSC (Compressed Sparse Column) method. This method is compatible with most of the tools available for solving sparse linear systems, such as UMFPACK and Eigen. For understanding the CSC method, consider below the example shown in the Davis (1995). A matrix  $A$  is defined as:

$$A = \begin{bmatrix} 2 & 3 & 0 & 0 & 0 \\ 3 & 0 & 4 & 0 & 6 \\ 0 & -1 & -3 & 2 & 0 \\ 0 & 0 & 1 & 0 & 0 \\ 0 & 4 & 2 & 0 & 1 \end{bmatrix}. \quad (\text{B.1.1})$$

The CSC method consists of storing this matrix by utilizing three arrays:  $A_p$ ,  $A_i$ , and  $A_x$ .

$A_p$  stores the number of non-zero elements in each column, in a specific form. By definition:

$$A_p[0] = 0, \quad (\text{B.1.2})$$

and

$$A_p[ind] = A_p[ind - 1] + NZCount[ind], \text{ for: } 0 < ind < m. \quad (\text{B.1.3})$$

$NZCount[ind]$  is the count of non-zero elements in column  $ind$ , with  $ind$  between 0 and  $m$ . Thus:

$$A_p = [0 \ 2 \ 5 \ 9 \ 10 \ 12]. \quad (\text{B.1.4})$$

By definition,  $A_p[0] = 0$ .  $A_p[1] = 2$ , since there are two non-zero entries in the first column.  $A_p[2] = 5$  since there are three non-zero entries in the second column and two in the first column. An so on. Finally,  $A_p[5] = 12$  because there are 12 non-zero values in the columns 1 to 5, and thus in the whole matrix  $A$ . The NNZ of  $A$  is the number of non-zero entries of the matrix  $A$ , and it always equals to  $A_p[m]$ , the last element of  $A_p$ .

Next, the array  $A_i$  is the list of coordinates of the non-zero entries in the matrix, in terms of row indexes, from the left to the right column. It considers the upmost row index equals to zero, as it is commonly done in computer sciences. Therefore:

$$A_i = [0 \ 1 \ 0 \ 2 \ 4 \ 1 \ 2 \ 3 \ 4 \ 2 \ 1 \ 4]. \quad (\text{B.1.5})$$

$A_i[0] = 0$  since the first element of the first column  $A[0][0] = 2$ .  $A_i[1] = 1$  since the second element of the first column  $A[0][1] = 3$ . Since there are no other elements in the first column,  $A_i[2] = 0$ , since  $A[1][0] = 3$ . And so on. The last element of  $A_i$ ,  $A_i[1][1] = 4$  since 4 is the row index of the last non-zero number,  $A[4][4] = 1$ .

Finally, the array  $A_x$  is the list of values of the non-zero elements of the matrix  $A$ , starting from the top-left to the bottom-right corner of the matrix. Thus:

$$A_x = [2 \ 3 \ 3 \ -1 \ 4 \ 4 \ -3 \ 1 \ 2 \ 2 \ 6 \ 1]. \quad (\text{B.1.6})$$

Those three arrays together,  $A_p$ ,  $A_i$  and  $A_x$  can store the  $A$  matrix data.  $A_p$  and  $A_i$  are arrays of non-negative numbers since they only store counts and indexes. That simple fact alone can decrease the  $A$  matrix's storage size since integer variables are smaller than floating-point ones.  $A_x$  is an array of the same type of variable that the matrix  $A$  stores since it represents the non-zero elements of  $A$ . If  $A$  is a matrix of floating-point variables, then  $A_x$  is an array of floating-point variables. If  $A$  is a matrix of integers, then  $A_x$  stores integers. The dimension of  $A_p$  is  $m + 1$ , with  $m$  equals to the number of columns of the matrix  $A$ . The dimensions of  $A_i$  and  $A_x$  are equal to the NNZ of the matrix  $A$ .

This storing method can substantially reduce the amount of memory utilized in the operations with the matrix  $A$  when compared to a simple, two-dimensional array representation of all the matrix elements. Some sparse linear systems are unpractical to be solved when storing with an uncomressed matrix. This difference in terms of efficiency is higher for matrices

with higher sparsities. The next section will show how this storing method has been applied to compress this specific project's sparse matrix.

## B.2 Representing the Coefficient Matrix of the Linear System of Equations with the CSC Method

Appendix A shows that the linear system of equations spawn by the Eq. 3.5.9 can be written as a matrix multiplication in the form:

$$Ax = B, \quad (\text{B.2.1})$$

illustrated by Figures A.2 and A.3. The matrix  $A$  is an heptadiagonal sparse matrix in that each of its diagonals is defined by the pressure coefficients in the Eq. 3.5.9:  $\overset{(\nu)}{A_{i,j,k}^{n+1}}$ ,  $\overset{(\nu)}{B_{i,j,k}^{n+1}}$ ,  $\overset{(\nu)}{N_{i,j,k}^{n+1}}$ ,  $\overset{(\nu)}{S_{i,j,k}^{n+1}}$ ,  $\overset{(\nu)}{E_{i,j,k}^{n+1}}$ ,  $\overset{(\nu)}{W_{i,j,k}^{n+1}}$  and  $\overset{(\nu)}{C_{i,j,k}^{n+1}}$ . This matrix can be stored in a compressed form by utilizing the method CSC. That consists in writing the matrix in terms of the three arrays  $A_p$ ,  $A_i$  and  $A_x$ , defined in the previous section. Advancing the simulation in time will not change the overall layout of the matrix  $A$  in terms of the position of its non-zero elements. This is due to the problem's nature: the number of pairwise interactions of each grid block in the reservoir does not change with time. Thus, the matrix  $A$  will always have this heptadiagonal form in this problem, described by Figure A.3. That implies that the count and position of the matrix  $A$ 's non-zero elements do not change with time, and neither does  $A_p$  and  $A_i$ . Therefore, they only need to be calculated one time for each simulated model. On the other hand, the values of the non-zero elements can change with time. Hence,  $A_x$  should be recalculated in each time step.

As shown in the previous section,  $A_p$  is an array of non-negative integers with the dimension equal to  $m + 1$  where  $m$  is the number of columns in the matrix  $A$ . As shown in the A, the matrix  $A$  is square and its dimensions are  $n \times n$  where  $n$  is equaled to the number of blocks in the grid. Thus, the dimension of  $A_p$  is equal to  $n_x n_y n_z + 1$ . By definition,  $A_p[0] = 0$ . Next,  $A_{p_{ind}}$  is equal to the number of non-zero coefficients of pressure in Eq. 3.5.9 for the grid blocks of indexes  $ind$  or below. This section will utilize as an example the model described by the Figure A.1, from Ertekin et al. (2001), but a similar approach has been done for every model run in this project. For that example, the grid block of index 1 has only 4 non-zero coefficients, as shown by Eq. A.0.2. Next, the grid block 2 has 5 non-zero coefficients, as can be seen in Eq. A.0.3. Repeating this data collection process for all the grid blocks, it is possible to build the Table B.1, from the number of pressure coefficients found in Eqs. A.0.2 to A.0.37.

Table B.1: Count of the non-zero coefficients of the Eq. 3.5.9 for the grid blocks in the example described by Figure A.1 from Ertekin et al. (2001).

Index <i>ind</i>	Number of non-zero coefficients	Cumulative sum of the count of the non-zero coefficients
1	4	4
2	5	9
3	5	14
4	4	18
5	5	23
6	6	29
7	6	35
8	5	40
9	4	44
10	5	49
11	5	54
12	4	58
13	5	63
14	6	69
15	6	75
16	5	80
17	6	86
18	7	93
19	7	100
20	6	106
21	5	111
22	6	117
23	6	123
24	5	128
25	4	132
26	5	137
27	5	142
28	4	146
29	5	151
30	6	157
31	6	163
32	5	168
33	4	172
34	5	177
35	5	182

Note that all the grid blocks shown in the table above have either 4, 5, 6, or 7 non-zero coefficients. This same fact can be seen in the rows of A.3; they also have from 4 to 7 non-zero elements. That is explained by the boundary conditions of the problem: the transmissibilities are set to zero at the reservoir boundaries. A grid block in the center of the reservoir normally has 7 coefficients in that equation:  $A_{i,j,k}^{n+1}$ ,  $B_{i,j,k}^{n+1}$ ,  $N_{i,j,k}^{n+1}$ ,  $S_{i,j,k}^{n+1}$ ,  $E_{i,j,k}^{n+1}$ ,  $W_{i,j,k}^{n+1}$  and  $C_{i,j,k}^{n+1}$ . For the first grid block, the coefficients  $B_{i,j,k}^{n+1}$ ,  $S_{i,j,k}^{n+1}$  and  $W_{i,j,k}^{n+1}$  are zero since those faces are in the boundaries of the reservoir. The number of coefficients of a given grid block equals to 7 minus the number of faces on the limits of the reservoir. For the specific geometry of this project, a grid block can only have zero to three faces in a boundary. Therefore, it is only possible to have from 4 to 7 non-zero coefficients. The third column in Table B.1 is the cumulative sum of the count of those coefficients for each grid block. That last column equals to  $A_p$ , which written in computer sciences notation is:

$$A_p = [0 \ 4 \ 9 \ 14 \ 18 \ 23 \ 29 \ 35 \ 40 \ 44 \ 49 \ 54 \ \dots \ 182 \ 186]. \quad (\text{B.2.2})$$

$A_i$  is the list of the row indexes of the non-zero coefficients of the matrix  $A$ . For this problem, it represents the grid block indexes of the pressures utilized in the 3.5.9 equation for a given grid block, in ascending order. For the grid block 1 of this example, those are 1, 2, 5, and 13, as can be seen in Eq. A.0.2. For the grid block 2, those are: 1,2,3,6 and 14, according to Eq. A.0.3. Table B.2 shows those pressure indexes for each one of the 36 grid blocks of this example. The table also shows the coefficients of those pressures. Those are equal to  $A_i$  and  $A_x$ , which in computer sciences notation are:

$$A_i = [0 \ 1 \ 4 \ 12 \ 0 \ 1 \ 2 \ 5 \ 13 \ 0 \ \dots \ 23 \ 31 \ 34 \ 35], \quad (\text{B.2.3})$$

and:

$$A_x = [C_1^{n+1} \ E_1^{n+1} \ N_1^{n+1} \ B_1^{n+1} \ W_2^{n+1} \ \dots \ A_{36}^{n+1} \ S_{36}^{n+1} \ W_{36}^{n+1} \ C_{36}^{n+1}]. \quad (\text{B.2.4})$$

Hence, the matrix resulting from Eqs. A.0.2 to A.0.37 can be stored with the CSC method by utilizing the arrays  $A_p$ ,  $A_i$  and  $A_x$  defined by Eqs. B.2.2, B.2.3 and B.2.4.

---

*Appendix B. Sparse Matrices Representation with the CSC Method*

---

Table B.2: Count of the non-zero coefficients of the Eq. 3.5.9 for the grid blocks in the example described by Figure A.1 from Ertekin et al. (2001).

Index <i>ind</i>	Pressure indexes in Eq. 3.5.9	Pressure coefficients in Eq. 3.5.9
1	1,2,5,13	$C_1^{n+1}, E_1^{n+1}, N_1^{n+1}, B_1^{n+1}$
2	1,2,3,6,14	$W_2^{n+1}, C_2^{n+1}, E_2^{n+1}, N_2^{n+1}, B_2^{n+1}$
3	2,3,4,7,15	$W_3^{n+1}, C_3^{n+1}, E_3^{n+1}, N_3^{n+1}, B_3^{n+1}$
4	3,4,8,16	$W_4^{n+1}, C_4^{n+1}, E_4^{n+1}, B_4^{n+1}$
5	1,5,6,9,17	$S_5^{n+1}, C_5^{n+1}, E_5^{n+1}, N_5^{n+1}, B_5^{n+1}$
6	2,5,6,7,10,18	$S_6^{n+1}, W_6^{n+1}, C_6^{n+1}, E_6^{n+1}, N_6^{n+1}, B_6^{n+1}$
7	3,6,7,8,11,19	$S_7^{n+1}, W_7^{n+1}, C_7^{n+1}, E_7^{n+1}, N_7^{n+1}, B_7^{n+1}$
8	4,7,8,12,20	$S_8^{n+1}, W_8^{n+1}, C_8^{n+1}, N_8^{n+1}, B_8^{n+1}$
9	5,9,10,21	$S_9^{n+1}, C_9^{n+1}, E_9^{n+1}, B_9^{n+1}$
10	6,9,10,11,22	$S_{10}^{n+1}, W_{10}^{n+1}, C_{10}^{n+1}, E_{10}^{n+1}, B_{10}^{n+1}$
11	7,10,11,12,23	$S_{11}^{n+1}, W_{11}^{n+1}, C_{11}^{n+1}, E_{11}^{n+1}, B_{11}^{n+1}$
12	8,11,12,24	$S_{12}^{n+1}, W_{12}^{n+1}, C_{12}^{n+1}, B_{12}^{n+1}$
13	1,13,14,17,25	$A_{13}^{n+1}, C_{13}^{n+1}, E_{13}^{n+1}, N_{13}^{n+1}, B_{13}^{n+1}$
14	2,13,14,15,18,26	$A_{14}^{n+1}, W_{14}^{n+1}, C_{14}^{n+1}, E_{14}^{n+1}, N_{14}^{n+1}, B_{14}^{n+1}$
15	3,14,15,16,19,27	$A_{15}^{n+1}, W_{15}^{n+1}, C_{15}^{n+1}, E_{15}^{n+1}, N_{15}^{n+1}, B_{15}^{n+1}$
16	4,15,16,20,28	$A_{16}^{n+1}, W_{16}^{n+1}, C_{16}^{n+1}, E_{16}^{n+1}, B_{16}^{n+1}$
17	5,13,17,18,21,29	$A_{17}^{n+1}, S_{17}^{n+1}, C_{17}^{n+1}, E_{17}^{n+1}, N_{17}^{n+1}, B_{17}^{n+1}$
18	6,14,17,18,19,22,30	$A_{18}^{n+1}, S_{18}^{n+1}, W_{18}^{n+1}, C_{18}^{n+1}, E_{18}^{n+1}, N_{18}^{n+1}, B_{18}^{n+1}$
19	7,15,18,19,20,23,31	$A_{19}^{n+1}, S_{19}^{n+1}, W_{19}^{n+1}, C_{19}^{n+1}, E_{19}^{n+1}, N_{19}^{n+1}, B_{19}^{n+1}$
20	8,16,19,29,24,32	$A_{20}^{n+1}, S_{20}^{n+1}, W_{20}^{n+1}, C_{20}^{n+1}, N_{20}^{n+1}, B_{20}^{n+1}$
21	9,17,12,22,33	$A_{21}^{n+1}, S_{21}^{n+1}, C_{21}^{n+1}, E_{21}^{n+1}, B_{21}^{n+1}$
22	10,18,21,22,23,34	$A_{22}^{n+1}, S_{22}^{n+1}, W_{22}^{n+1}, C_{22}^{n+1}, E_{22}^{n+1}, B_{22}^{n+1}$

Continued on next page

---

Table B.2 – continued from previous page

Index <i>ind</i>	Pressure indexes in Eq. 3.5.9	Pressure coefficients in Eq. 3.5.9
23	11,19,22,23,24,35	$A_{23}^{n+1}, S_{23}^{n+1}, W_{23}^{n+1}, C_{23}^{n+1}, E_{23}^{n+1}, B_{23}^{n+1}$
24	12,20,23,24,36	$A_{24}^{n+1}, S_{24}^{n+1}, W_{24}^{n+1}, C_{24}^{n+1}, B_{24}^{n+1}$
25	13,25,26,29	$A_{25}^{n+1}, C_{25}^{n+1}, E_{25}^{n+1}, N_{25}^{n+1}$
26	14,26,27,30	$A_{26}^{n+1}, W_{26}^{n+1}, C_{26}^{n+1}, E_{26}^{n+1}, N_{26}^{n+1}$
27	15,26,27,28,31	$A_{27}^{n+1}, W_{27}^{n+1}, C_{27}^{n+1}, E_{27}^{n+1}, N_{27}^{n+1}$
28	16,27,28,32	$A_{28}^{n+1}, W_{28}^{n+1}, C_{28}^{n+1}, E_{28}^{n+1}$
29	17,25,29,30,33	$A_{29}^{n+1}, S_{29}^{n+1}, C_{29}^{n+1}, E_{29}^{n+1}, N_{29}^{n+1}$
30	18,26,29,30,31,34	$A_{30}^{n+1}, S_{30}^{n+1}, W_{30}^{n+1}, C_{30}^{n+1}, E_{30}^{n+1}, N_{30}^{n+1}$
31	19,27,30,31,32,35	$A_{31}^{n+1}, S_{31}^{n+1}, W_{31}^{n+1}, C_{31}^{n+1}, E_{31}^{n+1}, N_{31}^{n+1}$
32	20,28,31,32,36	$A_{32}^{n+1}, S_{32}^{n+1}, W_{32}^{n+1}, C_{32}^{n+1}, N_{32}^{n+1}$
33	21,29,33,34	$A_{33}^{n+1}, S_{33}^{n+1}, C_{33}^{n+1}, E_{33}^{n+1}, B_{33}^{n+1}$
34	22,30,33,34,35	$A_{34}^{n+1}, S_{34}^{n+1}, W_{34}^{n+1}, C_{34}^{n+1}, E_{34}^{n+1}$
35	23,31,34,35,36	$A_{35}^{n+1}, S_{35}^{n+1}, W_{35}^{n+1}, C_{35}^{n+1}, E_{35}^{n+1}$
36	24,32,35,36	$A_{36}^{n+1}, S_{36}^{n+1}, W_{36}^{n+1}, C_{36}^{n+1}$

## Appendix C

# Petrophysical Distributions of the Models

This appendix shows the distribution of porosity, horizontal permeability, and vertical permeability for the cases 3 to 8, as defined in Chapter 8. They are shown as histograms of ranges of property values in the  $x$  axis and their frequencies in the  $y$  axis. Each figure contains data from a fine-grid model and its upscaled version.

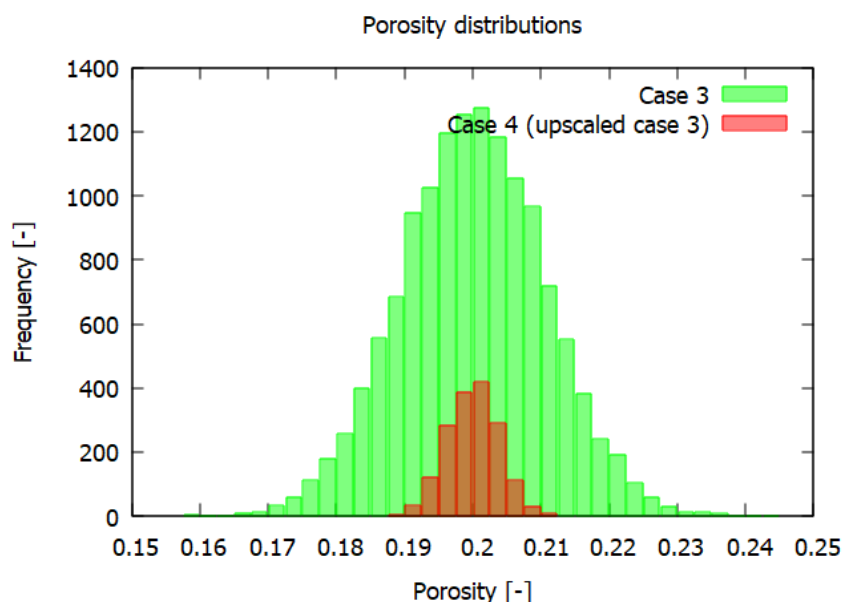


Figure C.1: Porosity distribution for case 3 and its upscaled version (case 4).

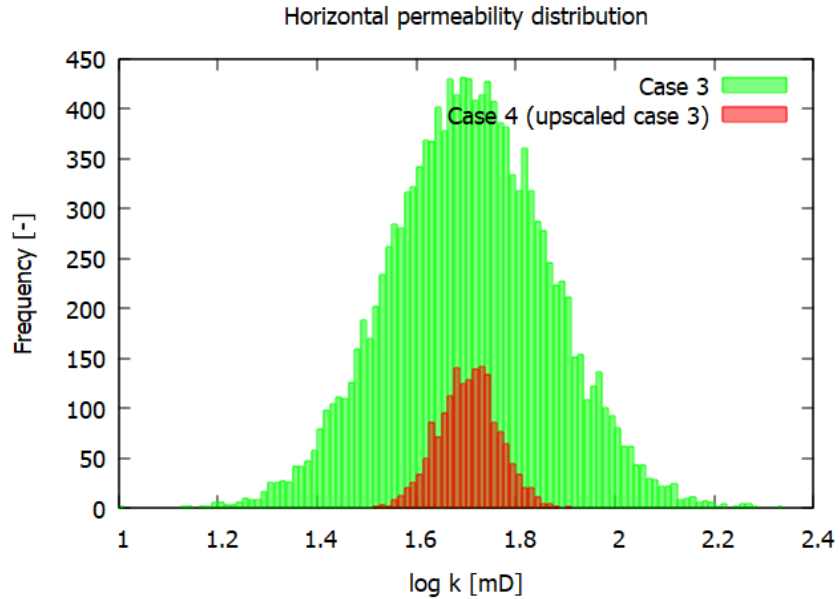


Figure C.2: Horizontal permeability distribution for case 3 and its upscaled version (case 4).

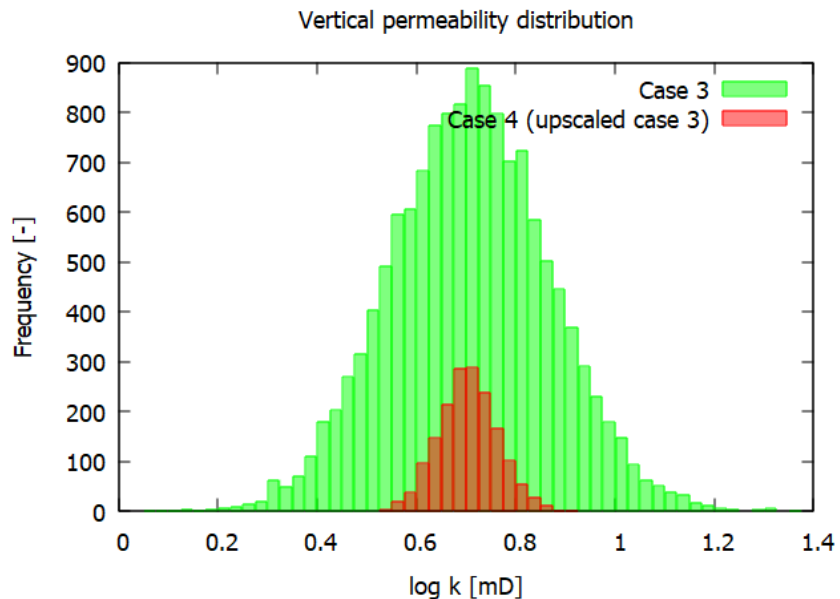


Figure C.3: Vertical permeability distribution for case 3 and its upscaled version (case 4).

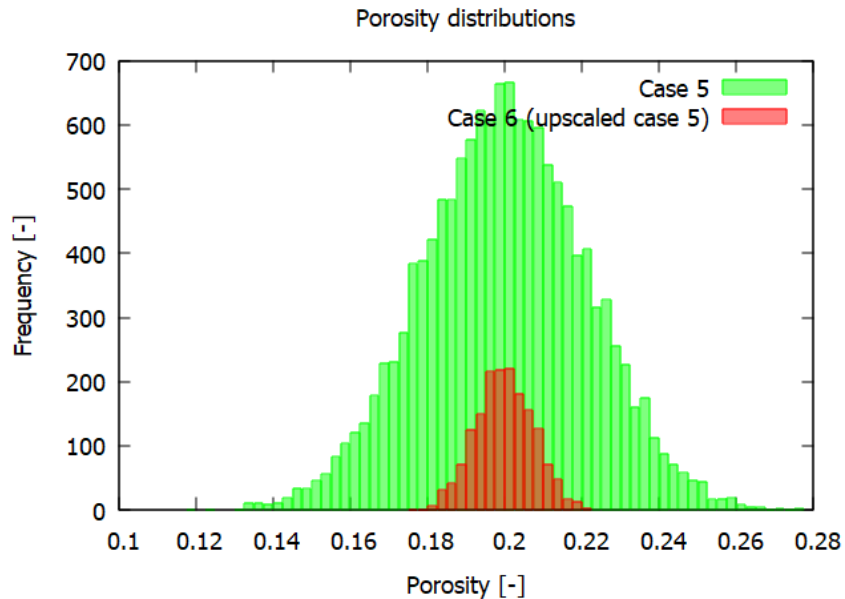


Figure C.4: Porosity distribution for case 5 and its upscaled version (case 6).

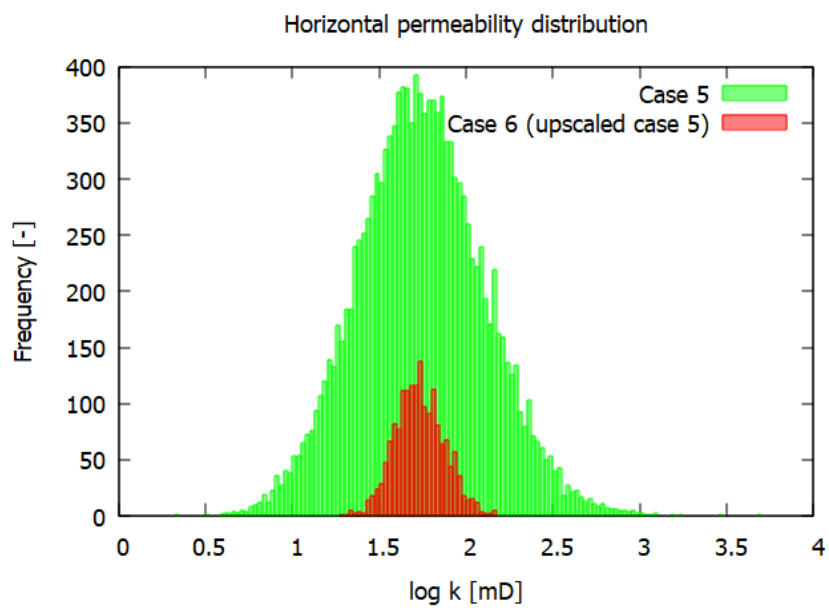


Figure C.5: Horizontal permeability distribution for case 5 and its upscaled version (case 6).

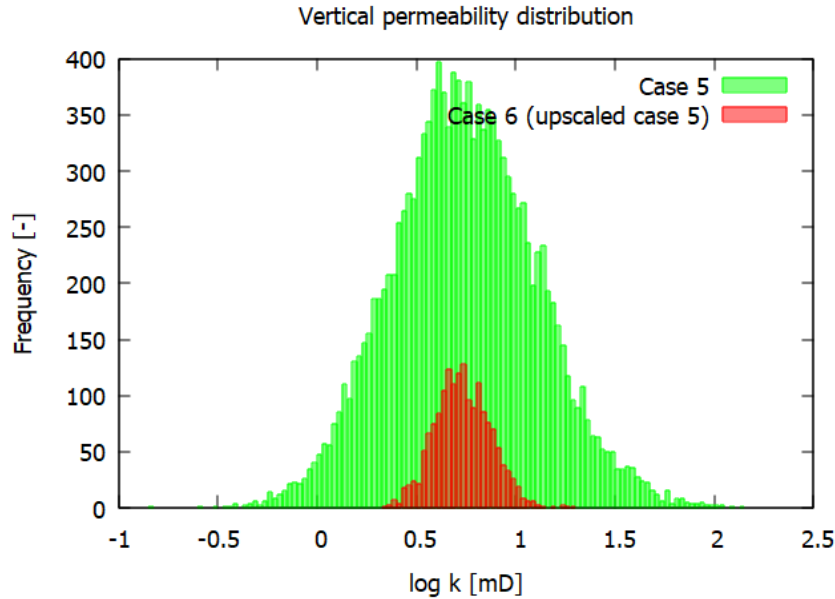


Figure C.6: Vertical permeability distribution for case 5 and its upscaled version (case 6).

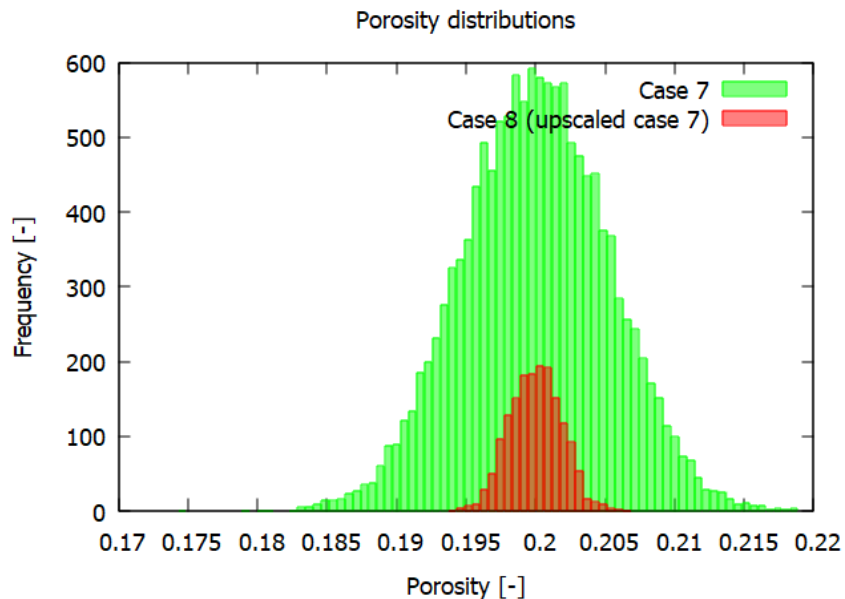


Figure C.7: Porosity distribution for case 7 and its upscaled version (case 8).

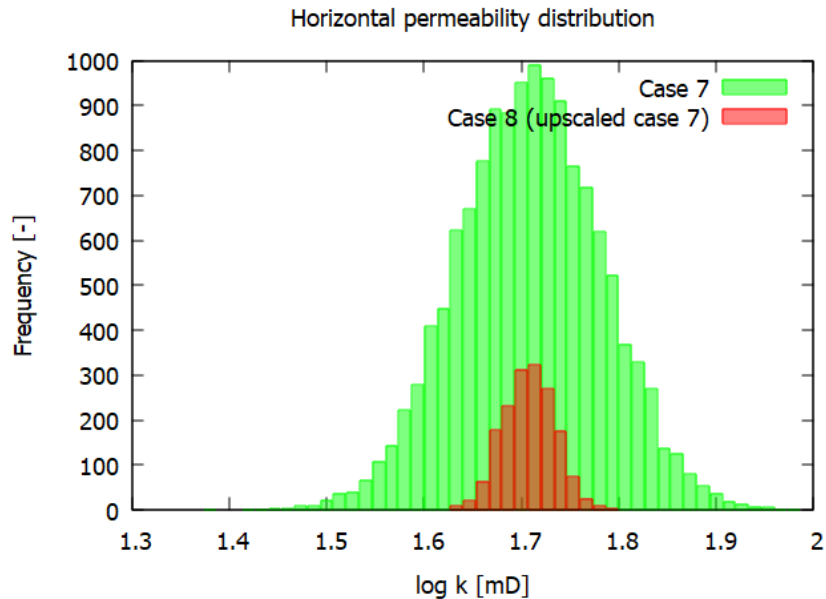


Figure C.8: Horizontal permeability distribution for case 7 and its upscaled version (case 8).

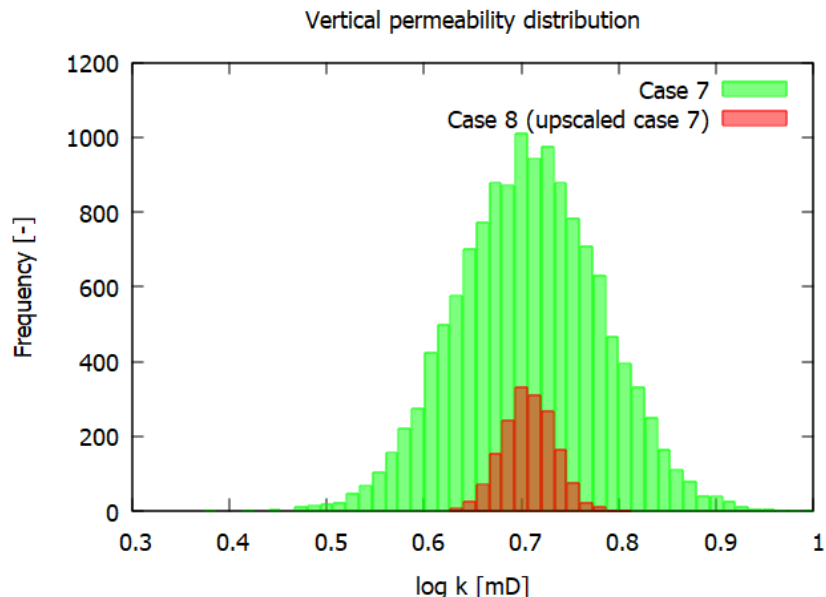


Figure C.9: Vertical permeability distribution for case 7 and its upscaled version (case 8).

Looking at Figures C.1 to C.9 above, one could notice that the red columns (upscaled model) are smaller than the green ones (fine model). This is explained by the fact that the number of grid blocks in the coarse model (upscaled) is eight times inferior to the number of grid blocks in the fine model. Since the vertical axis displays the frequency in absolute terms, the upscaled model should have smaller columns than its fine-grid version. The images above also show that the fine-grid models' dispersion is higher than in its upscaled counterparts. This decrease in dispersion is a natural characteristic of upscaling since averaging reduces dispersion.